

https://dspace.org/

Verification of residual stress compliances in GFRP laminates using a thermal load

Serôdio, Tiago Vicente Morais

2025-07

University of the Witwatersrand, Johannesburg

https://hdl.handle.net/10539/49590

Serôdio, Tiago Vicente Morais. (2025). Verification of residual stress compliances in GFRP laminates using a thermal load. [Master's dissertation, University of the Witwatersrand, Johannesburg]. WIReDSpace. https://hdl.handle.net/10539/49590

Downloaded from a DSpace repository. https://dspace.org/

Verification of residual stress compliances in GFRP laminates using a thermal load

Tiago Vicente Morais Serôdio
Student Number: 1070535

Supervisors:
Prof. Robert Reid
Dr. Teubes Smit

A dissertation submitted to the Faculty of Engineering and the Built Environment, University of the Witwatersrand, in fulfilment of the requirements for the degree of Master of Science in Aeronautical Engineering.

Johannesburg, 13th July 2025

Declaration

I, Tiago Vicente Morais Serôdio (Student Number: 1070535), am a student registered for the degree of Master of Science in Aeronautical Engineering in the academic year 2025.

I hereby declare the following:

- I am aware that plagiarism (the use of someone else's work without their permission and/or without acknowledging the original source) is wrong.
- I confirm that the work submitted herewith for assessment in the above course is my own unaided work except where I have explicitly stated otherwise.
- This task has not been submitted before, either individually or jointly, for any course requirement, examination or degree at this or any other tertiary educational institution.
- I have followed the required conventions in referencing the thoughts and ideas of others.
- I understand that the University of the Witwatersrand may take disciplinary action against me if it can be shown that this task is not my own unaided work or that I failed to acknowledge the sources of the ideas or words in my writing in this task.

Signed this 13th July 2025



Tiago Vicente Morais Serôdio
1070535

Acknowledgements

I would like to express my deepest gratitude to my supervisors, Prof. Robert Reid and Dr. Teubes Smit, for their unwavering support, motivation, and guidance. Their expertise and encouragement have challenged me to grow academically, and I am especially grateful for their insights into the skills I could further develop.

To my girlfriend, Martenique Torlage, your constant support and care have been invaluable. The thoughtful care packages that got me through long nights and your endless words of encouragement have meant the world to me.

I am profoundly grateful to my parents, Tony and Nela Serôdio, for their sacrifices and unwavering belief in me, which enabled me to pursue both my undergraduate and postgraduate studies. To my brother, André Serôdio, for always knowing the right words to push me forward and inspire me to achieve more.

Finally, to my church community, whom I regard as family, thank you for your thoughts and prayers — they have been a source of strength throughout this journey.

Abstract

Composite materials, particularly Fibre Reinforced Polymers (FRPs), have become widely used due to their favourable material properties such as an excellent strength-to-weight ratio. The manufacturing process for FRPs induces residual stresses into the manufactured component. These residual stresses are mainly attributed to the difference in Coefficients of Thermal Expantion (CTEs) between the fibres and the matrix, and matrix shrinkage due to cross-linking of the polymers during curing. Incremental Hole Drilling (IHD) is commonly used to measure these residual stresses due to its ease of application, accuracy, and relatively low cost. Calibration coefficients are necessary for the IHD method to relate the strain release measured on the surface of a specimen to the residual stresses present at a given depth, and are typically found using Finite Element (FE) analysis. The series expansion computational method makes use of varying temperature profiles to induce eigenstrains, and hence obtain calibration coefficients for known stress distributions. Tensile and bending loads have previously been used to verify the validity of the residual stresses found by incremental hole drilling. The use of thermal loads to validate the residual stress found through IHD has not yet been assessed, however. This approach has the advantage of requiring less cumbersome equipment than that required to apply bending or tensile loads.

The primary objective of this work is to assess how well zeroth-order calibration coefficients (and hence surface strains) predicted by FE correspond to those measured experimentally in the presence of uniform thermal loading. In pursuit of this aim, a Dual-Chamber Controllable Temperature Environment (DCCTE) was built to expose predrilled Glass-fibre Reinforced Polymer (GFRP) laminates to a large change in temperature, which induces measurable surface strains at each hole. The strains are compared with those obtained by FE. The trend in the measured strains largely align with those obtained by FE, however, the magnitudes of the experimental strains at each hole are all offset from those predicted by FE by a similar magnitude. The undrilled strain gauge rosette used for reference measurements was isolated as the source of this error, leading to the finding that selecting alternative rosettes for reference measurements brings the experimentally measured strains closer to those found by FE. Further improvement is possible once individual corrections for hole diameter and offset are implemented. Outliers were identified as having irregularly shaped holes and their results were found to be partially correctable by modelling them more precisely in FE.

Overall, a high level of agreement is observed between the measured strains and those found by FE. Some outliers still remain, indicating that some uncertainties may have been underestimated, and others are not included, and their effect is unknown. The level of agreement between strains obtained experimentally and by FE validates the zeroth-order calibration coefficients found using FE in the series expansion computational method.

Table of Contents

Declaration . . . . . **ii**

Acknowledgements . . . . . **iii**

Abstract . . . . . **iv**

List of Figures . . . . . **viii**

List of Tables . . . . . **ix**

List of Acronyms . . . . . **x**

1 Introduction **1**

2 Literature Survey **4**

2.1 Diffraction methods 4

2.2 Relaxation methods 5

2.2.1 Strain Measurements 7

2.2.2 Obtaining Calibration Coefficients 11

2.2.3 Mathematical Rational 15

2.3 Gap in Existing Literature 18

3 Research Question **19**

4 Objectives **20**

5 Research Method **21**

5.1 Experimental 21

5.1.1 Specimen Preparation 21

5.1.2 Determination of Lamina Properties 23

5.1.3 Controllable Temperature Environment 24

5.1.4 Experimental Apparatus 27

5.1.5 Strain Gauge Self-heating Mitigation 27

5.1.6 Experimentation 29

5.2 Verification of Experimental Method 32

5.2.1 Thermal soak 32

5.2.2 Hole Set A 33

5.2.3 Hole Set B 34

5.2.4 Stabilisation of End Point 35

5.3 Computation 36

5.4 Consolidation between FE and Experimental Data 40

5.4.1 Correcting Discrepancies 41

5.4.2 Uncertainties 42

6 Results and discussion **46**
6.1 $[0_2/90_2]_s$ Laminate 46
6.1.1 Experimental results 46
6.1.2 FE Results 48
6.1.3 Combination of Experimental and FE Strains 50
6.2 $[0/90/+45/-45]_s$ Laminate 56
6.2.1 Experimental Results 56
6.2.2 FE Results 57
6.2.3 Combination of Experimental and FE Strains 58

7 Conclusions **62**

8 Recommendations for future work **64**

References **65**

List of Figures

1 Two-dimensional residual stress plots produced using the contour method [4] 6
2 The layer removal and Sachs' methods of measuring residual stresses [31] 6
3 Slitting method of measuring residual stresses [15] 7
4 Hole drilling as preformed by Mathar with gauge points [34] 7
5 A typical foil strain gauge [37] 8
6 Typical strain gauges used in incremental hole drilling [17] 8
7 Geometry of a single strain gauge within a drilling rosette 9
8 Contour plot of calibration function [40] 10
9 Examples of bands produced when using Moiré interferometry in conjunction with IHD [41] 11
10 Principle of superposition used in the integral method [20] 12
11 Beghini cantilever experimental setup 14
12 Nobre's horizontal tensile test apparatus [24] 14
13 Physical interpretation of matrix G_{ij} for the hole drilling method [12] 16
14 Plan view of $[0_2/90_2]_s$ specimen indicating how the holes are located 22
15 Plan view of $[0/90/45/\text{-}45]_s$ specimen indicating how the holes are located 23
16 Schematic diagram of DCCTE and associated equipment - not to scale 25
17 Control block diagram for DCCTE temperature controller 26
18 Thermal images of strain gauges energised to 2.5 V on a GFRP specimen 28
19 Difference between temperature measured at a strain gauge rosette energised to 2.5 V and ambient temperature 29
20 Strain response of the $[0_2/90_2]_s$ specimen during the thermal soak 32
21 $[0_2/90_2]_s$ normalised strains in relation to time for even depth holes 33
22 $[0_2/90_2]_s$ normalized strains in relation to time for odd depth holes 35
23 $[0_2/90_2]_s$ normalised strains over time for the last 10 minutes of recording 37
24 Mesh constructed for the $[0_2/90_2]_s$ specimen 38
25 Model constraints applicable for the $[0/90/+45/-45]_s$ laminate 39
26 Obtaining strains from deflections of two points 40
27 Strain gauge misalignment and correction 42
28 $[0_2/90_2]_s$ - Strains measured at holes of differing depths in Set A with respect to the undrilled rosette, ΔT = -93.48°C 46
29 $[0_2/90_2]_s$ - Strains measured at holes of differing depths in Set B with respect to the undrilled rosette, ΔT = -94.71°C 47
30 $[0_2/90_2]_s$ - Combined uncorrected measured strains with respect to the undrilled rosette, ΔT = -93.48°C 47
31 $[0_2/90_2]_s$ - FE model with undrilled state as the reference datum, ΔT = 100°C . . . 49
32 $[0_2/90_2]_s$ - FE and uncorrected measured strains referenced to the 0.2 mm deep hole, ΔT = 100°C 50
33 $[0_2/90_2]_s$ - FE and measured strains referenced to the 0.6 mm deep hole, ΔT = 100°C 51

34 $[0_2/90_2]_s$ - Effect of reference hole choice in measured strain, ΔT = 100°C 52
35 $[0_2/90_2]_s$ - 0.4 mm deep hole 53
36 $[0_2/90_2]_s$ - Comparison between strains before and after correction for hole location and diameter, ΔT = 100°C 54
37 0.8mm deep irregular hole drilled on $[0_2/90_2]_s$ specimen 55
38 $[0_2/90_2]_s$ - Correction of 0.8 mm deep hole using more representative FE modelling, ΔT = 100°C 55
39 $[0/90/+45/-45]_s$ - Strains measured at holes of differing depths with respect to the undrilled rosette, ΔT = -98.93°C 56
40 $[0/90/+45/-45]_s$ - FE model with undrilled state as the reference datum, ΔT = 100°C 57
41 $[0_2/90_2]_s$ - FE and measured strains referenced to the undrilled rosette, ΔT = 100°C 58
42 $[0_2/90_2]_s$ - FE and measured strains referenced to the 0.2 mm deep hole, ΔT = 100°C 59
43 $[0/90/+45/-45]_s$ specimen - Strain gauge at 0.4mm deep hole 60

List of Tables

1 Kyowa KFGS-1.5-120-D28-23 specifications 22
2 Lamina ply properties 24
3 Summary of apparatus and materials used 30
4 Inputs parameters used for Monte Carlo simulation to determine CTE uncertainties 44
5 Inputs parameters used for Monte Carlo simulation to determine strain uncertainties 45

List of Acronyms

CNCMM	Computer Numerically Controlled Milling Machine.
CTE	Coefficient of Thermal Expansion.
DAQ	Data Acquisition.
DCCTE	Dual-Chamber Controllable Temperature Environment.
DIC	Digital Image Correlation.
FE	Finite Element.
FML	Fibre Metal Laminate.
FRP	Fibre Reinforced Polymer.
GFRP	Glass-fibre Reinforced Polymer.
IHD	Incremental Hole Drilling.
LSP	Laser Shock Peening.
UHSM	Ultra-High Speed Milling.

1 Introduction

The use of composite materials, particularly Fibre Reinforced Polymers (FRPs), has expanded dramatically due to the excellent strength and lightweight properties that they offer [1]. These properties are particularly useful in the aerospace industry where a lighter material translates to a lighter aircraft, allowing a larger useful cargo weight [2]. Additionally, the orthotropic, laminate nature of FRPs allows designers to construct a laminate in a way that produces desired strengths in the directions required [3], and thereby simultaneously design the part and the material to be used. Thus, a more efficient design can be achieved.

The optimal use of materials requires knowledge of how they behave, particularly after undergoing all necessary manufacturing processes. Residual stresses are often introduced into a material through the manufacturing process, especially through plastic deformation [4, 5]. Residual stresses are naturally in mechanical equilibrium within a flat plate, and are present in a material in the absence of an applied load [6]. The residual stresses in a material can be beneficial or detrimental depending on the location, magnitude, type of stress, and requirements of the design. It is not uncommon for residual stresses to be intentionally introduced into components as part of the manufacturing process to induce some desired trait. Laser Shock Peening (LSP) is a procedure whereby the rapid ablation of a metallic material and/or its coating creates plasma. This produces shock waves in the material, inducing compressive residual stresses that can help slow down crack propagation and increase fatigue life [7]. For the most part residual stresses are unwanted, however. The effect of residual stresses can be similar to that of stress concentrations [8], and can lead to catastrophic failure if not adequately accounted for [4]. In FRPs, residual stresses arise mainly due to the process required to cure the material, both on a micro-mechanical and a meso-mechanical (or ply) level.

Most FRP materials require a two-step curing cycle consisting of two distinct dwelling temperatures [9]. The first dwelling temperature reduces the viscosity of the matrix, allowing gases to escape while minimising the cure of the material as far as possible. After about an hour, the temperature is increased to the second dwelling temperature. This is the temperature where curing takes place. The curing of the material involves the cross-linking of matrix polymers. The cross-linking of polymers can shrink the matrix by up to 6% [9]. Furthermore, the Coefficients of Thermal Expantion (CTEs) of the fibres and the matrix are different. During the cool-down phase of the manufacturing process, the fibres contract less than the matrix. As the part cools, the fibres and the matrix balance each other out on a micromechanical level, inducing residual stresses [9]. On the meso-mechanical level, each layer of a FRP material consists of a unidirectional ply, meaning that all the fibres in that ply are oriented in the same direction. The material properties of the ply in the fibre direction are predominantly influenced by those of the fibre, whereas the properties in the transverse direction are predominantly influenced by the matrix material properties. One of the properties that can differ substantially between these two directions is the CTE. Since plies are stacked in differing fibre directions to produce the

desired layup, their differing CTEs cause each layer to contract and expand differently during the curing process, inducing residual stresses. Given that the material must undergo a curing process, the introduction of residual stresses in FRP components may be minimised, but cannot be totally eliminated.

The importance of quantifying residual stresses has led to the development of methods of measurement that can describe their profile and magnitude. Techniques for measuring residual stresses in manufactured components can be broadly sorted into one of two categories: non-destructive methods, and relaxation/destructive methods. Non-destructive methods rely on the measurement of an effect that can be directly related to stress. The most common subset of non-destructive methods are diffraction-based; namely the X-ray [10] and neutron diffraction [11] methods. These methods use the measured diffraction of radiation waves along with Bragg's Law to calculate the change in spacing in specific crystal lattice planes [11], thereby determining the strain, and by Hooke's Law, the stress present in the material. Since this method relies on the distance between crystal lattice planes, these methods are only suitable for use on crystalline materials.

Non-destructive methods are often preferred as the test specimen is not damaged in the testing process, but for non-crystalline materials such as FRPs, relaxation methods are more appropriate. Relaxation methods are also known as destructive methods because they rely on the incremental removal of material from the specimen in a controlled manner. As the specimen is cut, a new, unstressed surface is exposed which is then used as the zero-stress datum for further cuts. The redistribution of stresses within the material after a cut, measured as deformations at a location close to the cut, allows the original stress state to be determined [4]. The most common subset of relaxation methods are known as Stress Profiling Methods [12]. These include the Layer Removal method [13], Sachs' method [14], the Slitting method [15], the Contour method [16], the Hole Drilling method [17], the Deep Hole Drilling method [18], and the Ring Core method [19].

Although these methods look different in practice, the underlying principle is similar. Material is removed from a specimen and the resulting deformations are measured at some location away from where the material was removed. The initial stress state that would have resulted in the observed change in surface strains is then calculated [4]. The relationship between the measured surface strains and the initial stress state can be described mathematically with an integral, the initial stress state being within the integral. This complicates the computation of the initial stress state significantly [4]. For this reason, calibration coefficients that relate the change in surface strain resulting from the removal of material to the initial stress state of the specimen are needed.

For certain simple cut geometries, the calibration coefficients can be found analytically. This is not the case for more complex geometries and materials, so empirical solutions are often used [20]. When the hole drilling method was in its early stages of development, Kelsey [21] applied known tensile and bending loads to find the calibration coefficients. In later years, advances in

computational power have allowed for the use of the Finite Element (FE) method to find the calibration coefficients [20]. The FE method negated the need for specimen preparation, time, and expertise required to run additional calibration tests. Due to its advantages, the FE method has become commonplace in the determination of calibration coefficients.

FRPs are particularly susceptible to the build-up of residual stresses during manufacturing. Isotropic materials have well-defined methods of relieving and introducing residual stresses, whereas FRPs rely on controlled curing techniques such as optimised curing cycles [22] and microwave heating [23] to reduce the residual stresses present. However, there is a comparatively large body of research regarding the measurement of residual stress in isotropic materials as compared to FRPs. The versatility of FRPs necessitates the need to better understand their behaviours, and to what degree current methods of residual stress measurement are applicable.

In 2023, Nobre et al. [24] investigated the correlation between surface strains due to removed material obtained by FE and those obtained using the Incremental Hole Drilling (IHD) method on a Fibre Metal Laminate (FML) specimen under a known applied tensile load. By obtaining the surface strains for a certain hole depth at two different tensile loads, the principle of superposition was used to isolate the effect of the applied load and possible cutting effects from the residual stresses. Good correlation was found between the FE and empirical results for the tested configuration [24]. A downside to the method used by these researchers is the complexity and size of the apparatus used. With rigidity and the need to apply large loads in mind, the apparatus is bulky and heavy and testing procedures are cumbersome and time-consuming. Furthermore, IHD must be performed while the specimen is under load adding more complexity to the procedure.

Achieving similar results to Nobre et al. using a method that is easier to implement would allow for more materials and configurations to be validated against FE. Since FRPs are generally composed of many layers of unidirectional plies which may be aligned in different fibre directions, each ply has a different CTE in the global x and y direction. Therefore, although a FRP specimen has a CTE in the global x and y direction on a macro-mechanical level, the differing properties in each ply allow internal stresses to be induced by a change in temperature. Smit and Reid have made use of eigenstrains induced through the use of temperature profiles to calculate FE calibration coefficients required for the series expansion analytical method of IHD [25]. It has yet to be experimentally proven whether the surface strains due to removed material correlate to an equivalent FE model when temperature is used to induce a load.

By constructing a thermally controlled environment, thermal stresses can be induced in a FRP specimen. This allows a similar investigation as done by Nobre et al. [24] but with simpler equipment. This research seeks to determine whether correlation exists between the surface strains predicted by FE and empirical data obtained by the introduction of a thermal load to a FRP specimen.

2 Literature Survey

Knowledge of the characteristics of the residual stresses within a material is of great importance as these stresses can affect the performance of the material in service. This leads to a need for accurately measuring residual stresses. Various methods have been developed over the years to fulfil this requirement, each one with different strengths and weaknesses. Due to the importance of the field in material sciences, methods of measuring residual stresses have been improved over time to overcome their inherent limitations. Some of the methods have evolved to become significantly different from their earlier iterations. As more technologies became available they have been employed to make the measurement of residual stresses more accurate, and where possible, easier and more cost-effective. The various methods of measuring residual stresses make use of different physical phenomenon to obtain their readings. Therefore, it is important to carefully consider the limitations of the method to be employed in obtaining the residual stresses within a material to ensure the most suitable method for the required application is selected. Using an inadequate method can result in inaccurate readings at best, and expensive inconclusive readings at worst.

Methods used to measure residual stresses can broadly be divided into two categories: diffraction and relaxation methods [4].

2.1 Diffraction methods

The main advantage of diffraction methods of determining residual stresses is that samples do not need to be damaged in any way [4]. The most common diffraction methods for residual stress measurement are X-ray diffraction [10] and neutron diffraction [11]. These methods are similar in that they use the diffraction of particles in conjunction with Bragg's law to measure the change in distance between crystal latices planes.

The X-ray method makes use of X-rays to measure the atomic spacing between crystal lattice planes. Although effective at measuring the atomic spacing on the surface of a crystalline specimen, the wavelengths of the X-rays generally used (0.071-0.229 nm) [4] mean that the energy levels are not sufficient to penetrate the surface more than tens of microns. Therefore, material must be removed successively to measure residual stresses at greater depths. Although electrochemical methods could be used to remove material layers without introducing further residual stresses [26], the removal of material alters the stress field within the sample [27]. Further processing is therefore required achieve accurate residual stress measurements [27]. Furthermore, the relatively shallow penetration of the X-rays means that only a small volume can be sampled. The local stresses in a crystal phase do not align with that of the material as a whole, and as such special care must be taken to ensure that all phases are measured and their combined effect

determined [4]. The issue of shallow penetration can be overcome by the use of high energy X-rays, where this method can penetrate several millimetres of steel [28]. However, this method requires a synchrotron radiation source at a specialised facility, often with long wait times.

The neutron diffraction method works, in principle, in the same way as the X-ray method, the difference being that neutrons are used. Being uncharged particles, neutrons are able to penetrate materials to much greater depths than X-rays, thereby enabling the determination of stresses to depths of tens or hundreds of millimetres [4]. The residual stress profiles can then be calculated in a much larger volume without requiring the partial destruction of the specimen. The disadvantage of this method is similar to that of high-energy X-rays in that it requires a steady supply of thermal neutrons which is only readily available at a nuclear facility. Furthermore, the neutron diffraction method is limited to samples no smaller than a cube of 1–2 millimetres a side, limiting its usefulness on samples where the residual stresses need to be resolved over a smaller length scale [15].

The largest disadvantage of the diffraction-based methods is that they can only be performed on crystalline materials [29]. This excludes materials such as FRPs. To overcome this limitation, relaxation methods are often employed.

2.2 Relaxation methods

Relaxation methods of measuring residual stresses are some of the most commonly used [30] due to their practicality and accuracy which make them an attractive option when residual stress measurements are required [31]. Not being limited for use with crystalline materials, or even to the physical location of a laboratory, relaxation methods can be used more broadly [32, 33]. These methods all work by the same basic principle of removing material to rearrange the internal stress equilibrium [34]. The reformation of a new stress equilibrium results in measurable deformations. These deformations are measured as strains. By measuring these strains it is possible to determine the stress state prior to the removal of material, but to achieve this, the geometry of the cut needs to be precisely controlled and the strains accurately measured [4]. Some of the most common relaxation methods include: contour, layer removal, Sachs', slitting, and IHD methods.

The contour method [16] makes use of wire electro-discharge machining to cut a cross-section of a specimen. The rearranging of internal stress equilibrium induced by the cutting process results in deformations on the cross-section of the specimen that can be measured by a coordinate measuring machine. Two-dimensional maps of the residual stresses normal to the cutting plane, such as those shown in Figure 1 are produced.

Another method of measuring residual stresses is the layer removal method. In this method, strain gauges are placed on the surface of a plate, and layers of material are removed from the

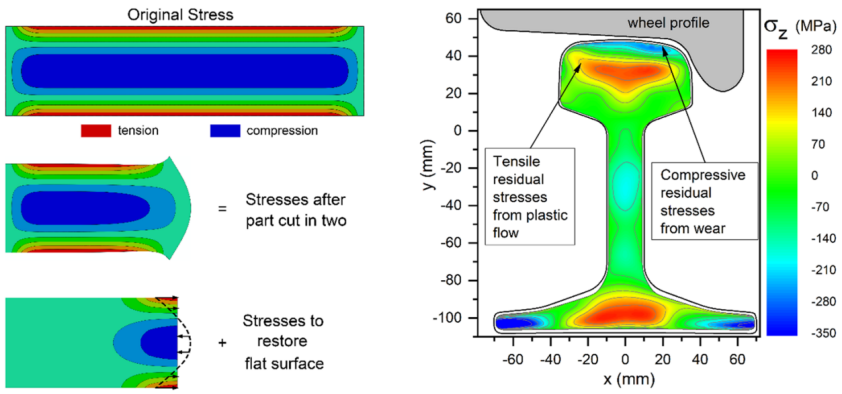

Figure 1: Two-dimensional residual stress plots produced using the contour method [4]

opposite face. Sachs' method is an adaptation of the layer removal method that is used when the residual stresses within a cylindrical sample are to be measured. Two linear strain gauges are placed on the surface of the specimen perpendicular to each other. In FRPs, a full strain gauge rosette with three gauges is used. Through holes are then centrally drilled in progressively larger sizes, thereby removing material. Sachs' method may also be performed by removing a layer of material at a time from the outer surface of a cylinder [35]. Typical setups for the layer removal and Sachs' methods are shown in Figure 2.



(a) Layer removal method

(b) Sachs' Method

Figure 2: The layer removal and Sachs' methods of measuring residual stresses [31]

The layer removal and Sachs' method involve the removal of a whole layer of material, be it from the surface or through the drilling of through-holes. As such, they damage the specimen to a relatively high degree. Additionally, the removal of layers in a FRP leads to an asymmetric laminate. An asymmetric laminate will deform and complicate the strain reading. The remaining methods have the advantage of only damaging the specimen in a small area, opening up the possibility to perform the test in a location that is inconsequential to the final manufactured component and can be removed in subsequent processing. The first of these methods is the slitting method. In this method strain gauges are placed on the surface of the specimen close to where the material is to be removed, and a narrow slit is made. More recent work has found that placing strain gauges on the back of the sample, directly opposing the slit gives more accurate measurements [36]. The depth of the slit is incrementally increased and the strain response recorded. A typical setup for the slitting method is shown in Figure 3.

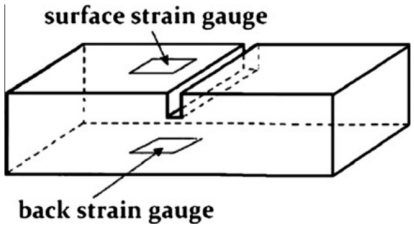

Figure 3: Slitting method of measuring residual stresses [15]

Similar to the slitting method is the IHD method. In this method, a specialised strain gauge rosette is placed on the surface of the specimen, and a hole is incrementally drilled in the centre of the strain gauge rosette. Incremental hole drilling as we know today was pioneered by Mathar in the 1930s [34]. Mathar proposed the use of a tensometer to apply a known load to a sample while drilling a hole through it. A extensometer would be used to measure the distance between the gauge points as seen in Figure 4. The measurements taken would then be used to compute the stresses present in the material before the drilling took place. It is important to note that Mathar's work focused on metallic (and therefore isotropic) materials. Even today, the research performed on isotropic materials is more plentiful than that performed on orthotropic and anisotropic materials.

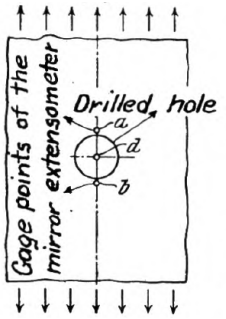

Figure 4: Hole drilling as preformed by Mathar with gauge points [34]

Mathar's research found a relationship between the depth drilled and the resulting deformation around the hole [34]. He also found that the deeper a hole is drilled, the less the hole deforms at the surface, and hence for thicker plates, a through-hole would not be necessary to obtain the residual stresses within the sample [34]. This method forms the basis of all variations on the hole drilling methods used today. All three major steps, drilling, measuring, and computing, have been refined over the years as better technology has become available.

2.2.1 Strain Measurements

Improvements in strain measurements as a hole is being drilled have come in many forms. By far the most common measurement technique due to its moderate equipment costs and its ability to be used in-situ is the use of strain gauges [30]. Strain gauges operate on the principle of the change in resistance of a conductor as it is deformed and therefore consist of a thin electrical

conductor of known nominal resistivity wound up and down a thin foil substrate. An example of a strain gauge is shown in Figure 5. A change in the length of the conductor results in a change in resistance which can measured [37].

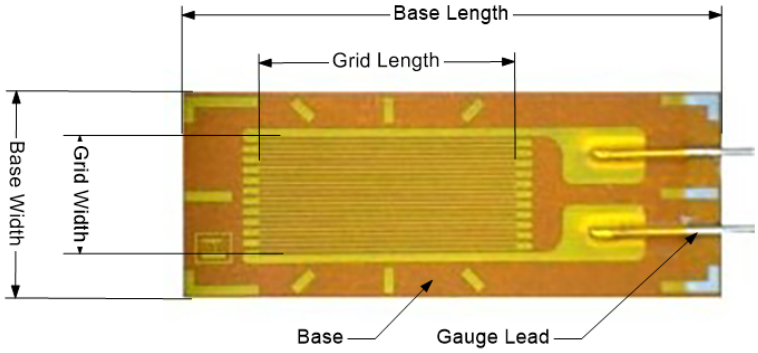

Figure 5: A typical foil strain gauge [37]

The integration of strain gauges into the measurement of residual stresses by hole drilling was first introduced by Soete in 1950 [38]. The computation of residual stresses from measured strains involves an inverse solution of an integral and thus requires accurate readings [4]. Strain gauges allow more precise strain measurements to be obtained as compared to the extensometer used by Mathar, thereby improving the quality and accuracy of residual stresses computed. Soete's method has progressed and been refined, later leading to the standardisation of the method as ASTM Standard Test Method E837 [17]. Many strain gauge types and designs have been experimented with, but the more complex the design, the higher the cost. The most basic, and commonly used strain gauge rosettes follow the Rendler and Vigness design [39]. This is the design employed by the ASTM E837 standard and is sufficient to provide the data necessary to compute the residual stress profiles of the direct stresses in the x, y directions, σ_x and σ_y respectively, and the in-plane shear stress, τ_{xy}. Examples of strain gauges used for incremental hole drilling are shown in Figure 6.

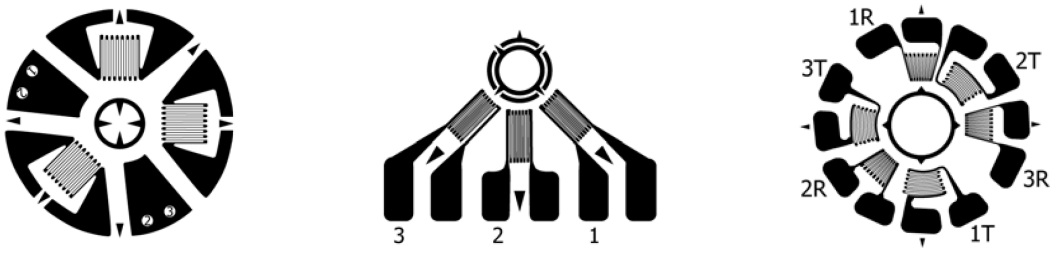

(a) Type A (b) Type B (c) Type C

Figure 6: Typical strain gauges used in incremental hole drilling [17]

Since calibration coefficients serve to relate the change in surface strains to the initial stress state of the material, the geometry of each element within the strain gauge will affect the final calibration coefficients. Figure 7 shows a single strain gauge relative to a drilled hole where GL is the grid length, GW is the grid width, R_1 is the radius of the grid extremity closest to the hole, R_2 is the radius of the grid extremity furthest from the hole, R is the mean radius of the

grid, and R_0 is the radius of the drilled hole. ϕ_1 and ϕ_2 are the boundary angles as seen in the figure.

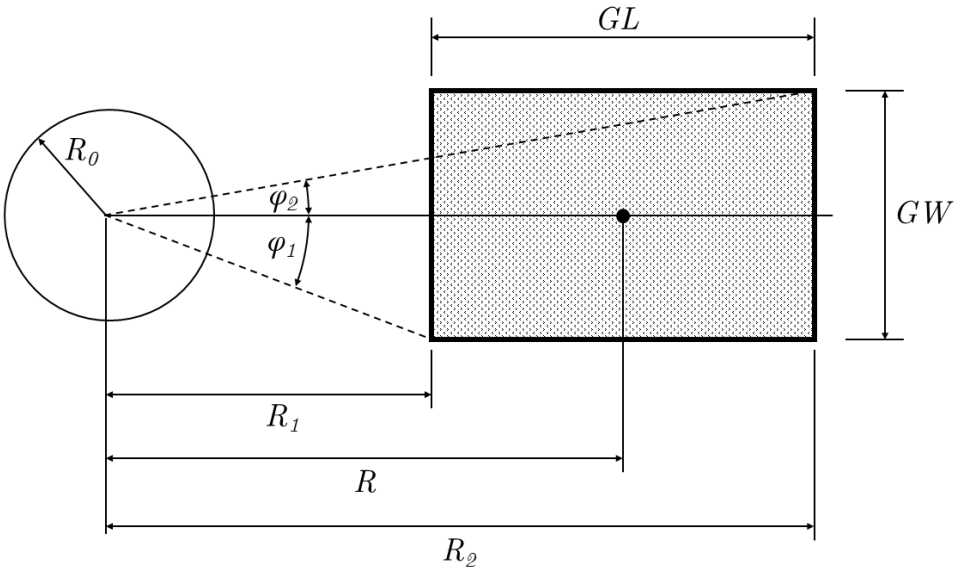

Figure 7: Geometry of a single strain gauge within a drilling rosette

In early attempts to find geometry-based calibration coefficients for uniformly stressed through holes, equations 1 and 2 were developed [40]:

$$\bar{a} = -\left(\frac{R_0}{R}\right)^2 \tag{1}$$

$$\bar{b} = -\left(4\left(\frac{R_0}{R}\right)^2 - 3(1+\nu)\left(\frac{R_0}{R}\right)^4\right) \tag{2}$$

These equations are imperfect as they do not consider the sizes of the gauges, but rather just the hole radius and the mean radius of the strain gauge grid. The size of the grid has an effect on the measured strains. Taking the size of the grid into account, the following equations are found [20].

$$\bar{a} = \frac{2{R_0}^2}{\mathrm{GL}\cdot\mathrm{GW}}\left(\phi_2 - \phi_1\right) \tag{3}$$

$$\begin{aligned}\bar{b} = \frac{2{R_0}^2}{\mathrm{GL}\cdot\mathrm{GW}}\Bigg[&2\left(1-\nu\right)\left(\phi_2-\phi_2\right)+\left(1+\nu\right)\left(sin\left(2\phi_2\right)-sin\left(2\phi_1\right)\right)\\ &-\frac{1+\nu}{8}\left(\left(\frac{R_0}{R_2}\right)^2\left(2sin\left(2\phi_2\right)+sin\left(4\phi_2\right)\right)\right)\\ &+\frac{1+\nu}{8}\left(\left(\frac{R_0}{R_1}\right)^2\left(2sin\left(2\phi_1\right)+sin\left(4\phi_1\right)\right)\right)\Bigg]\end{aligned} \tag{4}$$

When holes are drilled incrementally, these equations are used to form a matrix of coefficients of the form described in Figure 13. The cumulative calibration coefficients can be displayed graphically as seen in Figure 8.The point S indicates where a singularity in the calibration function exists. The hole depth is indicated as h and the strain gauge grid diameter as D. The singularity occurs between the hole depth to diameter ratio of 0.2 to 0.25. Hence, at depth values of greater than 20% of the mean grid diameter good results are difficult to obtain [40].

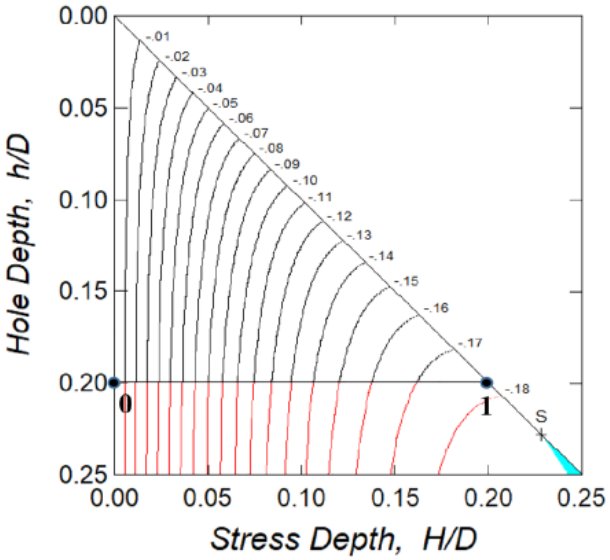

Figure 8: Contour plot of calibration function [40]

Another property that is important to consider when selecting a strain gauge rosette is the strain gauge resistance. The flow of current into a strain gauge induces heat by the relationship $P = I^2R$ where P is electrical power, I is the current, and R is the resistance. If a strain gauge is applied to a material that has a low thermal conductivity (such as Glass-fibre Reinforced Polymer (GFRP)), the gauge may start heating itself, causing the strain readings to drift [37]. In these cases, a strain gauge with a high resistance that is excited with a low voltage is preferred. The lower the voltage, the higher the uncertainty, so a balance between these factors must be achieved [37].

From the 1980s, optical methods of measuring strains on the surface of a material while drilling have been developed. Optical methods have the advantage of obtaining full-field data [30]. In other words, more information is obtained than with the gauges described in Figure 6. In most cases, the data is a little less reliable and precise than that obtained by strain gauges, but the sheer quantity of data can be used to overcome this limitation. The data obtained can be averaged and processed in a way that describes the in-plane stresses more completely than when using a strain gauge [30].

In 2009 Chen et al. [41] investigated the difference between using strain gauges and Moiré interferometry and found that in certain cases, Moiré interferometry has the power to overcome issues present when using strain gauges, such as the exact positional requirement of the drilled hole [41]. The downside to Moiré interferometry is the complexity of the experimental setup and its sensitivity to vibrations [42], limiting this method to mostly being used in a laboratory

environment [43]. An example of the resulting Moiré bands is shown in Figure 9.

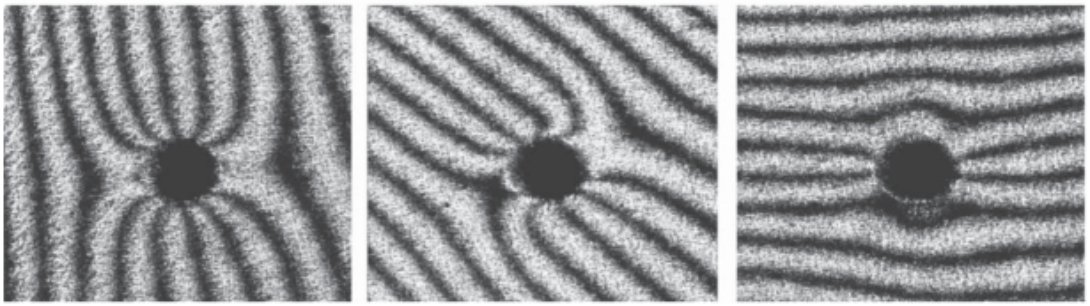

Figure 9: Examples of bands produced when using Moiré interferometry in conjunction with IHD [41]

Another popular optical method of measuring deflections is Digital Image Correlation (DIC), which uses a system of cameras in conjunction with software to map and measure the movement of characteristic marks on a specimen, thereby measuring how it deflects [42]. DIC is not affected by vibrations to the same extent as Moiré interferometry, so it is better suited for non-laboratory conditions [42].

2.2.2 Obtaining Calibration Coefficients

Obtaining the strain after drilling to each depth increment is only the first step in measuring the residual stresses. The strains measured are not at the location where the stress relief occurs, but rather at some distance away. The initial residual stresses that would result in the measured surface strains after drilling need to be determined. In 1950, Soete and Vancrombrugge devised a repeatable method for finding the initial, non-uniform residual stress from the readings obtained with a strain gauge close to the drilled hole [38]. Kelsey went a few steps further in 1956 and used a known applied load while drilling into a test specimen fitted with a strain gauge [21]. The known load was much larger than the initial residual stresses, so surface strains would largely be due to the removal of material while under an applied stress. This was useful in determining the strain response to material removal for the particular combination of material, hole geometry, and strain gauge type in question. The strain response was mathematically described by calibration coefficients derived from this test. Kelsey went further and found that the calibration coefficients differed per depth increment in the presence of not only a uniform residual stress, but in the presence of a non-uniform residual stress too [21]. Kelsey conceded that a limitation of his method is that the calibration coefficients obtained were only valid for the combination of materials, strain gauges, and hole geometries used in the test. The material and strain gauge types are not difficult to control, but the hole geometry presents a greater challenge. As such, a method was needed to quickly and cheaply obtain calibration coefficients appropriate for a given circumstance.

As computational power became more abundant, its use in conjunction with incremental hole

drilling expanded. First documented by Schajer in 1981, the use of FE allowed for the assumption that the strain distribution is the same in a blind hole and a through hole to be unnecessary. FE could now provide more detail into how a load applied to a specific depth increment affects the surface strains [20]. The determination of calibration coefficients had not only become easier and less time-consuming, it also became more accurate. Schajer described a method that used a power series to describe the unknown residual stress distribution within the material [20]. This method employs a least-squares procedure and multiple hole increments, helping to minimise noise and erroneous data. The averaging effect present limits the use of the power series method to smoothly varying residual stress profiles. By modifying the example data by random amounts within $\pm 1 \mu\epsilon$, Schajer also found the power series to be numerically unstable at orders greater than 1 [20]. In 2020, Smit and Reid found this to be incorrect by applying the power series method to a sample of aluminium that had undergone LSP. The LSP treatment induces a steep variation in residual stress, and even so, by using many depth increments, Smit and Reid found the power series solution to be numerically stable up to the 8th order at a minimum [44]. The methods' resilience to noise in the data makes it more appropriate to be used.

Given the perceived instability issue with the power series method and the ability to apply loads at any point in a FE model, the integral method became a viable alternative. The early work that led to the development of the integral method was done by Niku-Lari et al.[45] and Flaman et al.[46]. In 1985, both authors and their teams sought to find a way to use the FE approach to obtain better calibration coefficients. In 1988, Schajer published a method that could be broadly used and has more general applications [47, 48]. A previously made assumption had been that all the measured surface strains measured for a particular hole depth increment were solely due to the stress within the material removed in that increment [47]. This is untrue as the surface strains measured are due to the presence of the whole hole. Schajer proposed a method that, through FE, the strains measured on the surface could be split up into those due to the presence of the hole and those due to the last depth increment. The principle of superposition makes it possible to split the loads up in this way and find the strain response due to only the material removed. A representation of this principal is seen in Figure 10. The physical representation of the mathematics involved in the integral method are shown in Figure 13.

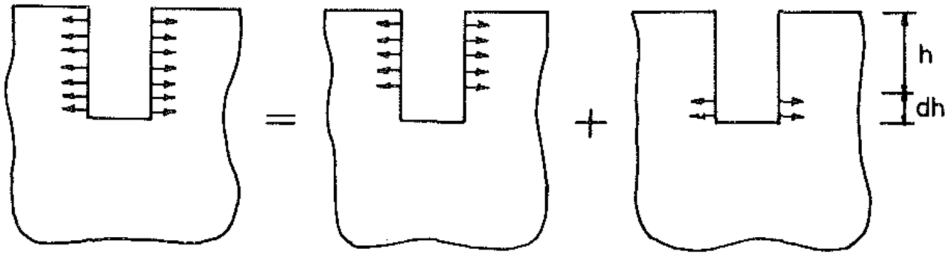

Figure 10: Principle of superposition used in the integral method [20]

In 2014, Nobre et al. [49] investigated the effect of the drilling process itself in inducing residual stresses. A load was applied to a sample, a hole increment drilled and strains recorded. A different load was applied, and the new surface strains recorded. The original load would then

be reapplied, and the next increment would be drilled. This process would be repeated until the desired final increment. A different drilling procedure would then be repeated on a similar sample and the strains for equivalent depths compared. Any differences would be solely due to the drilling process. Although not the direct point of the investigation, Nobre et al. [49] found that Ultra-High Speed Milling (UHSM) introduced less stress into the material than Computer Numerically Controlled Milling Machine (CNCMM).

Thus far in the literature survey, the research referred to has largely been applicable to isotropic materials. The research related to residual stress measurements in FRP, in particular IHD, is comparatively sparse. In 1994, Schajer and Yang investigated measurement of uniform residual stresses in orthotropic materials [50]. This method is not suitable for most laminates, as the residual stresses are discontinuous at the interface between plies. In 2003, Sicot et al. devised a method to compute non-uniform residual stress profiles with the use of FE and unit pulses [51]. Similar research was conducted by Pagliaro and Zuccarello in 2007 [52], where the determination of residual stress in homogenous orthotropic materials and composite laminates was considered. In their research, the residual stress within individual lamina was considered to be constant, and acceptable results were obtained.

In more recent work, Smit and Reid [25] evaluated the suitability of the power series method for measuring residual stresses in composite laminates. This presents a challenge in that FRP laminates have discontinuities in their residual stress profile at the interface between lamina. Although power series works best in continuous, smooth residual stress profiles, by assigning a different low order power series to each lamina, the residual stress can be measured [25]. Smit and Reid used temperatures profiles of varying orders to apply an eigenstrain to the FE model. Temperature distributions of zeroth order are readily applied to a specimen, and so verifying the calibration coefficients for holes of different depths for this load case is also readily achieved.

To overcome potential inaccuracies in the X-ray diffraction and IHD methods, Beghini et al. [53] proposed an experimental method of validating the calibration coefficients by applying a bending moment to an aluminium specimen setup in a cantiliver configuration. The specimen had undergone two treatments of LSP. The experimental setup used is shown in Figure 11. Beghini et al. found that this method produces good correlation between the FE and the measured results. The stress profiles measured varied by $\pm$ 25 MPa, but Beghini attributed this to the difference in compliance in the physical specimen and the FE model due to the attachment method used in the experiment. The method used by Beghini has the advantage of applying a large load by means of a bending moment. The larger the measured strains, the smaller the effect of noise uncertainties.

Nobre et al. [24] performed a similar investigation, albeit focusing on the depth dependent surface strain response. A horizontal tensile test machine was used to apply a tensile load to a FML specimen while IHD tests where performed. A hole would be drilled to a predetermined depth and the surface strains recorded. The load was then increased, and the surface strain response recorded. The original load would be restored and the process repeated to the next

depth increment. The apparatus used by Nobre is shown in Figure 12.

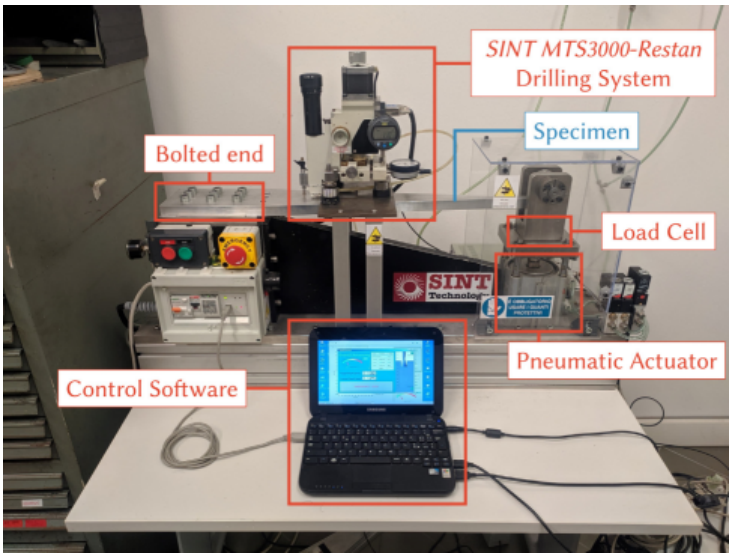

(a) Full experimental setup [53]

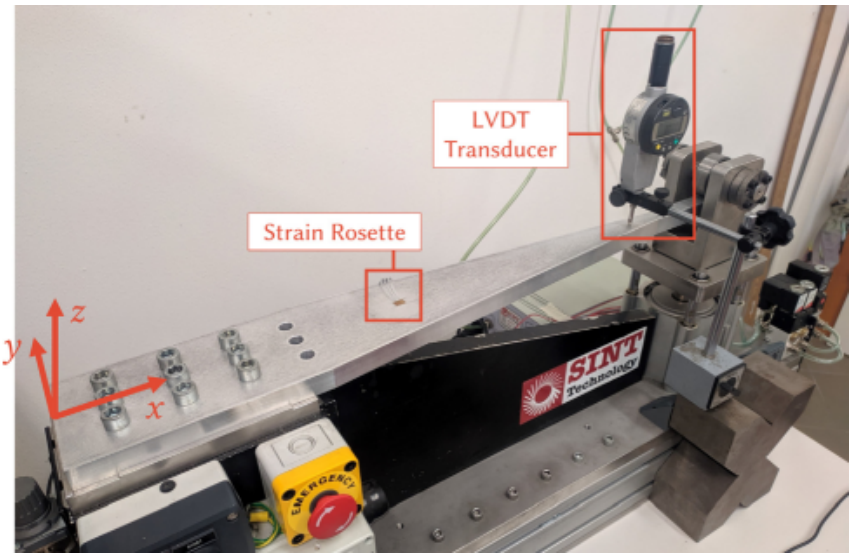

(b) Specimen setup [53]

Figure 11: Beghini cantilever experimental setup

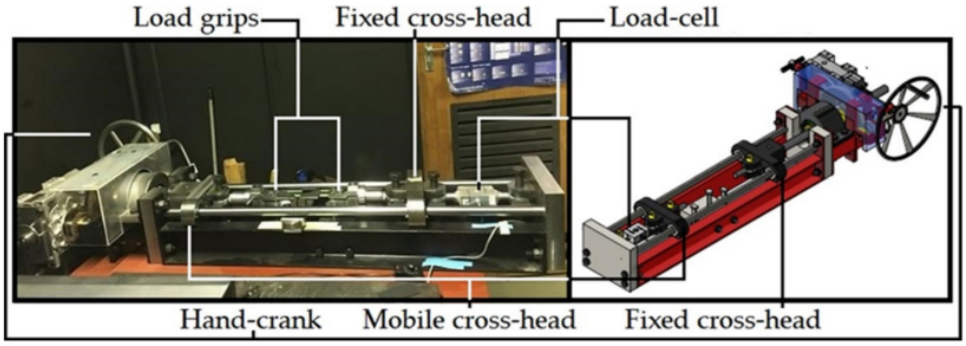

Figure 12: Nobre's horizontal tensile test apparatus [24]

As with Beghini, Nobre et al. found good correlation between the surface strains predicted by FE and those measured experimentally. Both methods have the advantage of introducing large,

easily measurable strains. Both methods require a large, stiff apparatus to hold the specimens in place without introducing undesired loads. For the apparatus to fulfil this role it must be large and built of heavy materials, limiting the scenarios in which they can be applied. Additionally, controlled tensile and bending loads are not always easy to apply to a specimen. Both of these methods are therefore limited to laboratory use.

2.2.3 Mathematical Rational

The four relaxation methods mentioned in the introduction of this chapter may seem quite different as they utilise different cutting geometries, but the measurement and processing of measured strains are very similar. For relaxation methods, the residual stresses originally present in a material can be related to the measured strains by the following integral equation [12],

$$d(h) = \int_{h_0}^{h} g(H,h)\sigma(H)dH \tag{5}$$

where $\sigma(H)$ is the residual stresses at all depths H before material is removed, and $d(h)$ is the strain of the material at a location close to where material is removed to depth h. The term $g(H,h)$ quantifies the relationship between the strain when material is removed and the original residual stresses, and is the term that differs depending on the relaxation method used, the cut geometry, the strain gauges used, and in the case of FRPs, the laminate configuration.

The geometries involved in the layer removal and Sachs' methods are relatively simple thus making an analytical solution of equation 5 possible [12]. For more complex cutting sequences such as those used in IHD and the slitting method, empirical solutions or those obtained with the aid of FE models are typically used [20]. FE methods are usually preferred due to the increased accuracy and relative availability of computational power.

Equation 5 cannot be solved directly when performing IHD or using the slitting method. Instead, forward and inverse solutions must be used. These steps are necessary because the unknown variable ($\sigma(H)$) in Equation 5 is within the integral. In the forward solution, a known stress distribution, or a computational representation thereof, is applied to a specimen. Material is then incrementally removed and the surface strain response due to the removal of material is recorded for each increment. Depending on the method used, the surface strains of interest may differ. The surface strains obtained due to the known applied load are then used to obtain calibration coefficients. This is commonly done with the use of a FE model. The calibration coefficients are used in the inverse solution to determine the initial residual stress state that would have resulted in the observed surface strains in the test specimen[15].

In determining the forward solution, the stress distribution is often described using the sum of a series. Great care is needed in the selection of the series as it must be adequately able to represent the solution, along with being linearly independent. Some commonly used functions include: unit pulses, power series, and Legendre polynomials, the first two being algebraically simple but not necessarily obeying equilibrium, while the latter is complex but always satisfies

the requirements of equilibrium [12]. There are ways to ensure that whatever method is used maintains internal equilibrium, such as the use of an applied eigenstrain [44]. Eigenstrains are initial strains in a material that generate a stress field. One of the most common sources of these strains are thermal [54]. The stress field produced is self-equilibrating [55], making a temperature-induced eigenstrain suitable for the forward solution. The function chosen is applied as a load to a FE model representing the test specimen. All increments of material removal under the chosen load must be applied, and the surface strain responses at the location of the strain gauges recorded for each depth increment. These strains are called calibration coefficients. Using the calibration coefficients and the experimentally measured surface strains, the inverse solution computes the residual stress distribution within the sample. The specifics of how the FE model is set up for the forward solution and how the inversion of the calibration coefficients is performed in the inverse solution is dependent on the method used, namely power series expansion or the integral method [47] which are the most common.

The integral method employs the use of the sum of a basis series ($u_i(H)$) multiplied by some coefficients (c_i) to express the unknown function ($\sigma(H)$) in equation 5. The expression is shown in Equation 6. A unit pulse is often used as a basis equation.

$$\sigma(H) = \sum c_i u_i(H) \tag{6}$$

The calibration coefficients are denoted by the matrix G_{ij} and are found through FE. They represent the expected strain response if a unit pulse is applied at depth j in a hole of depth i. This concept can be more clearly seen in Figure 13.

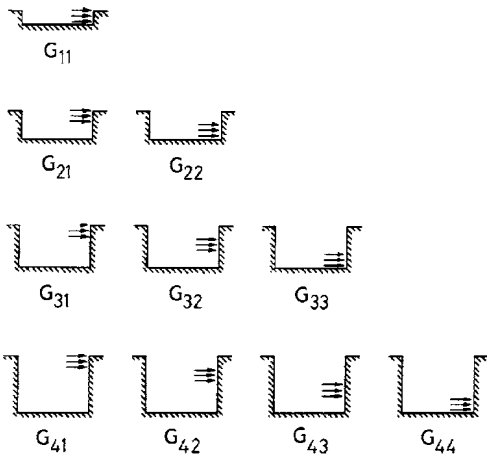

Figure 13: Physical interpretation of matrix G_{ij} for the hole drilling method [12]

Having obtained the calibration coefficients and measured the strains after each increment of material removal, the undrilled residual stresses can be obtained by equation 7:

$$\boldsymbol{\sigma = d\, G^{-1}} \tag{7}$$

where d is a vector representing the measured strains.

With the calibration coefficients being represented by a lower triangle matrix, the results are sensitive to measurement noise and may be distorted by steep stress gradients [44]. The use

of Tikhonov regularization [56] is often employed to smooth out the effects of noise and has been shown to produce reliable results [12], however, it does have its limitations and intricacies. The tuning of the parameters involved in Tikhonov regularization to minimise the noise is an iterative process, but the assumption of slowly varying curvature in the stress field can be used on isotropic materials [12]. This assumption does not hold true globally for FRPs. Within a single ply the stress field varies slowly, but a stress discontinuity may be present between plies, and therefore more iterations are required to achieve acceptable regularization [25]. To overcome this issue, Smit and Reid [44] proposed a temperature gradient described by a power series expansion. As with the integral method, calibration coefficients are obtained, but these are found using a power series expansion of eigenstrains of order n within individual plies. The eigenstrains are applied to the FE model by means of through-thickness temperature distributions and dummy CTEs. The residual stress distribution is described by Equation 8:

$$\begin{aligned}\sigma_x(z) =& a_{x0}s_{x0}(z) + a_{x1}s_{x1}(z) + a_{x2}s_{x2}(z) + ... \\ &+ a_{y0}s_{y0}(z) + a_{y1}s_{y1}(z) + a_{y2}s_{y2}(z) + ... \\ &+ a_{xy0}s_{xy0}(z) + a_{xy1}s_{xy1}(z) + a_{xy2}s_{xy2}(z) + ...\end{aligned} \tag{8}$$

where s_{jn} is part of an expandable stress distribution occurring when an eigenstrain of order n is applied in direction j, a_{jn} is an unknown amplitude, and $\sigma_x(z)$ is the residual stress distribution in direction x at z depth.

Similarly, the strain response can be characterised by Equation 9:

$$\begin{aligned}\epsilon_x(z) =& a_{x0}c_{x0}(z) + a_{x1}c_{x1}(z) + a_{x2}c_{x2}(z) + ... \\ &+ a_{y0}c_{y0}(z) + a_{y1}c_{y1}(z) + a_{y2}c_{y2}(z) + ... \\ &+ a_{xy0}c_{xy0}(z) + a_{xy1}c_{xy1}(z) + a_{xy2}c_{xy2}(z) + ...\end{aligned} \tag{9}$$

where c_{jn} is the strain response in the given direction (in this case x) due to the component of the nth order eigenstrain in the j direction.

For ease of visualisation and calculation, Equations 8 and 9 can be written in matrix form as Equations 10 and 11 respectively:

$$\sigma = S \cdot A \tag{10}$$

$$\epsilon = C \cdot A \tag{11}$$

The C matrix contains the results of the forward solution found through FE, the calibration coefficients. The A matrix represents the amplitudes that are applied to the eigenstrain functions so that the results best match the measured strain. This is the first quantity to be calculated in the inverse solution. To isolate the A matrix, Equation 11 must be manipulated as seen in Equation 12:

$$\begin{aligned}C^T \cdot \epsilon &= C^T \cdot C \cdot A \\ A &= (C_T \cdot C)^{-1} \cdot C^T \cdot \epsilon\end{aligned} \tag{12}$$

Having found the resulting A matrix, the initial stress distribution can be found using Equation 8.

2.3 Gap in Existing Literature

Through this literature survey, the importance of accurate drilling, measuring, and processing of the data for obtaining residual stress measurements has been emphasised. Small errors can be accounted for, but need to be considered to obtain useful information. The reliance on FE has only grown along with the abundance of computing power available. The accuracy of the residual stress measurements taken are directly tied to that of the FE model used and whether the FE package used is modelling reality correctly. In the same way that Beghini et al. [53] and Nobre et al. [24] were able to apply an external load to a specimen and verify whether the strains obtained were equivalent to those computed with FE, the power series method used by Smit and Reid [44] can also be verified for the zeroth order by the application of a thermal load. The use of a thermal load applied to a FRP specimen has the advantages of requiring only a simple temperature controlled environment and strain measuring equipment. Additionally, a method using temperature to apply an eigenstrain will not be affected by support constraints as is the case when applying a tensile or bending load. A procedure requiring verification of calibration coefficients using a thermal load could also be applied in-situ, making the procedure more versatile than those previously mentioned.

3 Research Question

How well do strains predicted by FE correlate with the strains that would be present in an FRP specimen given the presence of a hole of some depth and a change in temperature? Can the zeroth order calibration coefficients of power series expansion be found without the use of FE by the introduction of a thermal load to a physical sample?

4 Objectives

The objective of this work is to assess whether calibration coefficients (and hence surface strains) predicted by FE correspond to those measured experimentally in the presence of uniform thermal loading. In the pursuit of this objective, the following sub-objectives will be completed:

- Develop a means of applying a suitably large and stable thermal load to a specimen.
- Obtain surface strains resulting from thermal loading applied to a pre-drilled laminate.
- Assess obtained surface strains against those predicted by FE.
- Determine whether the measured and predicted surface strains match, thereby assessing the accuracy of calibration coefficients obtained from zeroth order terms of series expansion IHD method.

5 Research Method

The verification of calibration coefficients obtained through FE requires the use of both a computational model and physical experimentation. Special care must be taken in the execution of physical experimentation for any investigation as there are often various sources of error that need to be mitigated against. When using IHD to measure residual stresses in FRPs, the undissipated heat generated by mechanical drilling may damage the matrix, resulting in non-representative surface strain readings. Additionally, the use of too high an excitation voltage may result in too much power to be fully dissipated into a composite laminate and thereby yield incorrect readings. To ensure that the IHD method produces reliable results, it needs to be validated against a known applied load.

In this investigation, pre-drilled holes are used to ensure that all measured surfaces stains are solely due to the applied load and the presence of a hole. This ensures that the physical experimentation is aligned with that modelled by FE. The othrotropic nature of GFRP allows a thermal load to be used to induce internal stresses. It is difficult to experimentally apply a temperature profile of an order greater than zero. Therefore, a computational model that is limited to a zeroth order thermal load and that may be used with the series expansion method is created. A thermal load is applied computationally and experimentally and the results between the two compared. For IHD to be suitable in the determination of residual stresses, the results of this investigation obtained by FE must correlate to those obtained by physical experimentation within the appropriate margin of error.

5.1 Experimental

5.1.1 Specimen Preparation

The experimental process was performed on GFRP laminates consisting of E-Glass fibres and an epoxy matrix. Plates of $[0_2/90_2]_s$ and $[0/90/+45/\text{-}45]_s$ configuration were manufactured from prepreg material with fibre volume fraction (V_f) of approximately 60% and a ply thickness of approximately 200 μm. The prepreg material was supplied by c-m-p gmbh (product code: T-GE-1 250/635 CP002). The final manufactured plates had a thickness of approximately 1.6 mm. The plates were cured between two stainless steel plates to ensure a good surface finish.

A test specimen measuring 45×310 mm was cut from the $[0_2/90_2]_s$ plate. The top view of the sample is shown in Figure 14. Ten Kyowa KFGS-1.5-120-D28-23 hole drilling foil strain gauge rosettes were glued to the sample's top surface as per manufacturer specifications. The relevant properties of the rosette are tabulated in Table 1. The centre of each gauge, i.e. where the hole was to be drilled, was positioned a minimum of 20 mm from the edge and 30 mm from the next

hole to avoid edge effects. Starting from the left, as seen in Figure 14, holes were drilled with depths starting at 0.9 mm and ending at 0.1 mm, each varying by 0.1 mm. The right-most rosette was left undrilled. As the information of interest is the strains due to the presence of a drilled hole to a certain depth, the undrilled rosette acted as the zero reference and as the dummy gauge for temperature compensation.

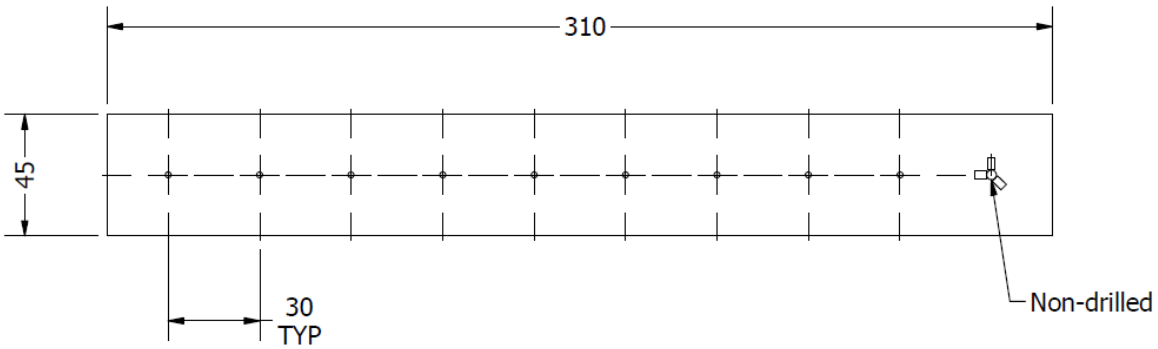

Figure 14: Plan view of $[0_2/90_2]_s$ specimen indicating how the holes are located

Table 1: Kyowa KFGS-1.5-120-D28-23 specifications

	Strain gauge rosette grids		
	0°	90°	135°
Gauge Resistance (Ohms)	$119.6 \pm 0.4\%$	$119.6 \pm 0.4\%$	$119.6 \pm 0.4\%$
Gauge Factor	2.10	2.09	2.08

IHD was performed with a Sint Technology Restan MTS 3000 with a pneumatic turbine. Although this investigation is concerned with the final drilled holes and not the incremental nature of IHD, using the IHD method ensures that the specimen is not damaged by elevated heating and that cracking and delamination are less likely. At this stage, it was unnecessary to collect the strain release data, so the gauges were glued, but not wired up to a Data Acquisition (DAQ) system. The holes were drilled with a 1.6 mm diameter tungsten carbide inverted cone end mill in increments of approximately 10 μm at a feed rate of 0.1 mm/min. This resulted in holes of approximately 1.9 mm in diameter. Once drilled, the sample was ready to undergo the temperature tests.

A similar preparation process was used for the $[0/90/+45/\text{-}45]_s$ laminate. The 45° plies in this laminate allow for the further investigation of the approach used on the $[0_2/90_2]_s$ laminate on a more complex laminate. Therefore, only 3 holes were drilled: 0.2, 0.4, and 0.6 mm deep. The top view of the sample is shown in Figure 15. Preliminary tests performed with the $[0_2/90_2]_s$ laminate indicated that self-heating of the rosettes may lead to issues if the rosettes are too close to one another. The minimum distance between the centre of the rosettes was accordingly increased to 40 mm. As with the $[0_2/90_2]_s$ specimen, an undrilled reference rosette was also used.

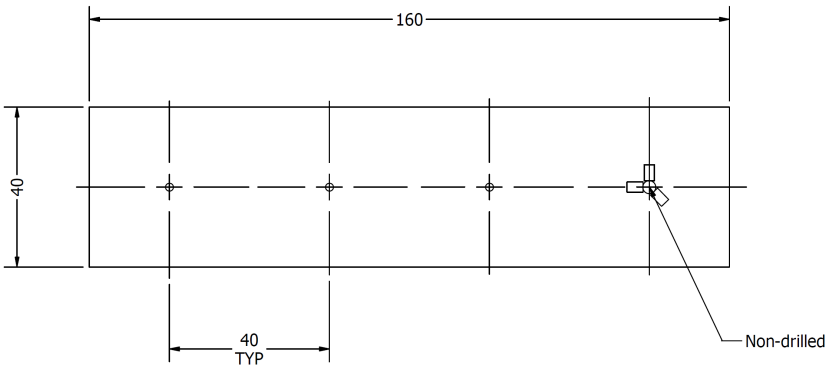

Figure 15: Plan view of $[0/90/45/\text{-}45]_s$ specimen indicating how the holes are located

5.1.2 Determination of Lamina Properties

In addition to the $[0_2/90_2]_s$ and $[0/90/+45/\text{-}45]_s$ plates, plates of $[0_4]_s$ and $[0/90/0/90]_s$ configuration were also manufactured from the same prepreg material to be used in conjunction with the ASTM D 3039 [57] and ASTM D 3518 [58] standards to determine the unidirectional lamina properties. These standards comprise mainly the tensile testing of unidirectional material coupons with strain gauges applied to find the Young's moduli, the shear modulus, and Poisson's ratio of the material. The above-mentioned laminate configurations were cut in a manner to produce six of each required coupon configuration: $[0_4]_s$, $[90_4]_s$, and $[+45/\text{-}45/+45/\text{-}45]_s$. All six coupons of each configuration were individually measured and tested, and their calculated properties averaged.

CTEs were found using Lanza Di Scalea's method [59]. Identical strain gauges were applied to a unidirectional GFRP sample and an Aluminium 1050 sample with known CTE [60]. Both samples were subjected to the same change in temperature. The difference between the strains measured on the GFRP sample and the aluminium sample were divided by the change in temperature and added onto the known CTE of the aluminium sample. Both the longitudinal and transverse CTEs of the unidirectional GFRP specimen were measured.

The lamina properties obtained are summarised in Table 2. The uncertainties for all properties except for the CTEs are assumed to be the same as those used by Smit and Reid [25] when evaluating the same material cured in the identical manner. The Poisson's ratio (ν_{23}) was taken from the micromechanics estimates obtained by Smit and Reid [25]. The uncertainties related to the CTEs were obtained by Monte Carlo simulation and are further explained in Section 5.4.2. All uncertainties in Table 2 are representative of one standard deviation. The properties in the through-thickness direction can be assumed as equivalent to those in the transverse direction due to rotational symmetry around the fibre direction.

Table 2: Lamina ply properties

Property, (Units)	Magnitude, Uncertainty
Longitudinal Modulus, E_1 (MPa)	37841.3, 1.986%
Longitudinal CTE, α_1 ($10^{-6}/°C$)	8.38, 5.39%
Transverse Modulus, E_2 (MPa)	9912.85, 2.223%
Transverse CTE, α_2 ($10^{-6}/°C$)	43.17, 15.07%
Shear Modulus, G_{12} (MPa)	3152.89, 2.582%
Poisson's Ratio, ν_{12}	0.3154, 2.078%
Poisson's Ratio, ν_{23}	0.4124, 5%

5.1.3 Controllable Temperature Environment

5.1.3.1 Physical Construction

To elicit a meaningful strain response to a change in temperature, the temperature to which the specimen is being exposed to needs to be known. Furthermore, the temperature needs to remain constant for a prolonged period of time so that the specimen can reach a steady thermal condition throughout. A Dual-Chamber Controllable Temperature Environment (DCCTE) was constructed to provide a constant temperature environment. The main material used was polystyrene as it offers excellent insulating properties. The outer chamber contains two 100 W incandescent light bulbs, two 12 V 80 mm computer fans, and an LM32 temperature sensor. The walls of the outer chamber are made of 6 pieces of 50 mm thick polystyrene. The inner chamber houses the test specimen, an LM32 temperature sensor and a HBM TT-3/100 foil temperature sensor glued to a small sample of unidirectional laminate. The walls of the inner chamber are made of 20 mm thick polystyrene. All polystyrene panels are bonded using polystyrene adhesive. A schematic of the DCCTE is shown in Figure 16.

The dual-chamber design facilitated the two main requirements of the apparatus. The outer chamber with its thicker walls prevents the escape of thermal energy from the system. It is also the chamber where the temperature is actively controlled. The inner chamber, where the test specimen was placed, has thinner walls. This acts as a thermal damper, smoothing out the transient temperature variations that are unavoidable in the outer chamber. The temperature in the inner chamber is therefore more constant, allowing the test specimen to reach a steady temperature where strain readings can be taken.

5.1.3.2 Temperature Control

This investigation required precise temperature control. The strain response of the material is wholly determined by the temperature applied, and hence the specimen must reach a state of thermal equilibrium. The DCCTE must be able to achieve a high temperature range to increase as far as possible the thermal strains in the system. To achieve this, a temperature control

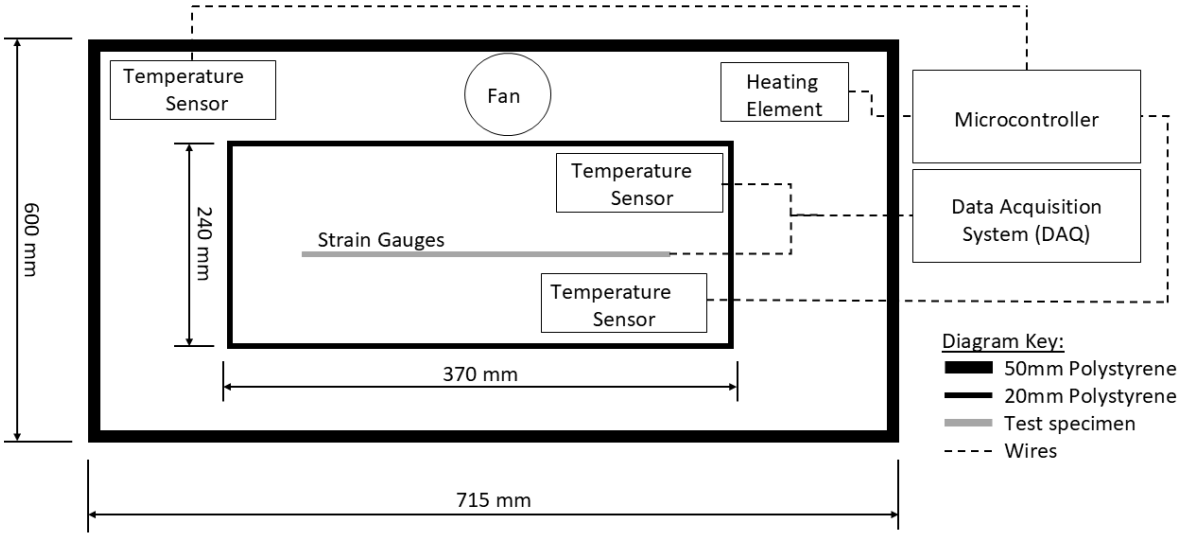

(a) Top View

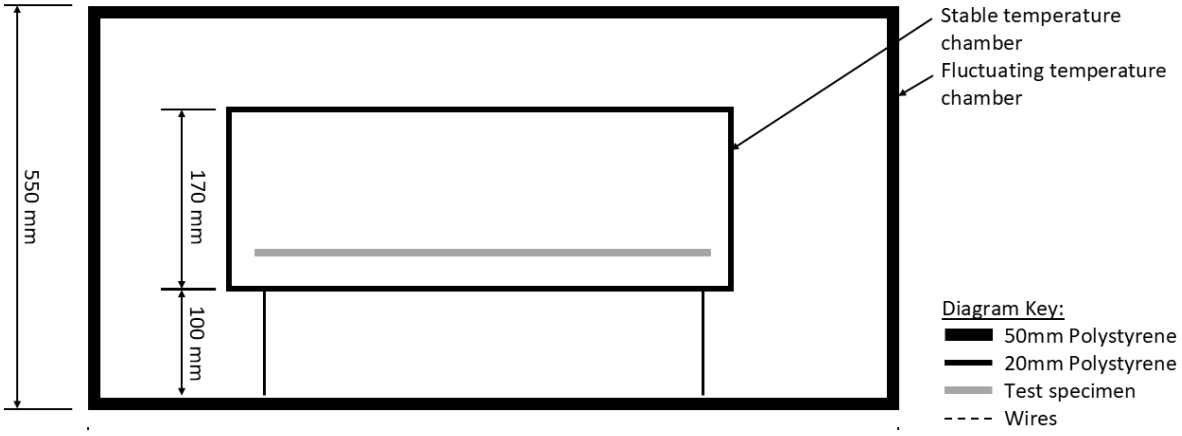

(b) Side View

Figure 16: Schematic diagram of DCCTE and associated equipment - not to scale

system is needed.

Incandescent light bulbs are an easy means to introduce heat energy as they are inefficient at creating light energy, and therefore two 100 W incandescent light bulbs were used for that purpose. Two 12 V 80 mm computer fans were used to assist the dissipation of heat throughout the chamber by convection. They also had the secondary effect of ensuring that polystyrene surfaces subjected to thermal radiation from the light bulbs did not get hot enough to cause melting.

A source of thermal energy alone cannot ensure that an enclosed environment reaches some steady-state temperature. It needs to be controlled. In the case of incandescent light-bulbs, the voltage input determines the intensity of the light and thermal energy output. In the past, lighting in households could be dimmed with a simple variable resistor. Although this would work for the purposes of controlling the heat output of the light bulbs, the results would be crude and maintaining the chamber at a set temperature would be labour-intensive. Ideally, an electronic control system should be used. In this investigation, an Arduino UNO microcontroller

in conjunction with a Robotdyn 1 Channel AC Dimmer Module was used. The dimmer module makes use of a TRIAC (a component that allows current to flow when triggered) to control what fraction of the AC sine wave flows through the light bulb. If less of the sine wave is used, the bulb shines dimmer. With the dimming module it is possible to automate the change in brightness of the light bulb as a result of another measured value.

The ultimate purpose of the light bulb is to increase the temperature of the outer chamber of the DCCTE. The Arduino and Robotdyn modules control the power supply to, and thus the heat output of, the light bulbs. The requirement of the control system is to maintain the heat inside the DCCTE at a certain temperature. A way of determining the current temperature inside the DCCTE is therefore necessary. An LM32 temperature sensor was used to measure the temperature and feed it back to the Arduino microcontroller. The output of the LM32 sensor was found to be within ±0.5°C of a thermocouple and the HBM TT-3/100 temperature sensor mentioned in Section 5.1.3.1.

Arduino code was developed that makes use of PID control to keep the temperature inside the DCCTE at some set point by actively controlling the power supply through the Robotdyn AC dimmer module depending on the outer chamber temperature read by the LM32 temperature sensor. The code allows for the set point to be modified at any time. A control block diagram of the temperature control system is shown in Figure 17.

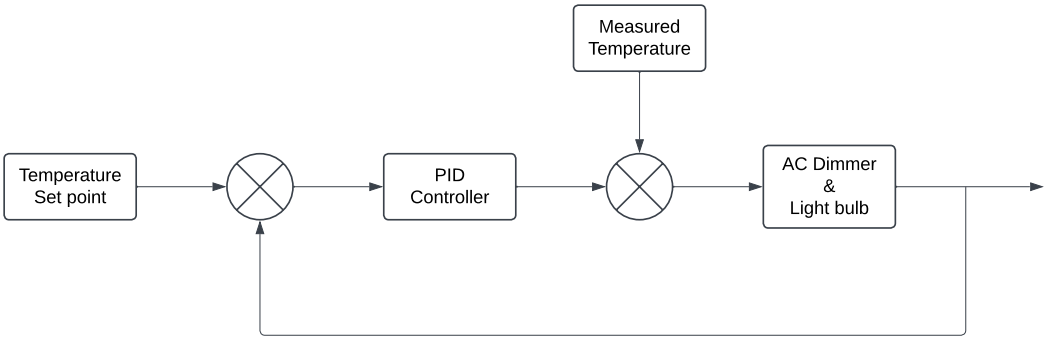

Figure 17: Control block diagram for DCCTE temperature controller

Through testing, it was found that the maximum temperature that the DCCTE could reliably reach was 70°C. Any higher and the controlled temperature would become erratic. This may be due to the insulation not being sufficient, and thus at higher temperatures too much heat energy is leaked into the external environment for the temperature to stay consistent. Another limitation of the DCCTE is that it can only introduce heat energy. It cannot cool the chamber down. If a range of temperature greater than from ambient temperature to 70°C is required, a cooler minimum temperature is needed. Since the DCCTE is insulated, this can be achieved by introducing something cool into the environment. With the introduction of 10 kg of dry ice, it was found that the DCCTE could be cooled to a temperature of between -30°C and -40°C. Therefore, in conjunction with the use of dry ice, the DCCTE can achieve a temperature range of up to 110°C. A limitation of the use of dry ice to cool the DCCTE is that as the dry ice

sublimates, the surface area thereof decreases, causing the minimum temperatures to fluctuate. This fluctuation is not large and valid results can still be obtained by taking the final strain readings at one of the temperature peaks or troughs.

5.1.4 Experimental Apparatus

Much of the equipment discussed thus far has to do with the temperature control of the DCCTE. In addition to the Arduino UNO microcontroller, AC dimming module, LM35 temperature sensor, light bulbs and fans used, specialised measurement equipment was employed to read the strains and temperature data from the specimen.

HBM QuantumX MX1615B DAQ

A 16-channel HBM DAQ was used in conjunction with catmanEASY version 5.0.1.39 to measure and record strain and temperature data obtained from the test specimen within the DCCTE.

HBM TT-3/100 foil temperature sensor

The HBM TT-3/100 foil temperature sensor is a platinum-based temperature sensor that is indicated for the measurement of surface temperature. It's electrical resistance is dependent on the room temperature. Each batch is calibrated by HBM and a measurement polynomial provided in the packaging. It is applied to the sample in the same manner as a strain gauge.

5.1.5 Strain Gauge Self-heating Mitigation

The use of strain gauges on composite materials presents a challenge regarding the thermal output of the strain gauge. As mentioned in Section 2.2.1, the magnitude of thermal output is governed by the strain gauge resistance and the excitation voltage used. The strain gauge resistance is an intrinsic property of the strain gauge and therefore cannot be changed, however the excitation voltage used can be changed. In general, the larger the excitation voltage, the better the reading resolution. A higher voltage is also accompanied by a higher thermal output.

Although a higher thermal output is generally not a problem when strain gauges are used on materials with a high thermal conductivity, such as most metals, GFRPs have a low thermal conductivity. This reduces the thermal energy dissipated into the environment. 350 Ω strain gauge rosettes have sometimes been used when performing IHD on GFRPs, as the higher electrical resistance allows for a higher excitation voltage to be used without excessive self-heating. 350 Ω strain gauge rosettes seem to no longer be manufactured so 120 Ω strain gauge rosettes were used instead. An excitation voltage of 0.5 V is often used with 120 Ω strain gauges applied to GFRPs, however the strains measured in this investigation are low and higher resolution was

required. The effect of using an excitation voltage of 2.5 V within the temperature range of the thermal tests was therefore investigated.

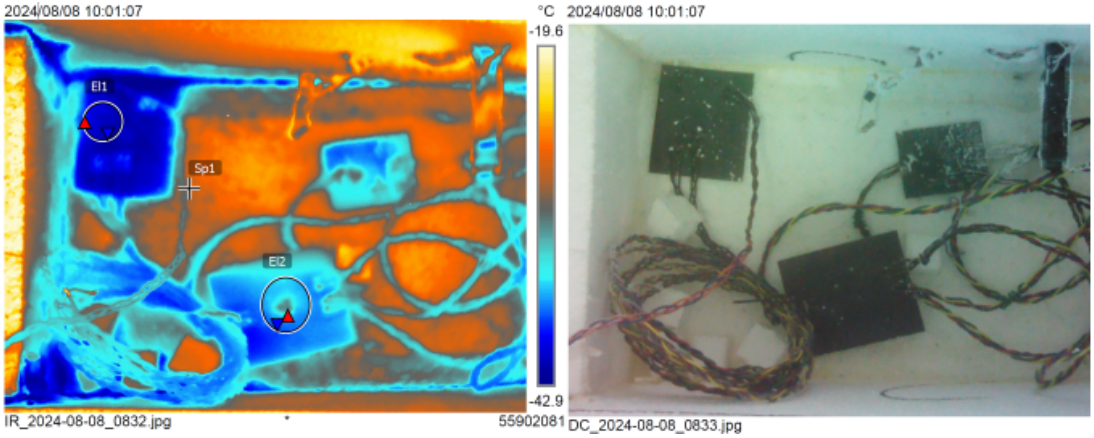

(a) Ambient temperature: -40.6°C

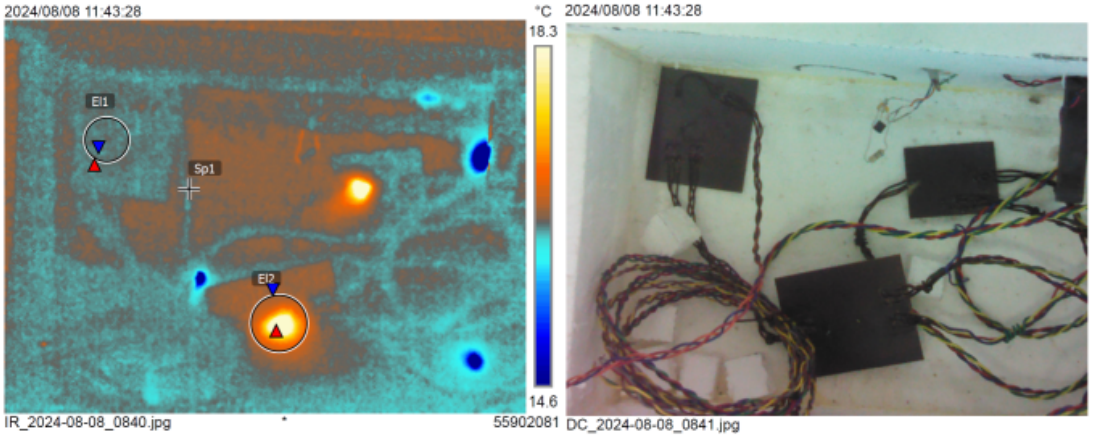

(b) Ambient temperature: 16.3°C

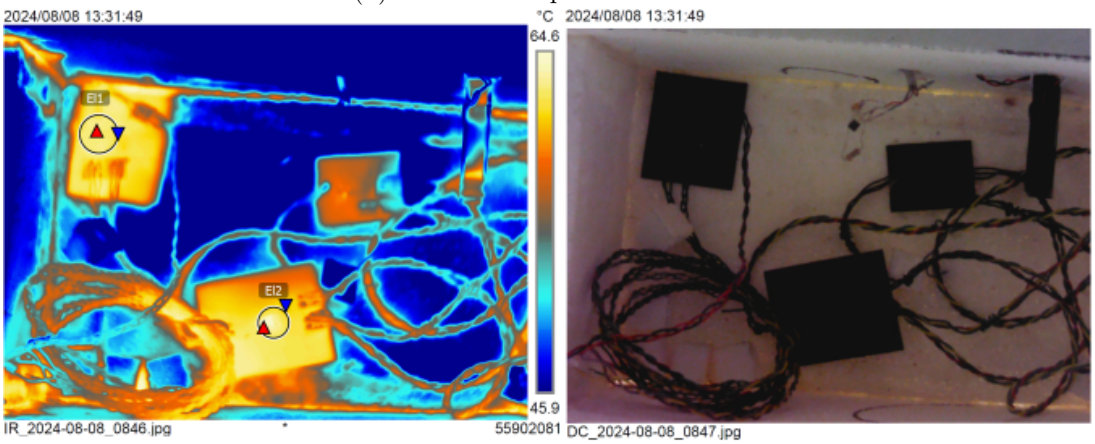

(c) Ambient temperature: 62.6°C

Figure 18: Thermal images of strain gauges energised to 2.5 V on a GFRP specimen

A FLIR T640 thermal camera was used to measure the temperature difference between two laminates, each with a Kyowa KFGS-1.5-120-D28-23 hole drilling strain gauge rosette. One was energised to 2.5 V and the other was not energised. The temperature was measured at three different temperatures within the expected test temperature range. Both of the specimens were lightly coated with black matt spray paint to avoid the measurement of reflected infrared

waves. After the temperature equalised, the lid of the DCCTE was removed and thermal images immediately taken. The thermal images are shown in Figure 18. In all images, the region labelled "El1" (top left) corresponds to the laminate with the non-energised strain gauge rosette and the region labelled "El2" (closer to the centre) corresponds to the laminate with the energised strain gauge rosette.

Four images were taken of the specimen at both the -40.6°C and 16.3°C state, but due to the rapid cooling of the specimen when the DCCTE lid was removed, only two images were taken of the specimen at 62.6°C. For each image, the hottest temperature around the strain gauge was recorded. An average temperature difference between the strain gauge temperature and the respective ambient temperature was found, the results of which are plotted on Figure 19.

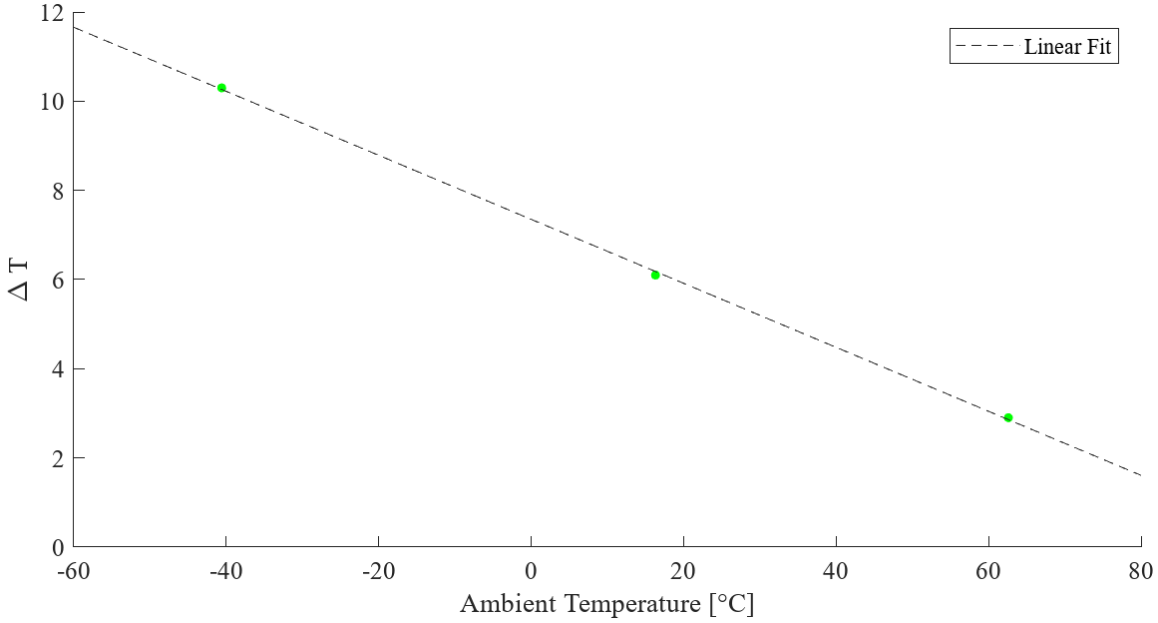

Figure 19: Difference between temperature measured at a strain gauge rosette energised to 2.5 V and ambient temperature

It was found that the difference between the temperature around the strain gauge rosette and the ambient temperature is linear in the region tested. The larger the ambient temperature, the smaller the difference between the measured temperatures. The uncertainty in the temperature can therefore be quantified and taken into account. Additionally, preliminary tests showed minimal strain drift at a steady ambient temperature. Therefore, 2.5 V can be used as an excitation voltage.

5.1.6 Experimentation

A summary of the apparatus and specimens used is shown in Table 3. Being able to use an excitation voltage of 2.5 V allows for a higher strain sensitivity. Changes in temperature achievable by the DCCTE produce lower strain responses as compared to an applied axial or bending load, therefore higher strain sensitivity is required. Excess heat was generated and

there was a potential for the self-heat generated from adjacent rosettes to affect the strain measurements at each hole. To avoid this, two separate tests were run. The first was with the even depth holes (i.e. 0.2 mm, 0.4 mm, 0.6 mm, and 0.8 mm deep) connected to the HBM QuantumX MX1615B DAQ, and the second was with the odd depth holes (i.e. 0.1 mm, 0.3 mm, 0.5 mm, and 0.7 mm) connected. From here on, the holes drilled to even depths will be referred to as "Set A", and the holes drilled to odd depths will be referred to as "Set B". In both cases, the undrilled rosette was also connected. The DAQ in conjunction with the CATMAN software was used to measure and record the strains from the rosettes and the temperature from the HBM TT-3/100.

Table 3: Summary of apparatus and materials used

Equipment / Instrumentation / Material	**Description**	**Quantity**
Dual Chamber Controlled Temperature Environment	Apparatus to control the temperature that the specimen is exposed to.	1
LM35 Temperature Sensor	Temperature sensor used to measure temperature inside the two chambers of the DCCTE	2
80 mm DC fan	Fan circulating the air within the outer chamber of the DCCTE.	2
100 W incandescent light bulb	Introduces heat in to the outer chamber of the DCCTE.	2
Arduino Uno microcontroller	Microcontroller controlling the electrical power sent to the light bulbs depending on the temperature of the DCCTE.	1
Robotdyn 1 Channel AC Dimmer Module	Microcontroller module that can set a light bulb to a chosen brightness.	1
HBM QuantumX MX1615B DAQ	16-channel data acquisition system used to record the temperature and strain data from the specimen.	2
Sint Technology Restan MTS 3000	Specialised incremental hole drilling machine	1
Kyowa KFGS-1.5-120-D28-23 strain gauge rosette	Hole drilling strain gauge rosettes to measure the strain response around the predrilled holes on the specimens.	14
HBM TT-3/100 foil temperature sensor	Platinum-based resistive temperature sensor measuring the surface temperature of the specimen.	1
$[0_2/90_2]_s$ Laminate	GFRP laminate manufactured using c-m-p TGE-1 250/635 CP002 prepreg.	1
$[0/90/+45/-45]_s$ Laminate	GFRP laminate manufactured using c-m-p TGE-1 250/635 CP002 prepreg.	1

Although a half-bridge configuration with a reference rosette for every active rosette would have been preferred for temperature compensation, it is much simpler to create a computational half-bridge with the undrilled rosette during data processing. Therefore, all the strain gauges were connected in quarter-bridge configurations. The compensation was performed after the fact by subtracting the strains measured at the reference gauges from all the other active gauges. A sample rate of 10Hz, and a 2Hz Bessel low-pass filter was used.

The specimen was placed in the inner chamber of the DCCTE, flat and supported on each corner by a small cube of polystyrene. The specimen did not make contact with the walls of the inner chamber as this would restrict its movement, inducing unwanted strains. The small laminate sample with the HBM TT-3/100 temperature sensor was also placed inside. This is important as the temperature values to be used in the results were from this sensor, not the LM32 sensor because the TT-3/100 sensor is more accurate and is applied directly to the surface of a laminate sample. The LM32 sensor measures air temperature which will be used to control the power supply to the light bulbs. The inner chamber was then closed while ensuring that the strain gauge wiring did not constrain the specimen. After inspecting that the fans were running and that the light bulbs were in place, the outer chamber was closed while making sure the wiring was out of the way.

During proof of concept tests, it was found that ambient air humidity was penetrating the laminate and causing some of the initial proof of concept tests to exhibit results that presented a large deviation from those predicted by FE. To mitigate this, the DCCTE was heated with the specimens inside to 70°C overnight for at least 10 hours. It was assumed that after this time all the moisture in the laminate specimen would have escaped and all subsequent measurements in that test would be unaffected by changes in moisture content within the laminate. This heat soak also had two other benefits. The overnight heating ensured that all components in the DAQ had warmed up and were not drifting, and that the sample was at the steady-state condition throughout its entire length and thickness required for the results to be valid.

At this point, the strain readings were all reset to zero and the DAQ recording of strains started. After a minute, the light bulbs were turned off. The outer chamber of the DCCTE was opened, the light bulbs removed and 10kg of dry ice was added. The light bulbs were removed as they are sensitive to sudden changes in temperature, and the dry ice was added to reduce the temperature in the box substantially. Cooling the specimen was found to yield better results than heating, likely due to moisture that may have made its way into the specimen. After adding the dry ice, the outer chamber of the DCCTE was closed.

The temperature within the DCCTE was monitored. The test continued until a stable minimum temperature was reached. Once the strains at the minimum temperature were recorded over a one-minute period, the DCCTE was opened to allow it to warm up, and after it reached room temperature, the light bulbs were reinserted. The whole procedure was subsequently repeated with the odd depth holes, or those of Set B.

5.2 Verification of Experimental Method

5.2.1 Thermal soak

Three main types of data were recorded: strains (in the 0°, 90°, and 45° directions around the holes), temperature and time. Special care was taken to ensure that the strain and temperature readings were not affected by any factors that are not related to the temperature of the specimen. The first step in obtaining surface strain results is heating up the specimen to the maximum temperature of the test for as long as possible. This process is known as a thermal soak. The intention is to ensure that the specimen has reached a thermal equilibrium and to ensure that there is no moisture in the laminate. The release of moisture while warming up the laminate causes a surface strain response that is not fully related to the CTE. Figure 20 shows the thermal soak for the Set A holes of the $[0_2/90_2]_s$ specimen. Each individual strain reading is not interesting by itself, but together with all the strain readings, some interesting patterns emerge. The thermal soak for the holes drilled to an odd depth produced similar results, so only the results for the holes drilled to an even depth are shown.

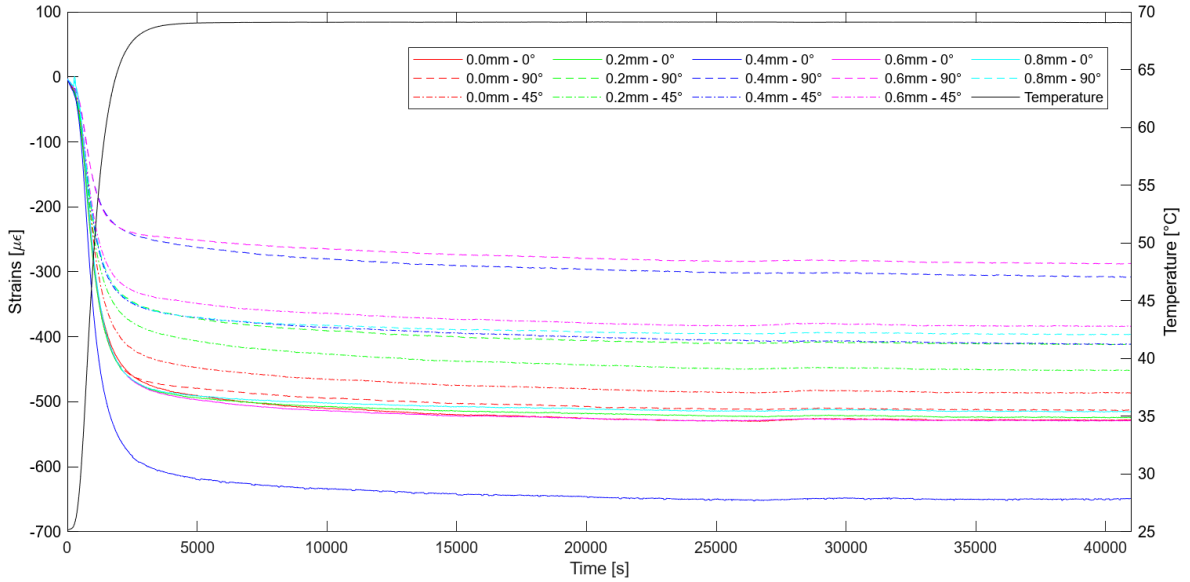

Figure 20: Strain response of the $[0_2/90_2]_s$ specimen during the thermal soak

For ease of interpretation, the measured temperature has been plotted on a secondary axis. After turning the light bulbs on, the temperature of the specimen rises quickly from room temperature (about 25°C) to the maximum temperature (just over 69°C). The temperature reaches the target set point and stabilises at roughly 10000 seconds. The same does not happen with the strains. The recorded strains continue to change slowly until around 32500 seconds as moisture is driven from the laminate. Thereafter, the strain values for all traces do not vary by more than 2 $\mu\epsilon$, and the distance between each line stays the same. This indicates that even if there is a small drift in strains, all the strain gauges are drifting equally. The drift is accounted for when the reference strain value is subtracted from the active gauge readings.

5.2.2 Hole Set A

The raw surface strain data recorded during the cooling of the $[0_2/90_2]_s$ specimen was normalised to identify any issues with the data. The strains traces were normalised by dividing each recorded value by the maximum strain measured by each strain gauge, making the largest possible value 1. Given that all the strain gauges are experiencing the same change in temperature, their strain profiles should be similar once normalised. Any traces that deviate from the others can be easily identified and the root cause investigated.

The normalised data obtained for this case is shown in Figure 21. As with Figure 20, temperature has been added to provide context.

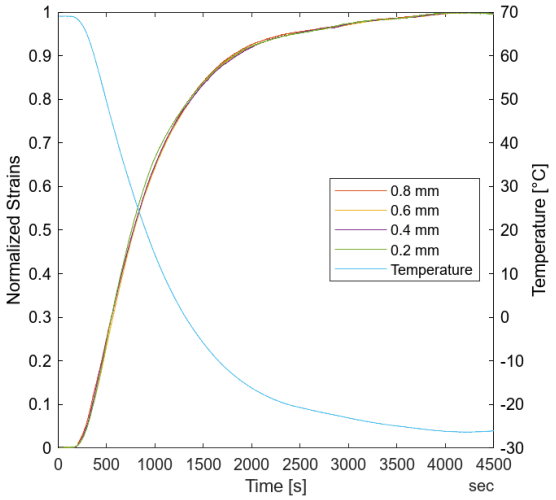

(a) 0˚ direction

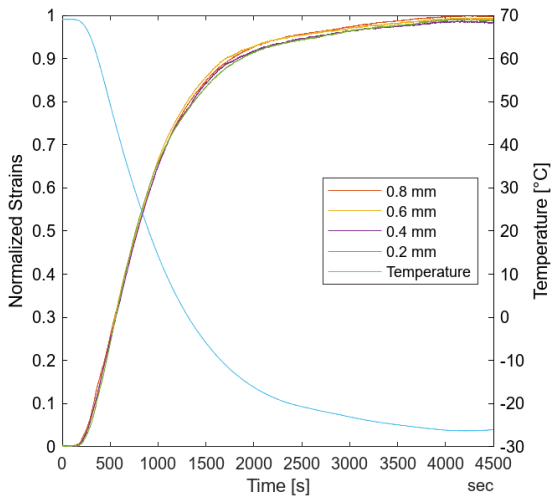

(b) 90˚ direction

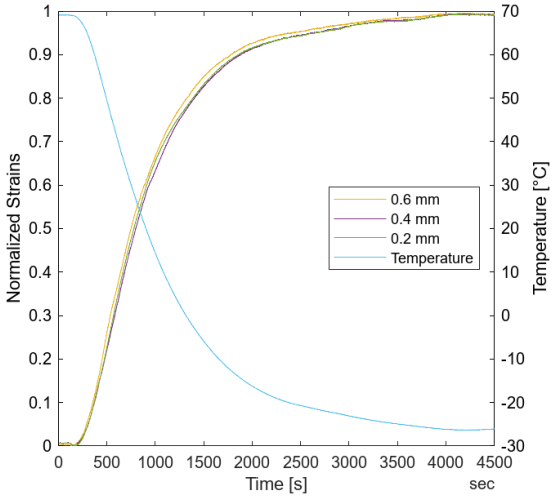

(c) 45˚ direction

Figure 21: $[0_2/90_2]_s$ normalised strains in relation to time for even depth holes

The normalised strain data from Set A has been limited to 4500 seconds. At this point, the temperature in the DCCTE reached a turning point and the temperature started to slowly increase as a consequence of the dry ice being consumed. The increase in temperature was slow, but at 4500 seconds the minimum temperature had been reached, and the strain readings had

stabilised.

As noted in the thermal soak test, the measured strains increase as the temperature decreases, but with a slight lag. A sharp increase in temperature results in a sharp decrease in strain. This is to be expected as there is a linear relationship between temperature and the thermal expansion of a test specimen. A difference between the thermal soak results and the results displayed in Figure 21 is that the strain release profiles are more uniform. Although the thermal soak results are not normalised, it can be seen that the strain readings stabilise at different times. The difference in time taken between the stabilising of the temperature and the strains is larger in the thermal soak than in the results displayed in Figure 21. A small difference between the time taken for the strains and the temperature to stabilise is still expected as the inner volume of the laminate will take some time equalise with the surface temperature. The small difference between the time taken for the strains and the temperature to stabilise, and the small difference in transient strain profiles confirm that moisture was removed by the thermal soak and does not affect surface strain readings.

The normalized strains shown in Figure 21 allow the comparison to be made between the strains in a particular direction at each hole depth. It is imperative that results be grouped into strains measured in the same direction as the strain response profile may differ between each direction. Figure 21a depicts the normalized change in strain over time in the 0° direction, where the behaviour of all the strain gauges is very similar, the largest difference being about 3%.

Figure 21b shows the normalized change in strain in the 90° direction over time. As with the normalised strains in the 0° direction, the strain profile between all the gauges are very similar. It follows the inverse of the temperature curve, although a small discrepancy exists after about 1500 seconds where there is a slight variation in the strain profiles. This difference is, however, no more than 5%.

Finally in Figure 21c, the change in strain over time in the 45° direction is shown. No data is recorded for the 0.8 mm deep hole due to the damaged strain gauge. The normalised strains profile in the 45° is similar to that seen in the 90° direction . The only strain profile that deviates from the others is that of the 0.6 mm deep hole. The difference is 3% at most, so it is not a significant difference.

5.2.3 Hole Set B

Similar tests were performed measuring the surface strains at hole Set B of the $[0_2/90_2]_s$ specimen. The normalised results are displayed in Figure 22

The normalised strain data from Set B has been limited to 6000 seconds. As with hole Set A, additional data was recorded, but by 6000 seconds the temperature reached a localised minimum and the strains reached a localised maximum.

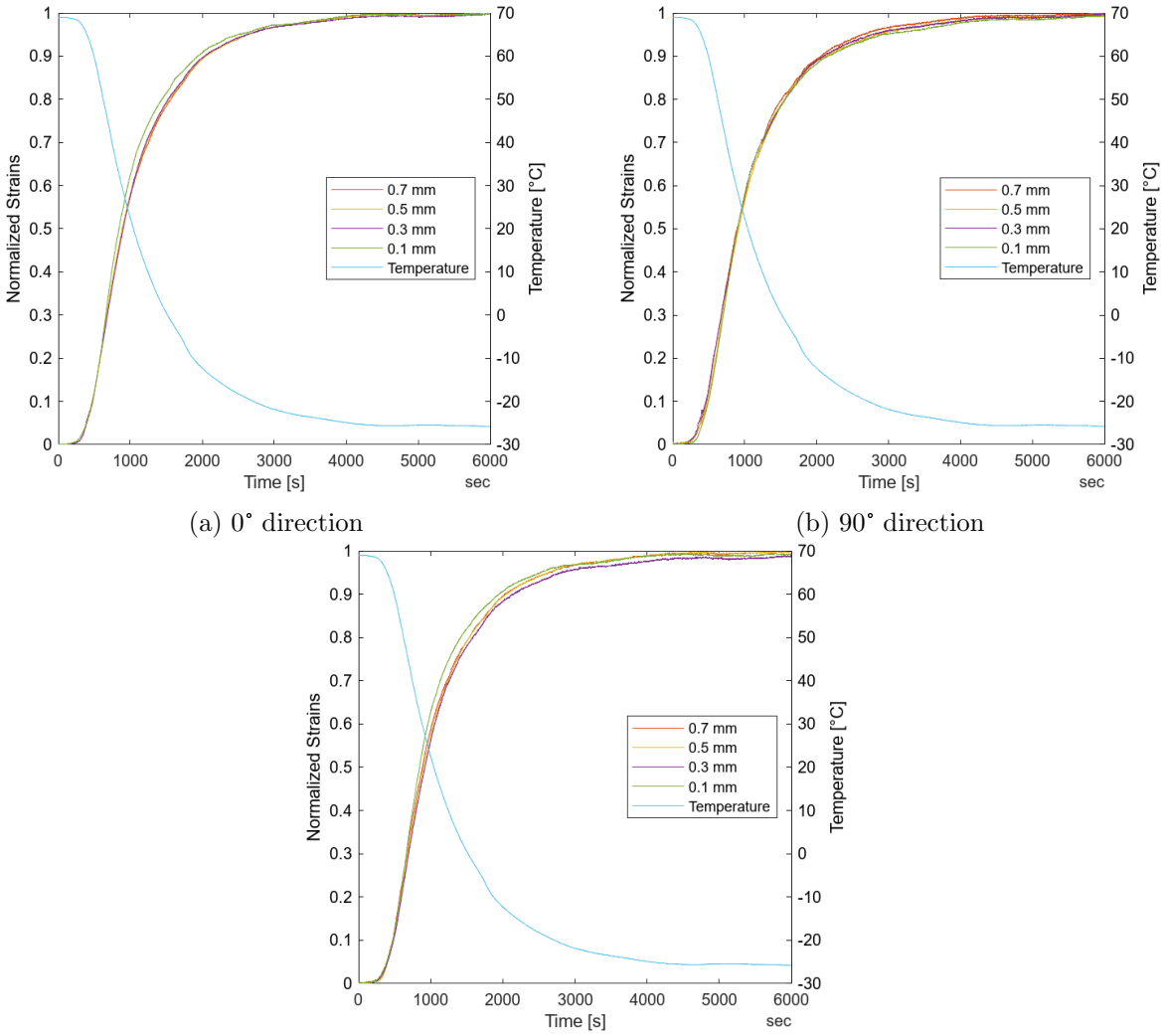

(a) 0° direction

(b) 90° direction

(c) 45° direction

Figure 22: $[0_2/90_2]_s$ normalized strains in relation to time for odd depth holes

The trend observed in all the subplots of Figure 22 are consistent with those of Figure 21 in that the measured strains increase as the temperature decreases. The temperature drops to approximately the same minimum as the Set A tests, but does so a little slower. The strains equalise at about the same timestamp as the temperature. Both sets of graphs are also comparable in how close the strain profiles are in corresponding strain directions. The 0° and 45° strain profiles vary by no more than 5%, and the 90° profiles are a little less scattered and differ by no more than 2%. This trend is similar to that seen in Set A.

5.2.4 Stabilisation of End Point

The validity of the measured strains in the context of this investigation is dependent on the test specimen being at thermal equilibrium at the beginning and end of the test. To ensure that this was achieved, the normalised strains in the final 10 minutes of measurement were examined. The results are shown graphically in Figure 23.

Figures 23a, c, and e show the variation in strain in the 0°, 90°, and 45° directions respectively in the 10 minutes prior to the final reading being taken in Set A. In this test, the total temperature range is 0.5°C. As the total range of the test is approximately 95°C, this represents a temperature change of 0.5% in the last 10 minutes. The strains deviate a maximum of 0.2% in the 0° direction, 0.3% in the 90° direction, and 0.3% in the 45° direction. Even taking the small spike in the 45° direction at the 0.2 mm and 0.4 mm deep holes into account, the strains measured in all directions remained relatively constant during this 10 minute period.

Figures 23b, d, and f show the same data, but for the testing of Set B. The 10 minutes prior to the final measurement being taken exhibit a smaller range in temperature, closer to 0.1°C, with a spike between 5100 and 5300 seconds. A change in temperature of this magnitude is not seen as something that could affect the strain readings a lot. The strains do seem to drift a little, no more than 2%, but on the whole, the strains in the same direction drift at the same rate, indicating that a relative strain comparison with reliable results is possible. The strains in the 0°, 90°, and 45° directions vary by a maximum of 0.2%, 0.4%, and 0.2% respectively over the measured time.

In summary, the relative stability and consistency of all the subplots in Figure 23 allow for the results obtained for this test to be meaningful overall, even if there are localised discrepancies.

5.3 Computation

MSC Patran/Nastran FE analysis was used to compute the expected strains. Due to symmetry of the material and the ideal hole, modelling the $[0_2/90_2]_s$ specimen only required an adequately constrained quarter model. A quarter of a disk with a diameter of 18 mm and a thickness of 1.6 mm is modelled. At the location where the centre of the disk would be, a separate region representing a hole of 2 mm diameter was created. This is the region where the elements were deleted layer by layer to achieve the desired hole depth. The initial geometry, along with a visual representation of how the quarter model was constrained is shown in Figure 24. Figure 24b in particular shows the location of the hole and the strain gauges.

The model consisted of 56192 HEX8 3D elements. These are solid elements with 8 nodes. The element size varied radially, with the elements closer to the centre smaller than the elements further away. This allows for a detailed analysis around the hole and the location of the strain gauges, the main areas of interest, without becoming overly computationally expensive. Each ply is described by 4 elements through the thickness, making the total laminate 32 elements thick. All elements have uniform thickness. The determination of the sizing of the surface mesh was made in conjunction with that of the through thickness mesh to ensure that an aspect ratio close to 1 is maintained in the regions of interest.

The MAT9 material card was used as it can describe an anisotropic material and allows for

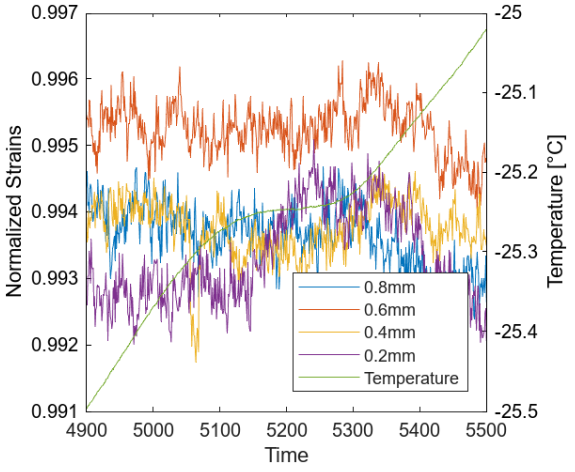

(a) 0° direction - Set A

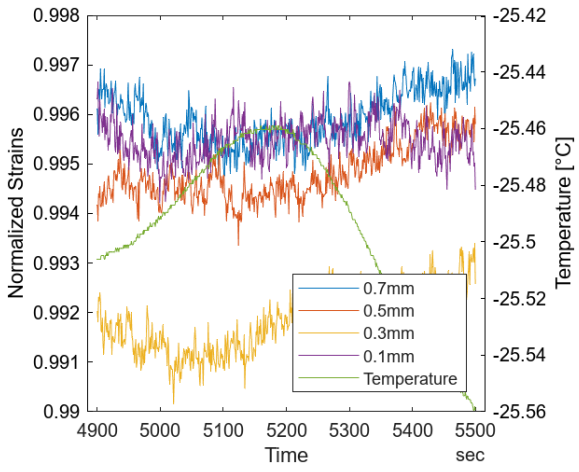

(b) 0° direction - Set B

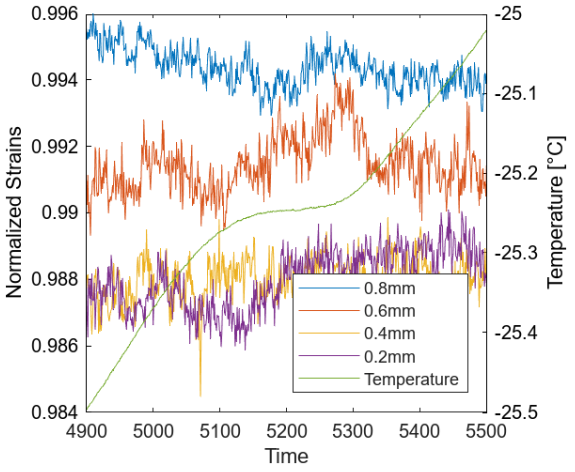

(c) 90° direction - Set A

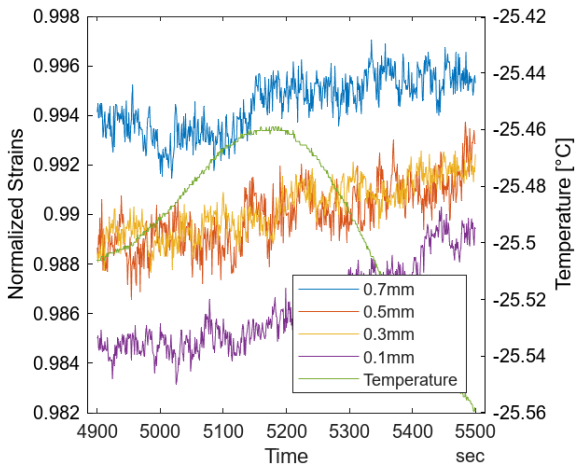

(d) 90° direction - Set B

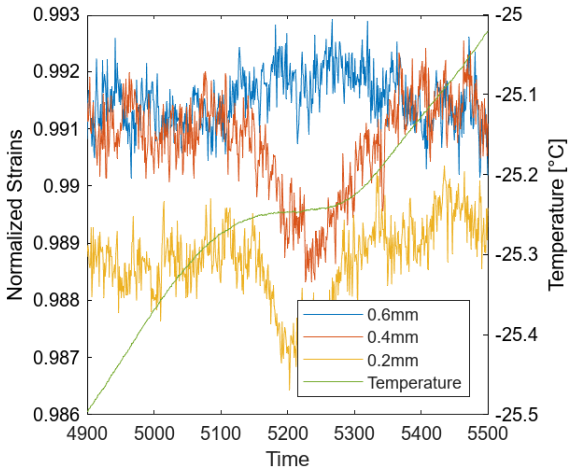

(e) 45° direction - Set A

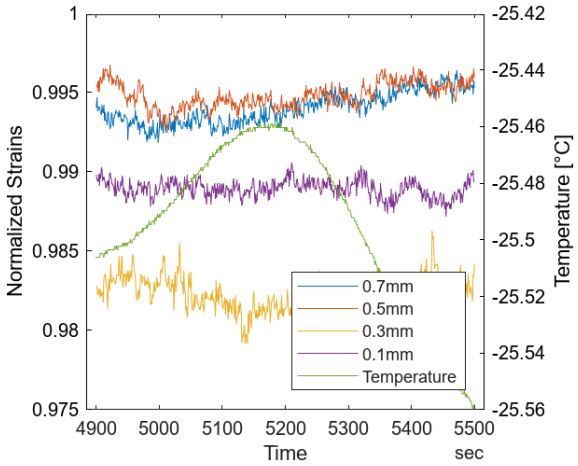

(f) 45° direction - Set B

Figure 23: $[0_2/90_2]_s$ normalised strains over time for the last 10 minutes of recording

input of CTEs and reference temperature. Three coordinate systems were created with their x-axis rotated by 45°, -45° and 90° clockwise respectively. Along with the original global axis, these axes were used to align the single defined material for each ply in the correct direction, eliminating the need to define a different material for each differently oriented unidirectional ply. It is also easier to change the properties of one material than to change those of four, which

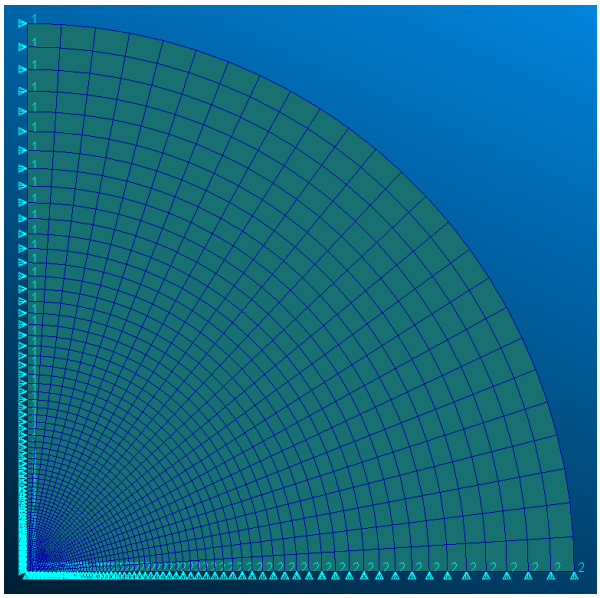

(a) Top view with x and y constraints

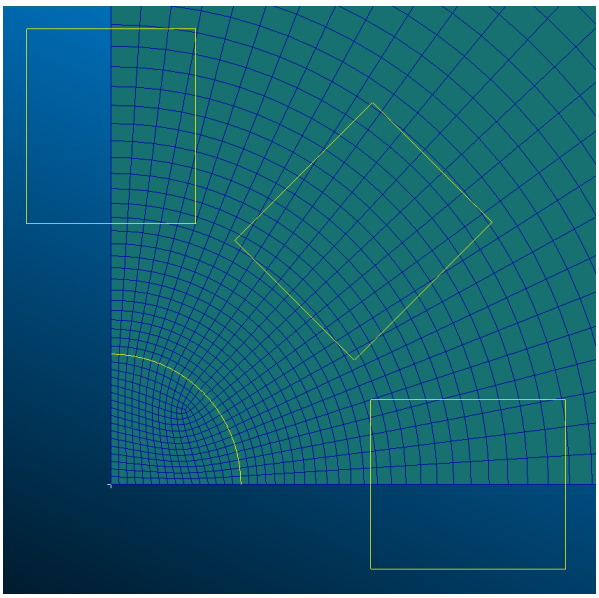

(b) Top view with hole and strain gauge locations

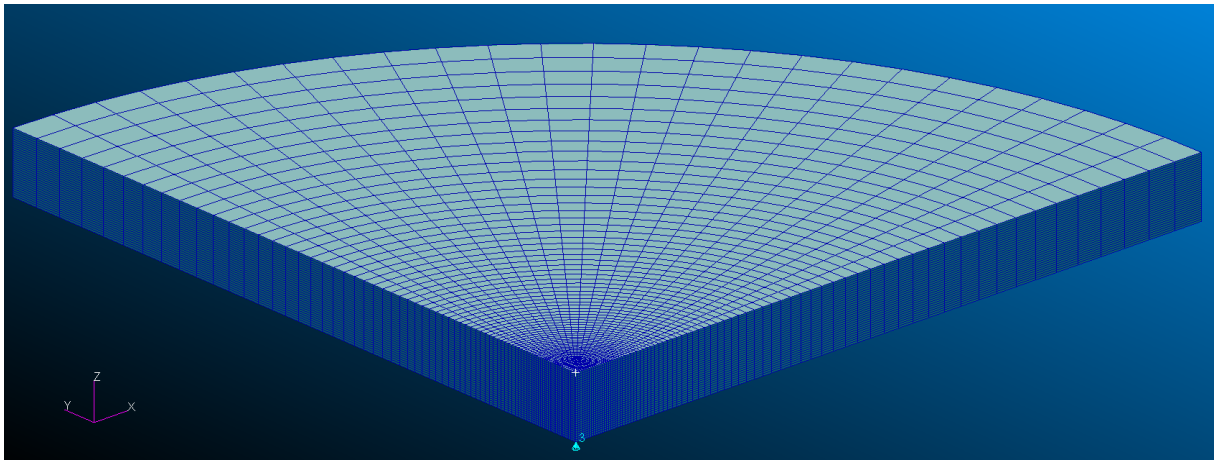

(c) Isometric view with z constraint

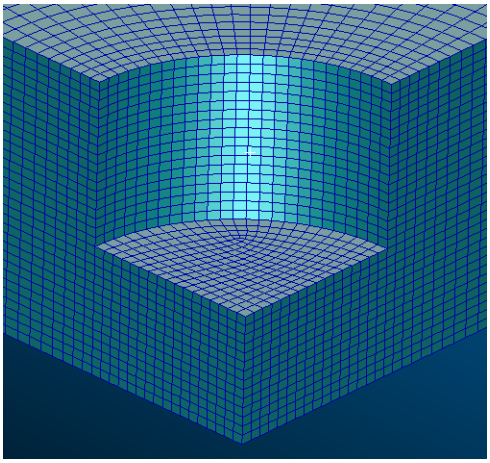

(d) Mesh constructed for the $[0_2/90_2]_s$ specimen with a hole

Figure 24: Mesh constructed for the $[0_2/90_2]_s$ specimen

makes the direct modification of Nastran BDF files easier for a Monte Carlo uncertainty analysis which will be discussed in Section 5.4.2.

A temperature of 100°C was applied as a nodal temperature load. The models were analysed using the SOL101 solver which is appropriate for static, linear cases. Since the transient response of the model is not required, nor is it expected to exceed the elastic limit, the SOL101 solver is adequate for this model.

For each hole depth required, the appropriate number of layers of elements are deleted from the hole region. Each 0.1 mm corresponds to 2 layers of elements. Starting at 0.1 mm deep, models are made and run for hole depth increments of 0.1 mm until a depth of 0.9 mm is reached. A zoomed in example of a model with a hole of 0.9 mm depth is shown in Figure 24d.

The $[0/90/+45/\text{-}45]_s$ model was similarly constructed. The only difference was that the presence of 45° plies means that a full model was necessary. The model previously detailed was mirrored across the y-axis and then the new solid was mirrored about the x-axis to produce a full disk. Boundary conditions were applied to prevent rigid body motion without introducing additional constraint loads. These boundary conditions were applied to the undrilled side and are visually depicted in Figure 25, where the blue dot denotes the node constrained, and the text denotes its applied constraints.Using the previously mentioned coordinate systems, the material properties were assigned. The rest of the process is similar to that described for the $[0_2/90_2]_s$ laminate.

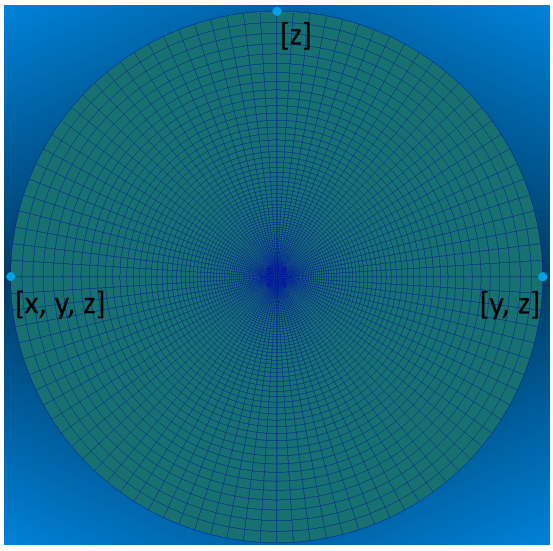

Figure 25: Model constraints applicable for the $[0/90/+45/-45]_s$ laminate

Once run, the displacement data from the FE model is processed to obtain the required strain data at the strain gauge locations. The surface stress distribution within the strain gauge grid area may not be uniform, yet the strain gauge only measures a single strain value [61]. Therefore, multiple points around the perimeter of the strain gauge grid are requited to compute the strain reading that would be recorded [61]. A surface spline is fitted through the displacements in the x direction, and another through the displacements in the y direction. The surface splines make it possible to obtain the strain data at any point in the model, not only at the node locations. Ten equidistant points representing the inner and outer edges of the strain gauge grid are defined. The displacements in the x and y direction were found for each of these points on the strain gauge, then the points relating to each side of the strain gauge grid were averaged.

Obtaining the strains from the displacements requires some calculation. Figure 26 is a schematic of a strain gauge pre-deformation (denoted in black), and post-deformation (denoted in red). Both the left and the right edge of the strain gauge translate, but by different amounts; ΔX_1 and ΔX_2 respectively. Therefore, if the original length of the strain gauge was L, then the new length after deformation is $L + \Delta X_2 - \Delta X_1$.

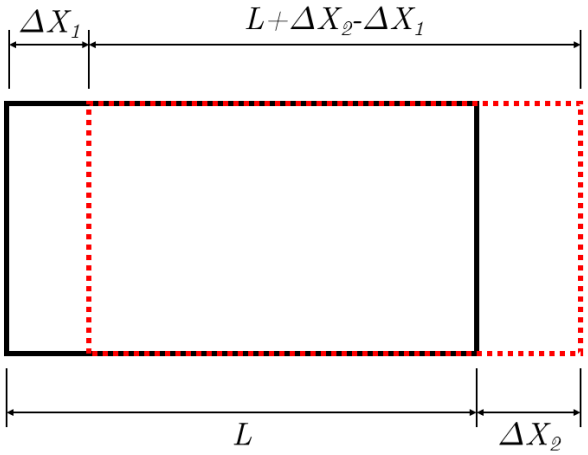

Figure 26: Obtaining strains from deflections of two points

Knowing the equation for strain, one can substitute accordingly:

$$\begin{aligned} \epsilon_X &= \frac{\Delta L}{L} \\ &= \frac{(L + \Delta X_2 - \Delta X_1) - L}{L} \\ &= \frac{\Delta X_2 - \Delta X_1}{L} \end{aligned} \tag{13}$$

Therefore only the displacement values for each side of the strain gauge and the original strain gauge length are needed to calculate the strain. Calculating the strains in the 45° strain gauge requires an extra step. The displacements in the x and y directions were rotated through 45° using trigonometry to determine the displacements aligned parallel and transverse to the grid direction.

A MATLAB script that automates the extraction of the strains from the FE output was developed to automate the process as this procedure was to be done on all FE models.

5.4 Consolidation between FE and Experimental Data

The data obtained from the FE model and the physical experimentation are not directly comparable. FE models a perfectly centred 2 mm diameter hole to perfect depth increments of 0.1 mm with a perfectly flat bottom. Experimentally the holes will usually have a slightly different diameter and include minor misalignment. The inverted cone end mill also does not produce a perfectly flat hole bottom. The determination of the zero depth position is particularly difficult with non-conductive materials such as GFRPs. When drilling metals, the Sint Technology

Restan MTS 3000 can be made to stop drilling as soon as it touches the sample by closing an electrical circuit made with the sample. This is not the case with FRP materials and one needs to determine the zero position visually while monitoring the strain response as the end mill is advanced slowly towards the sample's surface.

The use of dry ice yields inconsistent minimum temperatures from run to run. One full set of results requires two runs: one for hole Set A, and another for hole Set B. Furthermore, some of the material properties have rather large uncertainties associated with them. All of these factors may cause the FE model to differ from the physically measured results. Some of these factors may have large influences, others might be insignificant. Regardless, there are some parameters that can be accounted for and for those that cannot, a Monte Carlo simulation was used to ascertain what the uncertainty is.

5.4.1 Correcting Discrepancies

The first discrepancy addressed was the difference in temperature between FE and experimentation. Since the exact change in temperature is not guaranteed between test runs, the choice was made to present the results at a change in temperature of 100°C. This value is not far off from what was measured in the physical test, and is a round number to present the data. Since the effects of temperature on strain are linear, it is possible to scale the results accordingly. The physical tests were scaled to 100°C to match FE.

Another substantial discrepancy was the misalignment of the drilled hole. Over time, the cross-hairs of the microscope on the Sint Technology Restan MTS 3000 start to deviate from perfect alignment. Perfectly positioned cross-hairs may still result in an offset hole. An example of a misaligned hole can be seen in Figure 27a.

FE results for an offset hole were found to compensate for misalignment. This was done by offsetting the strain gauge rosette location with respect to the drilled hole in the MATLAB script. A visual representation of the process is shown in Figure 27b, with the rectangles denoted by dotted lines representing the strain gauge location before the correction. The rectangles with solid lines indicate the new position of the strain gauges after the correction. Once the post-correction strains are obtained, their percentage deviation from the pre-correction strains are calculated. It is assumed that the measured strains will react in the same way, so the inverse of this percentage difference is applied to the measured strains. The final output surface strains represent a hole that has been corrected for offset to represent what the strains would be had the hole been drilled correctly.

Correction for the actual hole diameter is required as it was decided that the modelled hole will be one measuring 2 mm in diameter. To correct for incorrect hole diameter three different FE models were required. One for the ideal diameter, one smaller (1.85 mm), and one larger (2.15 mm). The FE models were constructed in exactly the same way as the original model.

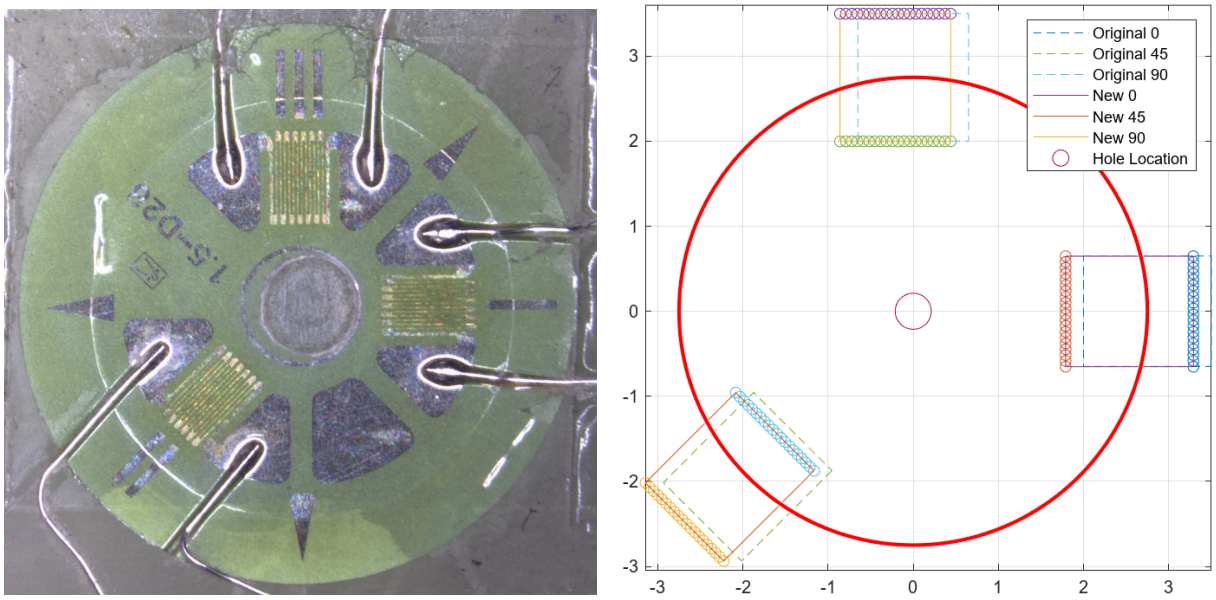

(a) Misaligned strain gauge rosette

(b) Offset correction

Figure 27: Strain gauge misalignment and correction

Surface strains for each of these models were obtained at all relevant hole depths. A quadratic equation was then fitted through the FE results for the different hole diameters at each hole depth. This allowed the FE surface strains for all hole diameters to be interpolated without having to model every single hole. The FE surface strains for each measured hole diameter were found and a percentage difference from the ideal hole (2 mm diameter) was calculated. It was assumed that the physical surface strains would behave the same way, so the inverse of the percentage difference was applied to the originally measured surface strains, thus correcting the strains for inconsistent hole diameter.

5.4.2 Uncertainties

As with any investigation, uncertainties are unavoidable. It is important to quantify them so that the data can be meaningful. There are uncertainties that relate to both the FE and the physically measured results. Both of these need to be taken into account.

5.4.2.1 Uncertainties in Experimental Results

One standard deviation of uncertainty in any recorded instrument can be approximated as the square root of the summation of the square of all uncertainties involved in its measurement. This is known as the law of propagation of uncertainty as defined in JCGM 100:2008 [62]. These uncertainties are directly related to the strain gauges and DAQ system they are connected to. It was found that the HBM QuantumX MX1615B DAQ has an uncertainty of 2% of the measured strains. The strain gauge uncertainty was found to be 1 $\mu\epsilon$ by leaving the DAQ recording for 10

minutes without a load being applied and calculating the standard deviation over that period.

To better represent all the captured and calculated data, two standard deviations were used for the uncertainty calculation. This statistically corresponds to 95% of the data spread. The mathematical representation of the uncertainty calculation is shown in Equation 14 where $\Delta\epsilon$ is the strain reading uncertainty to two standard deviations, and ϵ_{raw} is the measured strain before correcting to the reference. It is important to note that this uncertainty is related to the measured change in temperature, not the idealised change in temperature of 100°C. The same temperature scaling is applied to the uncertainty as is to the strain reading described in Section 5.4.1.

$$\Delta\epsilon = 2 \cdot \sqrt{(2\% \cdot \epsilon_{raw})^2 + (1\mu\epsilon)^2} \tag{14}$$

5.4.2.2 Uncertainties in FE Results

The uncertainties related to the FE model present a slightly bigger challenge to compute. As with all software, FE suites operate on the 'garbage in, garbage out' principle. As such, it is important to ensure that the model is set up correctly and that the input material properties are correct. Even so, there is an uncertainty in the measured material properties. The orthotropic nature of each GFRP lamina and the various orientations makes it close to impossible to predict how a change in lamina properties will affect the surface strains of the laminate. To overcome this challenge, a procedure known as a Monte Carlo simulation [63] can be used in conjunction with FE to obtain the combined uncertainties related to the complete model.

A Monte Carlo simulation is a process whereby approximate deterministic answers are obtained using statistical probability [64]. The method is particularly useful when the interaction between many variables is difficult to predict or too computationally intensive. When using this method, two things are needed from each variable: the mean and the probability distribution. The Monte Carlo method makes use of a large number of trials. For each trial, a pseudorandom value that falls within the selected probability distribution for each variable is generated. The generated values are then used to compute the final solution. As the number of tests increases, the mean starts becoming apparent. After a sufficiently large number of tests, the mean and standard deviation of all the data converges. The mean becomes the plotted point, and the standard deviation becomes the uncertainty. The Monte Carlo simulation method was used in three ways in this investigation. It was used to find the uncertainty in the lamina CTEs, to find the uncertainty in the FE model due to the uncertainty in the material properties, and to shift the uncertainties to the non-reference strain gauge rosettes when investigating the use of drilled rosettes as surface strain references.

The computational determination of the lamina CTEs was complicated by the unknown material properties of the matrix and fibres that make up the lamina. Mathematical relationships as

expressed in equations 15 and 16, both from the work of Schapery [65], relate material properties to the lamina CTEs, but the precise properties of the constituent materials used in this work are not known. The material property variables used in equations 15 and 16 are defined in Table 4.

$$\alpha_1 = \frac{E_f \alpha_f V_f + E_m \alpha_m V_m}{E_f V_f + E_m V_m} \tag{15}$$

$$\alpha_2 = (1 + \nu_f)\, \alpha_f V_f + (1 + \nu_m)\, \alpha_m V_m - \alpha_1 \left(\nu_f V_f + \nu_m V_m\right) \tag{16}$$

The CTEs were measured by experimentation, but the uncertainty was found by Monte Carlo simulation. Fibre and matrix properties were taken from data listed by Herakovich [66]. Although uncertainties were not stated by Herakovich, small uncertainties were used for properties relating to the fibre, and large uncertainties were used for the properties related to the matrix. The E-glass used in the prepreg falls within a defined specification, whereas the matrix is proprietary and its properties can vary a lot depending on the manufacturer. The properties used in the Monte Carlo simulation are listed in Table 4.

By 5×10^5 iterations the results had converged. Although the CTEs found by equations 15 and 16 differed from the experimentally measured values, the prepreg uncertainties used allow for a comparison to be made between the calculated and measured CTEs. Therefore, the uncertainty for α_1 is taken to be 5.39% and that for α_2 is taken to be 15.07%. These values are reflected in Table 2.

Table 4: Inputs parameters used for Monte Carlo simulation to determine CTE uncertainties

x_i	Description	$p(x_i)$	Type	Features
V_f	Fibre Volume Fraction	Normal	B	0.6, 1.67%
E_f	Fibre Modulus	Normal	B	69×10^3 MPa, 3.0%
E_m	Matrix Modulus	Normal	B	3.4×10^3 MPa, 10.0%
α_f	Fibre CTE	Normal	B	5.4×10^{-6} /°C, 1.8%
α_m	Matrix CTE	Normal	B	63.0×10^{-6} /°C, 15.9%
ν_f	Fibre Poisson's Ratio	Normal	B	0.22, 10.0%
ν_m	Matrix Poisson's Ratio	Normal	B	0.35, 4.5%

The determination of the uncertainty within the FE results made use of the same model that was used to find the initial results, albeit with different material properties. E_1 was increased by 1% while the rest of the properties were kept at nominal values. Subsequently, E_2 was increased by 1% while the rest of the properties were kept at nominal values. The process was repeated until results had been obtained for a 1% change in E_1, E_2, G_{12}, ν_{12} and ν_{23}. The results show how the surface strains are affected by a 1% change in the material property in question. Of course, the uncertainty in each property was not 1% so the uncertainties for each property were scaled appropriately. The same raw materials and production processes as Smit and Reid [25] was used, therefore their material property uncertainties were used. The uncertainties found experimentally by Smit and Reid were around 2% for E_1, E_2, G_{12}, and ν_{12}. The value for ν_{23} was obtained by micromechanics estimates. The estimates may not be very precise, necessitating a large uncertainty of 5% to be used taken for ν_{23}. All material properties are taken to follow a

normal distribution. Using the data shown in Table 5, a Monte Carlo simulation with 5×10^5 iterations was run and the final FE uncertainties were calculated. These uncertainties varied per hole depth. The uncertainties along with the mean surface strains were used to generate an error band wherein the FE results should fall.

Table 5: Inputs parameters used for Monte Carlo simulation to determine strain uncertainties

x_i	Description	$p(x_i)$	Type	Features
E_1	Longitudinal Modulus	Normal	B	37841.3 MPa, 1.986%
E_2	Transverse Modulus	Normal	B	9912.85 MPa, 2.223%
G_{12}	Shear Modulus	Normal	B	3152.89 MPa, 2.582%
ν_{12}	Poisson's Ratio	Normal	B	0.3154, 2.078%
ν_{23}	Poisson's Ratio	Normal	B	0.4124, 5%
α_1	Longitudinal CTE	Normal	B	8.38×10^{-6} /°C, 5.39%
α_2	Transverse CTE	Normal	B	43.17×10^{-6} /°C, 15.07%

6 Results and discussion

To coherently discuss the results, they are broken down into three main sections: Experimental results, FE results, and comparison between the two. Two laminate configurations, $[0_2/90_2]_s$ and $[0/90/+45/\text{-}45]_s$, were used for this investigation and the same kind of data was obtained for each.

6.1 $[0_2/90_2]_s$ Laminate

6.1.1 Experimental results

The strains measured during testing were recorded and, as usual with IHD, all strains are referenced to those measured by the undrilled rosette. Figures 28 and 29 show the raw stains measured in Set A and Set B respectively as referenced to the undrilled rosette. The measurement uncertainties comprising the measurement noise and the strain gauge uncertainties are shown as error bars.

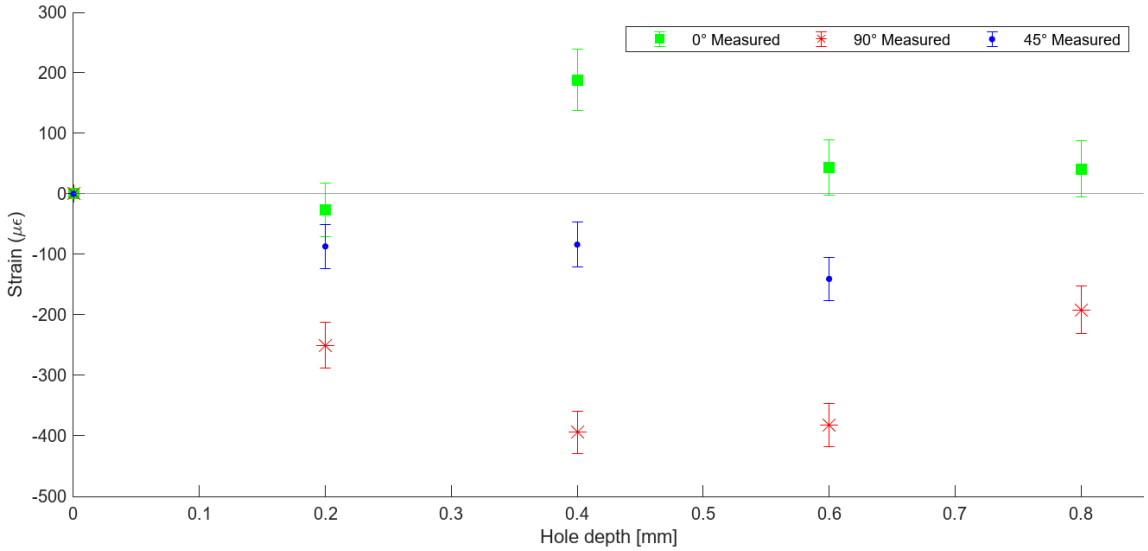

Figure 28: $[0_2/90_2]_s$ - Strains measured at holes of differing depths in Set A with respect to the undrilled rosette, ΔT = -93.48°C

Set A (the experimental strains of which are shown in Figure 28) consists of the strains measured in the 0°, 45°, and 90° direction relative to the laminate coordinate system at the undrilled rosette and holes drilled to depths of 0.2 mm, 0.4 mm, and 0.6 mm. During the investigation, the solder tabs on the rosette used for the strains in the 45° direction of the 0.8 mm deep hole were irreparably dislodged, therefore only the strains measured in the 0° and 90° directions are included in the dataset. Set B (the experimental strains of which are shown in Figure 29)

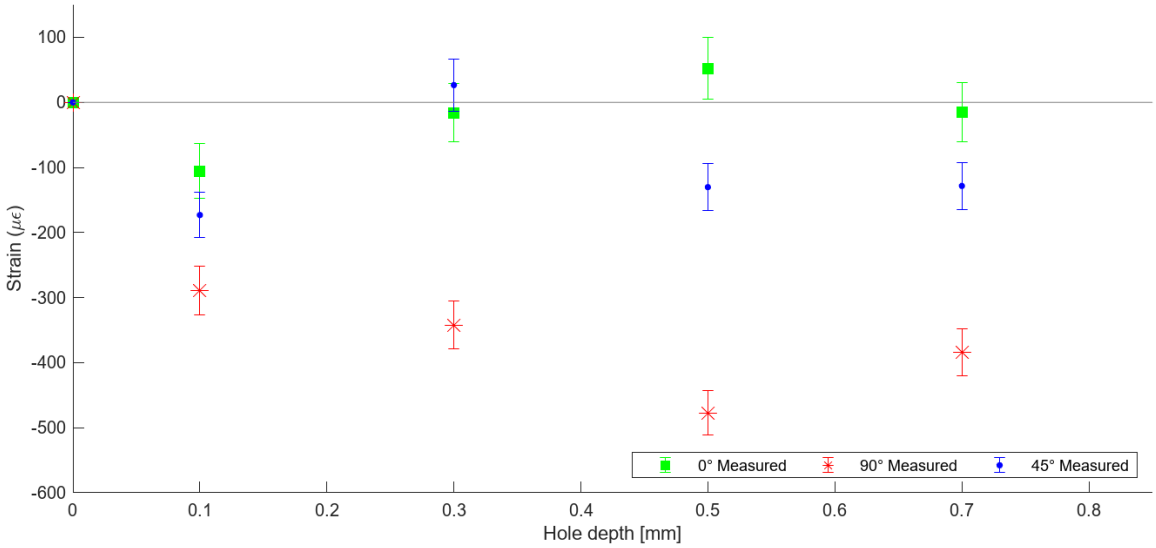

Figure 29: $[0_2/90_2]_s$ - Strains measured at holes of differing depths in Set B with respect to the undrilled rosette, ΔT = -94.71°C

consists of the strains measured in the same direction as in Set A, but for holes drilled to depths of 0.1 mm, 0.3 mm, 0.5 mm, and 0.7 mm. Since the tests for Set A and Set B were run independently, and the cooling process was not actively controlled, the change in temperature was similar, but not identical for each hole set. Temperature changes of -93.48°C and -94.71°C were measured during the thermal testing of Set A and Set B respectively.

Individually, hole sets A and B provide a coarse description of the change in surface strains as the hole depth increase, but together a finer description is obtained. The experimental results for holes sets A and B, not yet corrected for hole diameter and hole location, have been aggregated onto Figure 30. The strains measured in Set B and their respective uncertainties were linearly scaled to reflect the change in temperature in Set A, providing a comparison that is like to like.

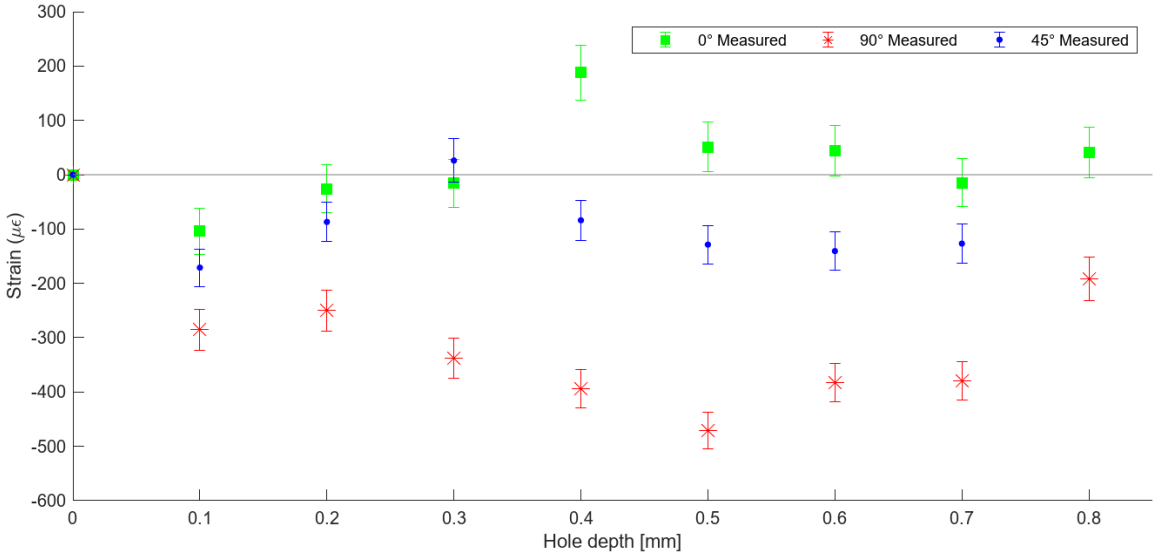

Figure 30: $[0_2/90_2]_s$ - Combined uncorrected measured strains with respect to the undrilled rosette, ΔT = -93.48°C

In Figure 30 the trends in the change of surface strains measured in each direction can be seen to a finer degree. Nobre et al. [24] found that, particularly under small applied loads, a change in gradient can be seen at the interface between lamina of differing properties. A similar trend was noticed in the data presented by Smit and Reid [25]. This trend is replicated in the experimental data obtained. The strains measured in the 0° and 90° directions each show one major turning point; at 0.4 mm and 0.5 mm respectively. The strains in the 0° direction steadily increase to their turning point at a strain of 188.2 $\mu\epsilon$, after which they decrease. In the 90° direction, an opposite trend is found. The measured strains steadily decrease, reaching a minimum of -471.1 $\mu\epsilon$. Thereafter, the strains increase slowly. In both cases this turning point is close to the region where a change in fibre direction occurs, at a nominal depth of 0.4 mm.

The trend in strain measured in the 45° direction is more difficult to determine. There is a local minimum of -171.0 $\mu\epsilon$ and a local maximum of 26.2 $\mu\epsilon$ at hole depths 0.1 mm and 0.3 mm respectively. Other than those depths, the strains measured in the 45° direction have a mean of -113.4 $\mu\epsilon$, deviating by an absolute maximum of 29.6 $\mu\epsilon$. At the scale of the strains measured in the 0° and 90° directions, such a low deviation can be taken to represent a constant value.

A concern presented by the data shown in Figure 30 is the mismatch between the strains measured at the undrilled strain gauge rosette and those measured at all the other hole depths. Generally, a large change in gradient as the hole depth increases is related to a change in material properties, but this is not the case with the strain measured in the region corresponding to a hole depth of between 0.0 mm and 0.3 mm. Here, a local turning point is present, but the material properties do not change. The strains measured elsewhere follow the expected trend. A reference strain gauge rosette that gives faulty readings can cause the whole dataset to be shifted in the y direction on Figure 30. It is possible that the strains measured at the reference strain gauge rosette are indeed faulty, and as such a different reference rosette may need to be used.

6.1.2 FE Results

The FE prediction for the strains in the 0°, 45° and 90° directions for the $[0_2/90_2]_s$ laminate were found using models representing 2.0 mm diameter holes of different depths. A temperature change of 100°C was applied to the models. 100°C was chosen as it allows for easy scaling of the strains. The resulting strains are shown in Figure 31 with the undrilled state as the reference. The uncertainty bands were found by Monte Carlo trials as explained in Section 5.4.2 and are denoted in dotted lines to two standard deviations to include 95% of the possible variation.

The surface strains predicted by the FE models show a single turning point in both the 0° and 90° directions. These points are at found at depths of 0.4 mm and between 0.4 and 0.5 mm for the 0° and 90° directions respectively. Both sets of strain data grow from 0 to their absolute maxima and then decrease, roughly mirroring each other. The strains predicted in the 45° direction do not change much, but they do increase, changing gradient at a depth of 0.4 mm.

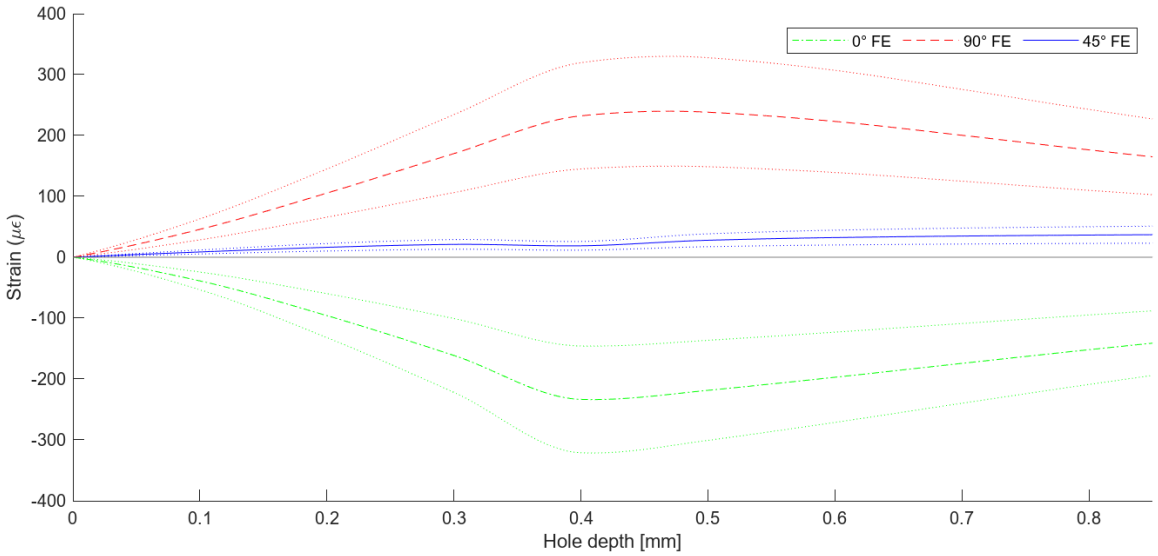

Figure 31: $[0_2/90_2]_s$ - FE model with undrilled state as the reference datum, ΔT = 100°C

The uncertainties for the strains in all directions increase as the predicted value gets further away from 0 $\mu\epsilon$, but decrease after the turning points as the strains tend towards 0 $\mu\epsilon$.

Figure 31 indirectly shows that some of the experimental strain measurements within the 0.0 mm to 0.3 mm are most likely incorrect. There should not be a big difference between the strains measured at 0.0 mm and 0.1 mm. To mitigate against the effects of an erroneous strain gauge, a strain gauge rosette associated with a different hole depth should be used. In principle, any strain gauge rosette can be used as a reference rosette to isolate the effect of the hole depth from the applied thermal strain, but it is important to choose a rosette that has minimal uncertainty. The reference rosette is the standard to which all the other rosettes are measured. Any uncertainties attributed to the reference rosette will propagate to all rosettes that use it as the standard to measure against. The larger the uncertainty of the reference rosette, the larger the uncertainty of all measured strains.

Since sets A and B do not have holes in common, referencing both sets of strain readings to the same hole requires interpolation. The interpolation between two points is limited to being linear, therefore the hole depth chosen as the new strain reference must be within a region where the surface strains vary linearly. The trends in strain predicted by FE show that there are two regions of linearity, namely between depths of 0.0 mm to 0.4 mm, and 0.4 mm to 0.8 mm. Hole depths that cannot be used as reference rosettes are 0.0 mm, 0.1 mm, 0.4 mm, and 0.8 mm. 0.0 mm cannot be used as a reference because the strain values are suspected to be incorrect, and the rest of the depths cannot be used as they are found at extremities of their linear range.

The first rosette chosen as a reference will be that associated to the 0.2 mm deep hole.

6.1.3 Combination of Experimental and FE Strains

All strains referenced to the measured and predicted surface strains for a change in temperature of 100°C at a hole depth of 0.2 mm is shown in Figure 32. No corrections for hole diameter or hole location have yet been applied to the measured strains.

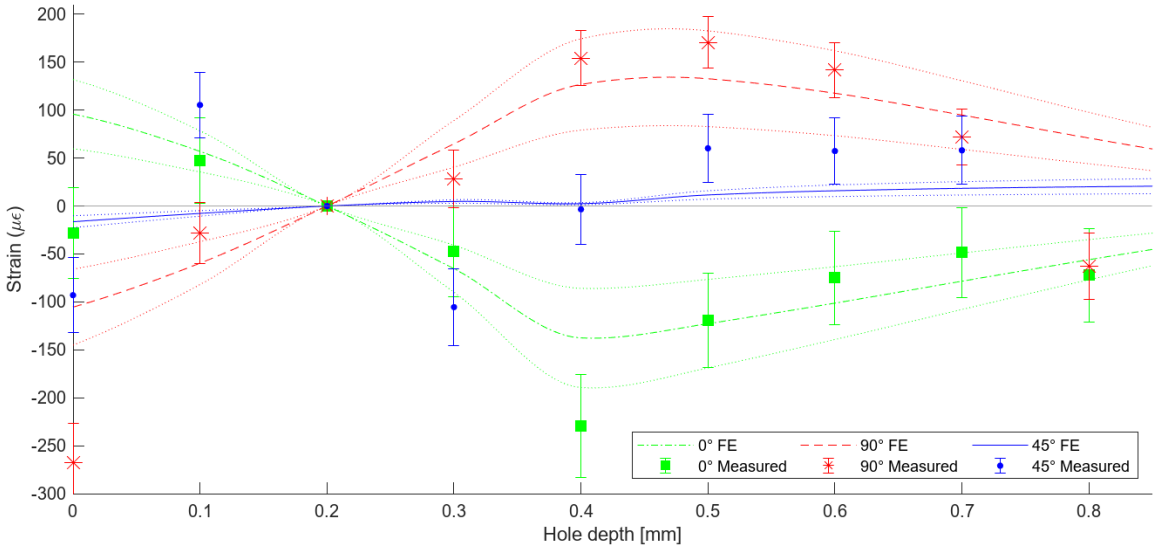

Figure 32: $[0_2/90_2]_s$ - FE and uncorrected measured strains referenced to the 0.2 mm deep hole, $\Delta T = 100°C$

Figure 32 shows some correlation between the measured strains and those predicted by FE. The trends in the results predicted by FE are the same as those shown in Figure 31, except for a shift in the y-axis so that the surface strains at a depth of 0.2 mm are 0 $\mu\epsilon$. The uncertainty related to FE also changes since the reference measurements are taken to have no uncertainty. The same trend of having a lower uncertainty closer to a surface strain reading of 0 $\mu\epsilon$ persists for all hole depths in all measured directions.

To align the experimental strain gauge readings to those predicted by FE, the measured strains and their uncertainties were linearly scaled to the temperature modelled in FE. The strains measured both in Set A and Set B were for a laminate put though a cooling process, where the FE was modelled for an increase in temperature. For this reason, the experimental strains have not only shifted in the y-axis as for the FE strains, but their gradients have flipped. Where in Figure 30 the experimental strains in the 0° direction increased to their maximum at a depth of 0.4 mm, the linear temperature scaling to +100°C causes the experimental strains to decrease until their minimum at the same depth. The same occurs with the 45° and 90° experimental results.

Figure 32 shows good overlap between the experimental and predicted surface strains. The overall trends seen in the experimentally obtained strains largely track those predicted by FE. The vast majority of the uncertainties in both the experimental strains and those predicted by FE overlap, particularly in the 0° and 90° directions. Some notable exceptions are all the strains measured at the undrilled rosette. The better fit of the experimentally obtained surface strains

when using a different strain gauge rosette reaffirms that the strains measured at the undrilled location are erroneous. Another notable exception is the strain measured in the 90° direction at the 0.8 mm deep hole. FE predicts the surface strains at a hole 0.8 mm deep to be 70.8 $\mu\epsilon$, but the measured strain is -62.6 $\mu\epsilon$.

The strains measured in the 45° direction deviate from the predicted strains more than those in the 0° and 90° direction. In addition to the strain measured at the undrilled rosette, the strains measured at a depth of 0.1 mm, 0.3 mm, and 0.5 mm do not overlap with those predicted by FE. As mentioned when discussing Figure 30, the strains measured in the 45° are smaller than those measured in the 0° and 90° direction, and are therefore more prone to imprecise readings and comparatively more affected by noise.

It is important to note that the reference hole selection affects the measured strains. The uncertainties in the strains measured at the reference hole propagate to all the others. Figure 33 shows the same strains as in Figure 32, but with all strains referenced to those measured and predicted at the 0.6 mm deep hole. A Monte Carlo simulation of 5×10^5 trials was used to shift the uncertainties from the 0.2 mm deep hole to the 0.6 mm deep hole.

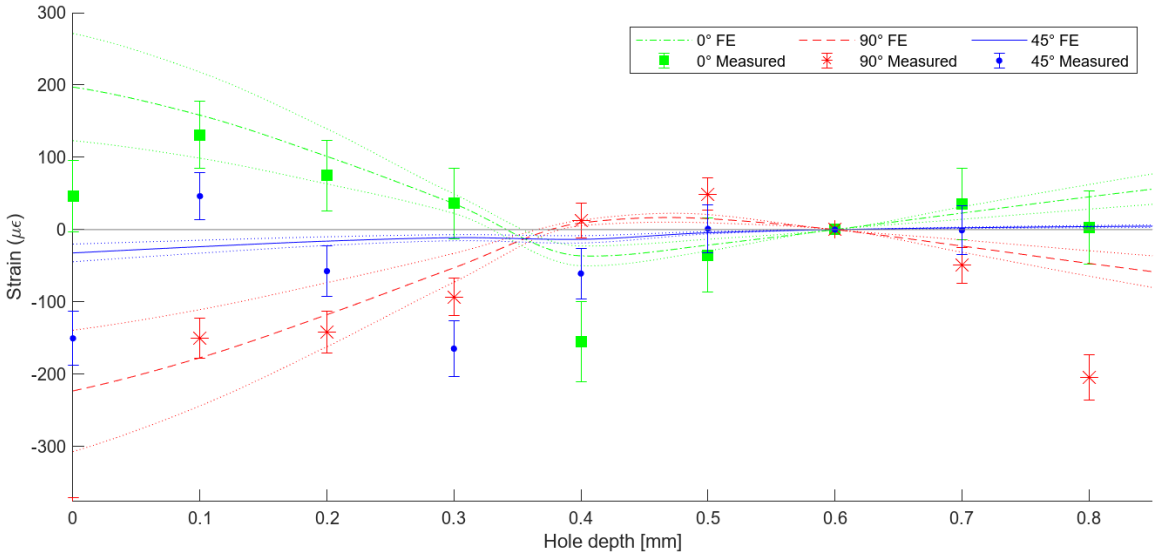

Figure 33: $[0_2/90_2]_s$ - FE and measured strains referenced to the 0.6 mm deep hole, $\Delta T = 100°C$

The agreement between experimental and FE surface strains in Figure 33 improves in some ways and deteriorates in others as compared to Figure 32. This is exacerbated by the change in the uncertainties, particularly relating to FE. The strains in the 0° direction mostly improve. All measured strains except those measured for a hole depth of 0.4 mm agree adequately with the strains predicted by FE. Although the uncertainties in surface strain do not overlap in the 0° direction at a depth of 0.4 mm when using 0.6 mm as a reference depth, the difference between the experimental and predicted value improves from 152.5 $\mu\epsilon$ to 118.6 $\mu\epsilon$ as compared to the use of 0.2 mm as the reference depth. A similar scenario occurs at the 0.5 mm deep hole, but in the 90° direction. There, the experimental and FE strains do not overlap as they did in Figure 32, but the difference between the experimental strains and those predicted by FE decreases from 41.9 $\mu\epsilon$ to 34.3 $\mu\epsilon$ when using the strains at the 0.6 mm deep hole as a reference.

The choice of reference depth has been shown to have a large influence on the processed results. The extent of that difference is visually quantified on Figure 34. The procedure used to find the experimental strains on Figure 33 was used to reprocess the previously obtained data to find what the experimental strains would have been had hole depths 0.3 mm to 0.7 mm, excluding 0.4 mm, been used as references. The experimental strains for each reference hole case were then added to the predicted FE strains with the 0.2 mm deep hole defined as the reference. This allows the strains processed of all different reference hole depths to be expressed on the same set of axes and compared. These reprocessed strains were superimposed onto the strains found for a reference hole depth of 0.2 mm as semi-transparent points on Figure 34.

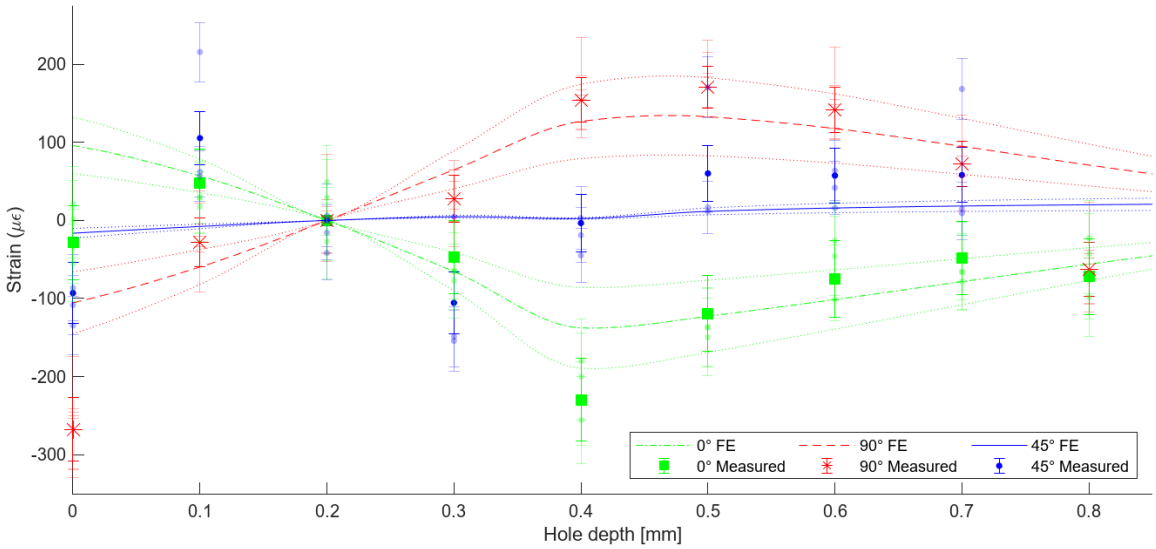

Figure 34: $[0_2/90_2]_s$ - Effect of reference hole choice in measured strain, $\Delta T = 100°C$

Figure 34 shows a large spread in uncertainty at each hole depth depending on which hole is used as a reference depth. The majority of the experimentally measured strains fall within the FE uncertainty bounds, but the degree of overlap varies depending on the reference used. The experimental uncertainty spread shown in Figure 34 suggests a larger overall uncertainty when taking into account the successive use of each valid hole as a reference. In general, these larger experimental uncertainties exhibit a larger overlap with the uncertainties in FE, however they still do not overlap at the undrilled rosette.

Although the trends observed in the experimental and FE strains are similar, they do not agree as well as expected. The drilled holes differ, even if slightly, from those modelled in FE in hole diameter and also contain an offset. An example of this is the hole drilled to a depth of 0.4 mm, a photomicrograph of which is shown in Figure 35. The hole was drilled closer to the 0° strain gauge grid. The strains in Figure 32 show a discrepancy at the 0.4 mm deep hole in the 0° direction. The closer a hole is to the strain gauge grid, the larger the measured strains. So long as the hole is still round, and the hole is drilled well, this discrepancy can be corrected as described in Section 5.4.1. This correction was applied to all holes.

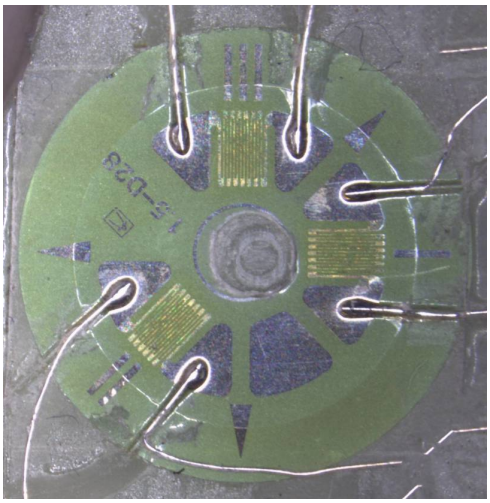

Figure 35: $[0_2/90_2]_s$ - 0.4 mm deep hole

The corrected experimental strains are shown in Figure 36. For ease of comparison, the strains not corrected for hole diameter and location are presented again in Figure 36a and the corrected strains are presented in Figure 36b.

The correction for diameter and hole location made little change to most of the experimentally measured strains, indicating that discrepancies present are not due to these factors. An exception to this is the strain measured in the 0° direction at the 0.4 mm deep hole. The experimental strain for this case improved from $-229.5\ \mu\epsilon$ to $-190.0\ \mu\epsilon$, bringing it closer to the FE predicted strain of $-137.5\ \mu\epsilon$. Although this result is not perfect, it does indicate that the effect of hole location was problematic in the strain initially measured.

Another experimentally obtained surface strain that deviates substantially from that predicted by FE is the strain in the 0° direction at a hole depth of 0.8 mm. Before correcting for diameter hole location, the experimentally measured strain for this point was $-62.6\ \mu\epsilon$ while FE predicted a surface strain of $69.9\ \mu\epsilon$. The corrections applied in Figure 36b did improve the experimental strain to $-42.0\ \mu\epsilon$, but this is still substantially lower than that predicted by FE.

The geometry of the 0.8 mm hole was considered as a possible reason for the disagreement between the experimental strains and the FE predictions. Upon inspection of the 0.8 mm deep hole (microphotograph shown in Figure 37a), it was found that the hole is misshaped, and the diameter thereof is difficult to accurately measure. The image of the hole was traced in Autodesk Inventor Professional, and the geometry exported to MSC Patran where it was used to model the drilled hole as it is. The odd shape of the hole complicated the meshing process. Instead of the typically preferred isomesh, a paver mesh was used for the area inside and just outside the hole in a circular transitional region before an isomesh was applied to the rest of the outer model. A full model was necessary because of the lack of symmetry. An image of the final mesh is shown in Figure 37b.

Keeping the FE data for all other drilled holes constant, the newly obtained FE data for the

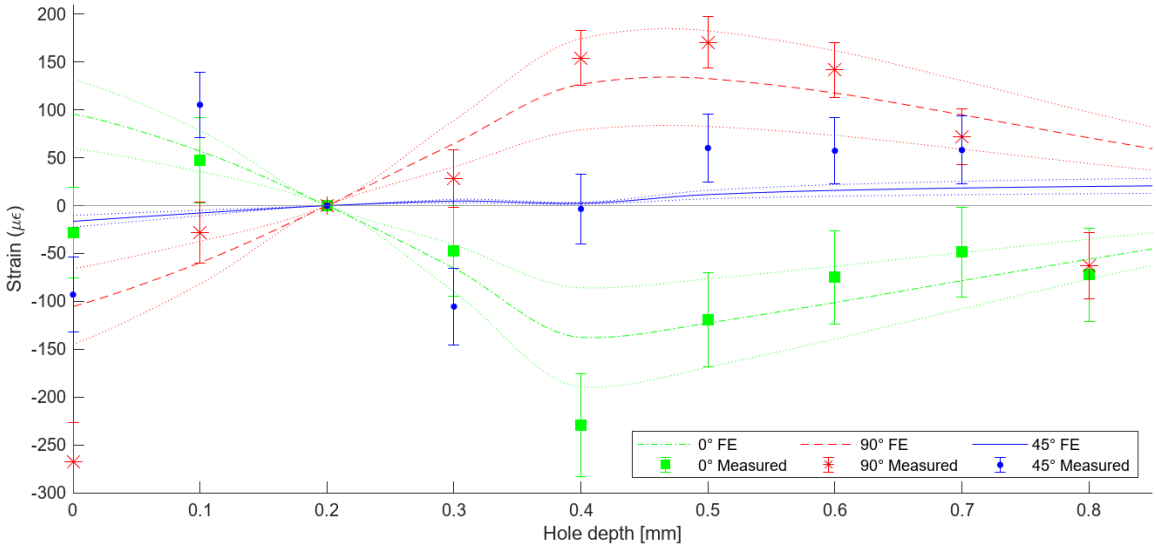

(a) Before strain correction

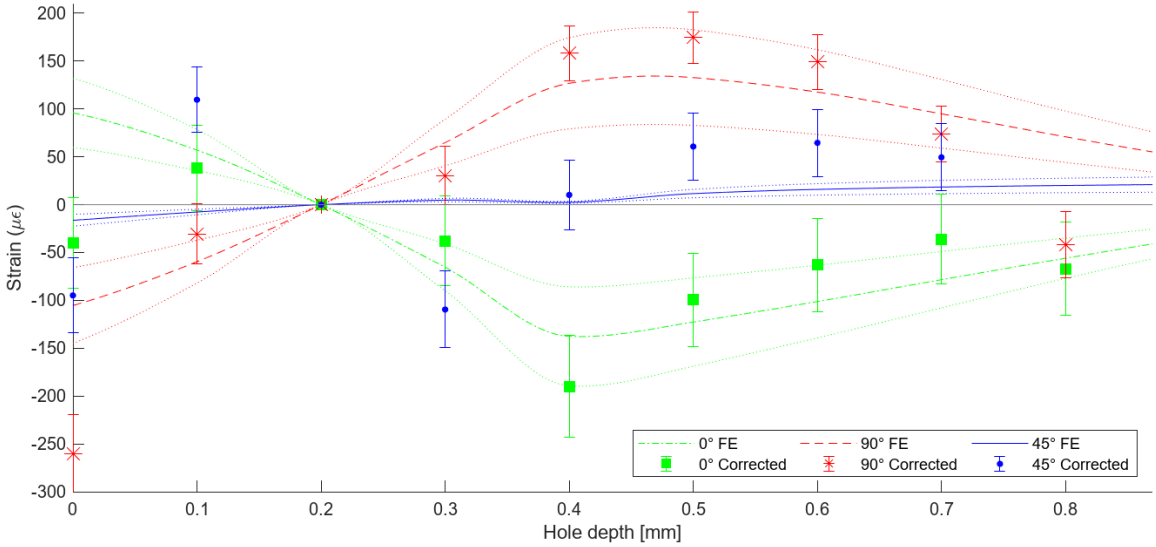

(b) After strain correction

Figure 36: $[0_2/90_2]_s$ - Comparison between strains before and after correction for hole location and diameter, $\Delta T = 100°C$

0.8 mm deep hole was plotted and compared to the uncorrected measured strains. The resulting data are plotted in Figure 38.

Using the improved FE model, the surface strains predicted by FE in the 0° direction at the 0.8 mm deep hole reduce to 34.7 $\mu\epsilon$. The uncertainty bounds still do not overlap, but the difference between the lower bound of the strains predicted by FE and the upper bound of the experimentally measured strains reduce from 51.2 $\mu\epsilon$ to 15.7 $\mu\epsilon$. The remaining difference between the strains predicted by FE and those obtained by experimentation may be due to the uncertainty in the hole shape. In Figure 37a, the perimeter of the hole is unclear, making the tracing thereof difficult to perform accurately. Furthermore, the photomicrograph of the specimen is only able to describe the surface of the hole. The shape at the bottom of the hole cannot be seen using this method, therefore it is not possible to accurately model. Additionally,

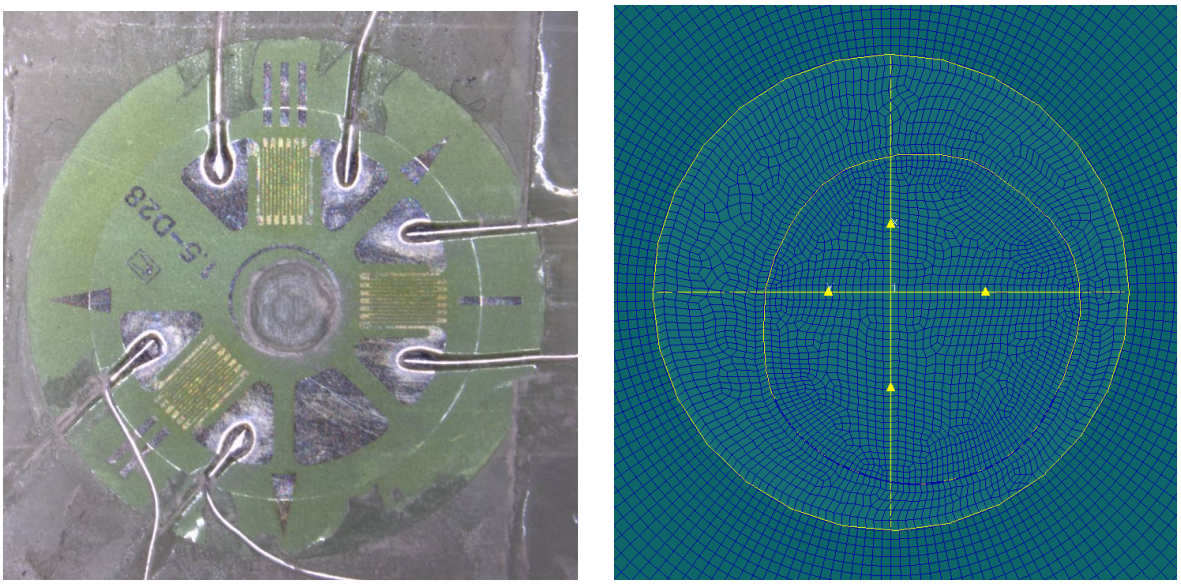

(a) Photomicrograph of Rosette (b) FE mesh

Figure 37: 0.8mm deep irregular hole drilled on $[0_2/90_2]_s$ specimen

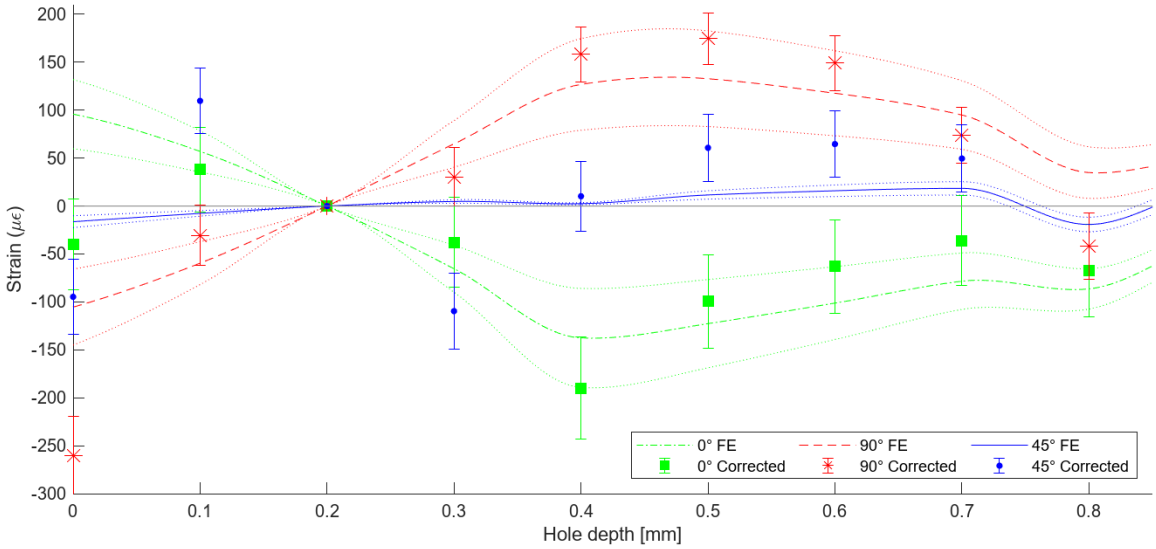

Figure 38: $[0_2/90_2]_s$ - Correction of 0.8 mm deep hole using more representative FE modelling, $\Delta T = 100°C$

the depth of the hole is close to the limit of sensitivity given the diameter of the hole. This may increase the measured surface strain uncertainty in this region. A positive point to be taken from the results obtained from the FE model that more correctly represents the physically drilled hole is the trend in the correct direction. The updated results shift downwards, which concur with the physically measured results.

6.2 $[0/90/+45/\text{-}45]_s$ Laminate

The $[0_2/90_2]_s$ laminate looked at thus far does not exhibit a large strain response in the 45° direction. The measured data seems to be scattered and less reliable than that in the 0° and 90° directions. To verify if the correlation between FE and measured physical strains exists, a laminate configuration that includes 45° plies was necessary. For the laminate to be balanced, a -45° ply was required for every +45° ply. A $[0/90/+45/\text{-}45]_s$ GFRP laminate was chosen to verify the behaviour of the strains in the 45° direction. A similar process to that followed for the $[0_2/90_2]_s$ specimen was adhered to. A preliminary hole was drilled to determine the offset between the microscope cross-hairs and the centre of the drilled hole so that the holes were more accurately drilled.

6.2.1 Experimental Results

The $[0/90/+45/\text{-}45]_s$ laminate made use of four strain gauge rosettes, three of which were drilled. Only three rosettes were used as the aim of testing this laminate was to verify the results of the $[0_2/90_2]_s$ laminate and the effect of 45° plies. The laminate underwent a cooling process, inducing a change in temperature of -98.93°C. The strains measured during testing were recorded and referenced to the undrilled rosette. The raw strains referenced to the undrilled rosette are shown in Figure 39. As with the $[0_2/90_2]_s$ laminate, the uncertainties are composed of the measurement noise and the strain gauge uncertainties.

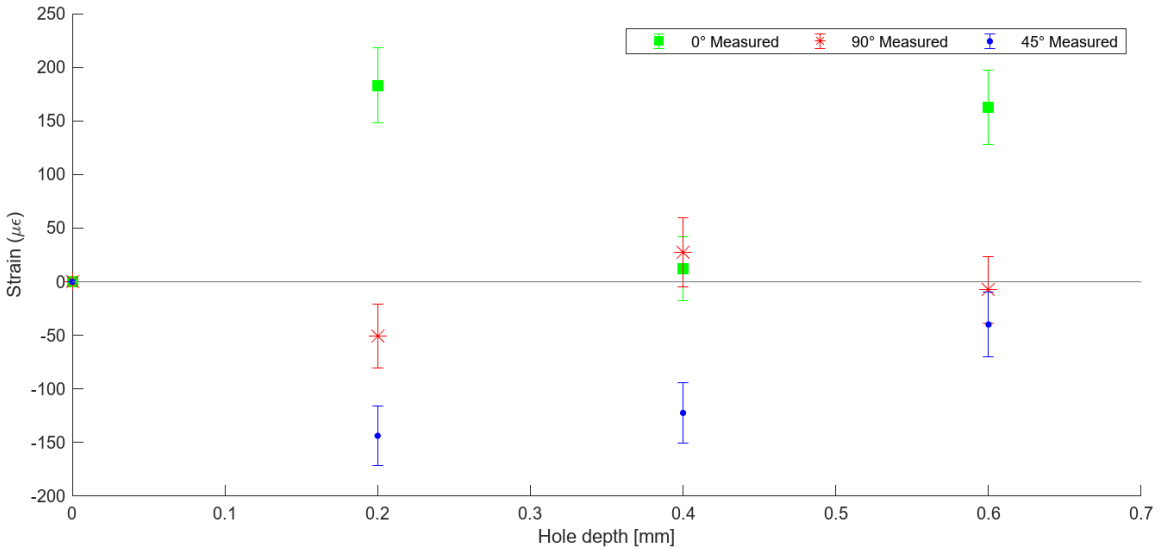

Figure 39: $[0/90/+45/\text{-}45]_s$ - Strains measured at holes of differing depths with respect to the undrilled rosette, ΔT = -98.93°C

Since there are so few holes only coarse trends can be observed. The strains in the 0° direction have two turning points: at depths of 0.2 mm and 0.4 mm. The same is seen in the 90° direction. This trend is similar to that seen in the $[0_2/90_2]_s$ laminate, where there are distinct changes in gradient as the hole depth goes from one laminate layer to another. The strains in the 45°

direction seem to decrease from a depth of 0.0 mm to a turning point at 0.2 mm with the strains steadily increasing thereafter until 0.6 mm.

Without looking at the FE results, it is unclear whether the strains measured at the undrilled strain gauge rosette are erroneous or not as with the $[0_2/90_2]_s$ laminate. As each strain direction only has four datapoints, an error in the reference rosette may make the strains difficult to interpret.

6.2.2 FE Results

As for the $[0_2/90_2]_s$ laminate, the FE prediction for the strains in the 0°, 45° and 90° directions for the $[0/90/+45/\text{-}45]_s$ laminate were found using models representing 2.0 mm diameter holes of different depths. A temperature change of 100°C was applied to the models. 100°C was chosen as it allows for easy scaling of the strains. The resulting strains are shown in Figure 40 with the undrilled state as the reference. The uncertainty bands were found by Monte Carlo trials as explained in Section 5.4.2 and are denoted in broken lines to two standard deviations to include 95% of the possible variation.

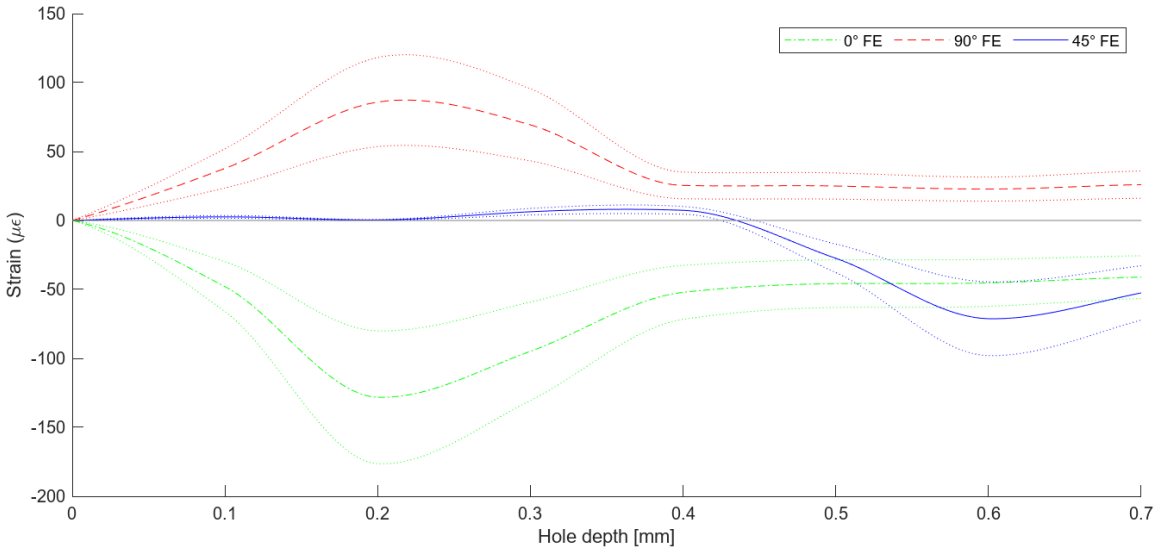

Figure 40: $[0/90/+45/\text{-}45]_s$ - FE model with undrilled state as the reference datum, $\Delta T = 100°C$

As with the $[0_2/90_2]_s$ laminate, the surface strains in the 0° directions follow a mirrored trend to the surface strains measured in the 90° direction. The strains in both the 0° and 90° directions start at zero and reach their absolute maxima of -128.2 $\mu\epsilon$ and 86.2 $\mu\epsilon$ respectively at a hole depth of 0.2 mm. This corresponds to the interface between the plies in the 0° and the 90° directions. The strains then reach another turning point at a depth of 0.4 mm, the interface between the plies in the 90° and 45° directions. From this point on, the strains in the 0° and 90° direction remain relatively constant regardless of an increase in hole depth.

The strains in the 45° directions vary more in the $[0/90/+45/\text{-}45]_s$ laminate than in the $[0_2/90_2]_s$ laminate. They increase very gradually to a value of 7.2 $\mu\epsilon$ at a hole depth of 0.4 mm whereafter

the gradient changes sharply, decreasing to a value of local minimum of $-71.2\ \mu\epsilon$ at a hole depth of 0.6 mm. The presence of plies in the 45° direction causes a large strain response once that lamina is drilled into.

As with the $[0_2/90_2]_s$ laminate, the absolute uncertainties related to the FE predictions are largest when the predicted strain is furthest away from 0 $\mu\epsilon$.

The strains predicted by FE offer some insight on how the measured strains should behave. Superimposing the FE strains on the experimentally measured strains allows for an easier comparison thereof.

6.2.3 Combination of Experimental and FE Strains

The experimental and FE predicted surface strains for the $[0/90/+45/\text{-}45]_s$ laminate are shown on Figure 41. All strains on this figure are referenced to the undrilled rosette and are for a temperature change of 100°C.

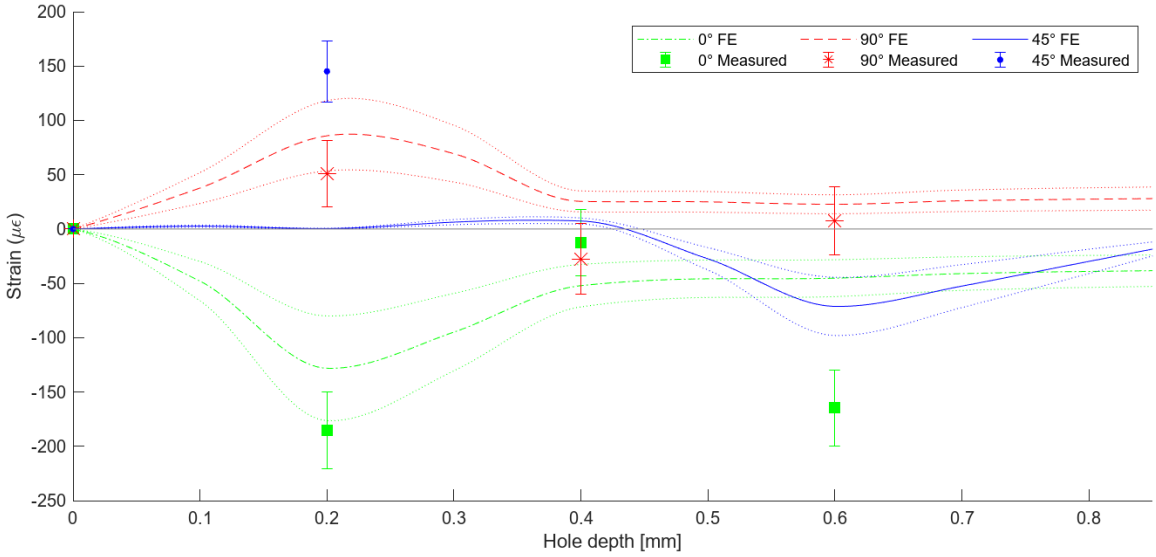

Figure 41: $[0_2/90_2]_s$ - FE and measured strains referenced to the undrilled rosette, $\Delta T = 100°C$

Setting the undrilled hole as a reference yields better results in the $[0/90/+45/\text{-}45]_s$ laminate than when the same is done on the $[0_2/90_2]_s$ laminate. The strains measured in the 0° direction only have one result, that measured for the 0.6 mm deep hole, where there is no overlap of uncertainties. Although the uncertainties of the surface strains measured for holes of depth 0.2 mm and 0.3 mm overlap with those of FE, their measured values do not. The strains are therefore acceptable, but not ideal.

A similar result is observed in the 90° direction. In this case, the uncertainties for the surface strains measured at hole depths of 0.2 mm and 0.6 mm overlap with those obtained by FE, but the strains do not fall within the FE uncertainty bounds. The uncertainties of the strain measured at the 0.4 mm deep hole does not overlap at all with those obtained by FE, but the

difference between the lower FE uncertainty bound and the upper measured strain uncertainty is 20.5 $\mu\epsilon$. Although the strains measured in the 90° direction are not ideal, they are acceptable and agree with FE better than the strains in the 0° direction. Additionally, all the measured strains in the 90° direction are constantly less than those predicted by FE by an amount of 42.9 ± 10.1 $\mu\epsilon$.

None of the surface strains in the 45° direction fall within the uncertainty bounds of the strains predicted by FE. The uncertainties of the experimental strains are also far off from the FE uncertainty bounds and at no point do these uncertainties overlap, however, the experimental strains are consistently all offset above those of FE by 128.2 ± 16.7 $\mu\epsilon$. This suggests that the experimental surface strains follow the same trend as the predicted strains, but that some factor such as erroneous measurements from the undrilled rosette may be causing a y-shift in the experimental strains. This is the same effect present in the $[0_2/90_2]_s$ laminate.

The trends seen in the strains measured in the 90° and 45° directions, along with the consistent difference observed between the experimental and FE results for each case suggest that the surface strains at the undrilled rosette are erroneous, albeit to a lesser extent than the undrilled rosette on the $[0_2/90_2]_s$ laminate. To investigate the possibility of erroneous strain measurements from the reference rosette, the reference surface strains were set to those measured at the surface of the 0.2 mm deep hole. The resulting strains are shown in Figure 42. The strains shown are corrected for hole diameter and offset.

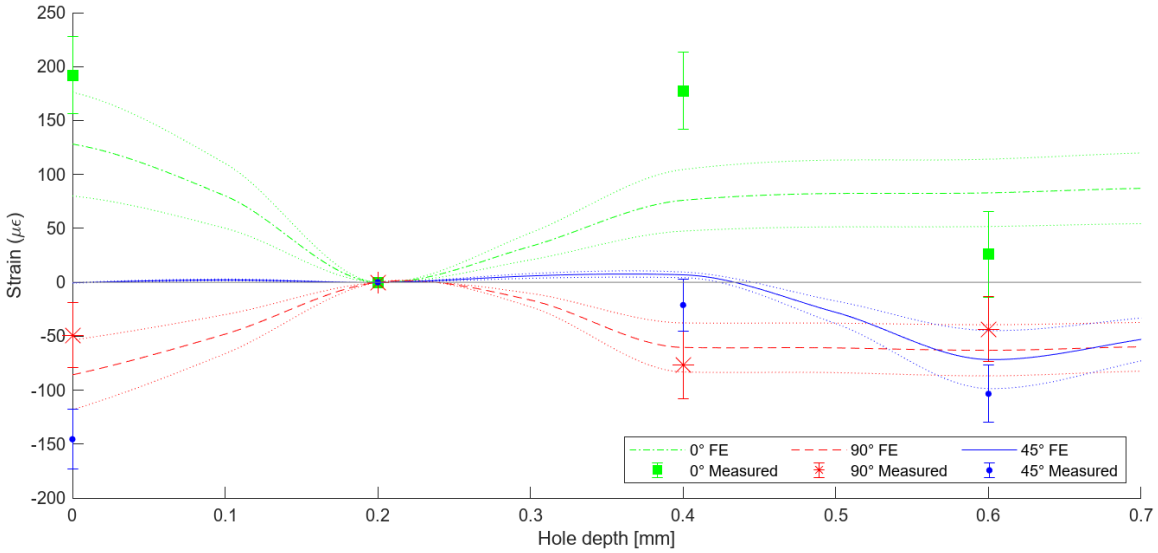

Figure 42: $[0_2/90_2]_s$ - FE and measured strains referenced to the 0.2 mm deep hole, ΔT = 100°C

The change in reference rosette improves the agreement between the experimentally measured strains and those predicted by FE. This is particularly true for the strains measured in the 90° and 45° directions. In the 90° direction, all the measured strains fall within the FE uncertainty bounds, and the strains predicted by FE fall within the experimentally measured strain uncertainty.

Although this is not true for the measured strains in the 45° direction, the experimental strain

uncertainties overlap with the FE uncertainty bounds for the 0.6 mm deep hole. At the 0.4 mm deep hole, the FE and experimental uncertainties do not overlap, but the difference between the upper experimental uncertainty and the lower bound of the FE uncertainty is only 1.7 $\mu\epsilon$. The strains measured in the 45° direction at the undrilled rosette differs from the predicted strains by 145.1 $\mu\epsilon$. The high level of agreement observed for the surface strains measured in the 45° direction at the 0.4 mm and 0.6 mm deep holes indicates that the strain measured at the undrilled rosette in the 45° direction may be inaccurate.

The uncertainties in the experimental surface strains measured in the 0° direction overlap with the FE uncertainty bounds at the undrilled location and a hole depth of 0.6 mm. The overlap in uncertainties indicates a fair level of agreement for these data points, even if the experimental surface strains do not fall within the FE uncertainty bounds. The surface strain uncertainties measured at the 0.4 mm deep hole in the 0° direction do not overlap at all with the FE uncertainty bounds. The lower experimental strain uncertainty differs from the upper bound of the FE uncertainty by 32.2 $\mu\epsilon$. An image of the strain gauge rosette stuck at the 0.4 mm deep hole is shown in Figure 43. No visual damage to the strain gauge rosette, eccentricity, or evidence of failed adhesion can be seen.

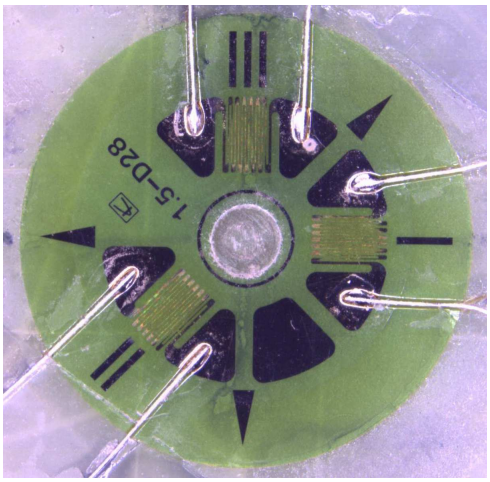

Figure 43: $[0/90/+45/\text{-}45]_s$ specimen - Strain gauge at 0.4mm deep hole

Since the uncertainties in material properties, measurement noise, strain gauge output, and drilled hole diameter and eccentricity have been taken into account, the discrepancy in the measured strain must either be due to another factor or the uncertainties have been underestimated.

Considering the results obtained for both tested laminates, the measured surface strains due to uniform thermal loading largely agree with those predicted by FE. Many of the measured strains do not align exactly with the FE prediction, but the overlapping uncertainties indicate that these differences are largely due to the possible variances in material properties and the uncertainties related to the instrumentation. It was also found that the reference hole selection affects the spread in uncertainties of all measured strains and the y shift of the entire strain distribution, at times causing the measured strains to be within the FE uncertainty bounds if one reference rosette is used, but not if another is used. Although the use of the surface strains

at an undrilled location is highly preferred, care must be taken in the selection of a different reference rosette should the undrilled rosette provide erroneous data. Some of the measured strains, such as those in the 90° direction at a depth of 0.8 mm on the $[0_2/90_2]_s$ laminate, did not agree with those predicted by FE at all. Further modelling shows that hole shape irregularity, along with the hole depth being at the limit of sensitivity, introduces uncertainties that are not being accounted for in the uncertainty analysis employed. Taking into account the uncertainties from known and uncertain sources, there is an acceptable level of agreement between measured strains and those predicted by FE. FE accurately models the surface strains observed in thermally tested laminates, and therefore the zeroth-order calibration coefficients of the power series expansion can be found by applying a known thermal load to a predrilled GFRP laminate.

7 Conclusions

A thermal load large enough to obtain a measurable strain response was successfully applied to the test laminates by placing them in a DCCTE preheated to 70°C which was subsequently cooled to approximately -25°C by the introduction of dry ice. It was observed that, when taking the appropriate uncertainties into account, the surface strains obtained by FE in the 0°, 90° and 45° directions largely concur with those measured in both trend and magnitude for the laminates tested.

While most measured results concur with those obtained by FE, anomalies in the overall trend are still present. These are most evident in the erroneous strains found at the undrilled rosettes. Using any alternative reference depth better aligns the measured strains with those obtained by FE. The uncertainties in the measured strains depend on the uncertainties in the reference rosette. The consequent uncertainties in the experimental strains found by successively using all holes as references increase the measurement uncertainty and hence, a larger overlap between the experimental strains and those found by FE is observed. When corrections were implemented to take into account the actual hole diameter and the offsets at which the holes were drilled, the agreement between the measured strains and those obtained from FE further improved. This is evident in the $[0_2/90_2]_s$ laminate at the hole drilled to a depth of 0.4 mm, where the experimental strain in the 0° direction improved from $-229.5\ \mu\epsilon$ to $-190.0\ \mu\epsilon$, closer aligning to the $-137.5\ \mu\epsilon$ predicted by FE . The observed beneficial effect of these corrections reinforce the finding that the surface strains present in a laminate due to a change in temperature largely concur with those obtained by FE.

Even though corrections for the actual hole diameter and offsets are implemented, additional outliers are still present. Diameter and offset corrections are challenging to apply to holes that do not have well-defined outlines or are irregularly shaped. Remodelling the holes while considering hole irregularity further improves the agreement between the measured results and FE. This improvement is seen in the $[0_2/90_2]_s$ laminate at the hole drilled to a depth of 0.8 mm, where the difference between the lower uncertainty bound for strains predicted by FE and the upper uncertainty in experimental strains in the 90° direction reduced from 51.2 $\mu\epsilon$ to 15.7 $\mu\epsilon$. This reinforces the conclusion that, so long as the holes drilled into the laminate closely resemble those modelled in FE, the strains measured on the laminate largely concur with those found by FE. Three large outliers are still present, two of which are on the $[0_2/90_2]_s$ laminate in the 45° direction at depths of 0.1 mm and 0.3 mm and one on the $[0/90/+45/\text{-}45]_s$ laminate in the 0° direction at a depth of 0.4 mm. The reason these readings do not align is currently unknown.

In spite of the few outliers that still remain in the corrected experimental strains, the level of agreement between the corrected experimental strains and the strains obtained by FE suggests that FE predicts, within the uncertainties associated with this work, the strains measured at holes of different depths in the presence of a thermal load. The zeroth-order calibration coeffi-

cients calculated for use in the series expansion method, and which are analogous to the surface strains, align with physical measurements, justifying their use.

8 Recommendations for future work

The following recommendations are for future work relating to the topics discussed in this dissertation:

- Repeat this investigation with high resistance IHD strain gauge rosettes. Although unavailable at the time of testing, the use of high resistance strain gauges would allow higher voltages to be used without locally increasing the laminate temperature. This would increase the resolution of the measured strains and decrease the measurement uncertainty.
- Assess the compatibility of measured and FE predicted strains for non-linear temperature distributions. This could be done by placing foil temperature sensors on each side of a laminate and placing the undrilled side on a surface of known temperature. The transient temperature distributions could be determined, thereby obtaining calibration coefficients for second and higher order temperature distributions. This would further validate the use of eigenstrain-inducing temperatures in the series expansion method to measure more diverse residual stress profiles.
- Develop a DCCTE that is able to actively cool the test environment and minimise humidity. An actively cooled environment would minimise some of the temperature oscillations that can occur by passive cooling.

References

[1] D. Rajak et al. “Fiber-Reinforced Polymer Composites: Manufacturing, Properties, and Applications”. In: *Polymers* 11.10 (2019), p. 1667. ISSN: 2073-4360. DOI: 10.3390/polym11101667.

[2] P. D. Mangalgiri. “Composite materials for aerospace applications”. In: *Bulletin of Materials Science* 22.3 (1999), pp. 657–664. ISSN: 0973-7669. DOI: 10.1007/bf02749982.

[3] C. Barile, C. Casavola and F. De Cillis. “Mechanical comparison of new composite materials for aerospace applications”. In: *Composites Part B: Engineering* 162 (2019), pp. 122–128. ISSN: 1359-8368. DOI: 10.1016/j.compositesb.2018.10.101.

[4] G. S. Schajer, M. B. Prime and P. J. Withers. “Why Is It So Challenging to Measure Residual Stresses?” In: *Experimental Mechanics* 62.9 (2022), pp. 1521–1530. ISSN: 1741-2765. DOI: 10.1007/s11340-022-00879-x.

[5] T. Wu et al. “Measurement and Analysis of Residual Stresses and Warpage in Fiber Reinforced Plastic and Hybrid Components”. In: *Metals* 11.2 (2021), p. 335. ISSN: 2075-4701. DOI: 10.3390/met11020335.

[6] G. Albertini, E. Girardin and A. Manescu. “Residual Stress Analysis by Neutron and X-ray Diffraction”. In: *Innovative Technological Materials: Structural Properties by Neutron Scattering, Synchrotron Radiation and Modeling*. Ed. by J. J. Skrzypek and F. Rustichelli. Berlin, Heidelberg: Springer Berlin Heidelberg, 2010, pp. 79–121. ISBN: 978-3-642-12059-6. DOI: 10.1007/978-3-642-12059-6_4.

[7] A. Birnbaum, S. Vikelic and Y. Lawrence Yao. “Advances in laser-induced plastic deformation processes”. In: *Advances in Laser Materials Processing*. Elsevier, 2010, pp. 535–572. ISBN: 9781845694746. DOI: 10.1533/9781845699819.6.535.

[8] N. Rossini et al. “Methods of measuring residual stresses in components”. In: *Materials & Design* 35 (2012), pp. 572–588. ISSN: 0261-3069. DOI: 10.1016/j.matdes.2011.08.022.

[9] S. White and H. Hahn. “Cure Cycle Optimization for the Reduction of Processing-Induced Residual Stresses in Composite Materials”. In: *Journal of Composite Materials* 27.14 (1993), pp. 1352–1378. ISSN: 1530-793X. DOI: 10.1177/002199839302701402.

[10] B. Cullity. *Elements of X-ray Diffraction*. Addison-Wesley metallurgy series. Addison-Wesley Publishing Company, 1956. ISBN: 9780201012309.

[11] P. Withers and H. Bhadeshia. “Residual stress. Part 1 – Measurement techniques”. In: *Materials Science and Technology* 17.4 (2001), pp. 355–365. ISSN: 1743-2847. DOI: 10.1179/026708301101509980.

[12] G. S. Schajer and M. B. Prime. “Use of Inverse Solutions for Residual Stress Measurements”. In: *Journal of Engineering Materials and Technology* 128.3 (2006), pp. 375–382. ISSN: 1528-8889. DOI: 10.1115/1.2204952.

[13] R. G. Treuting and W. T. Read. “A Mechanical Determination of Biaxial Residual Stress in Sheet Materials”. In: *Journal of Applied Physics* 22.2 (1951), pp. 130–134. ISSN: 1089-7550. DOI: 10.1063/1.1699913.

[14] G. Sachs and G. Espey. “The Measurement of Residual Stresses in Metals”. In: *Iron Age* 148.12 (1941), pp. 63–71.

[15] M. B. Prime. “Residual Stress Measurement by Successive Extension of a Slot: The Crack Compliance Method”. In: *Applied Mechanics Reviews* 52.2 (1999), pp. 75–96. ISSN: 2379-0407. DOI: 10.1115/1.3098926.

[16] M. B. Prime. “The Contour Method: Simple 2-D Mapping of Residual Stresses”. In: *Recent Advances in Solids and Structures*. IMECE2000. American Society of Mechanical Engineers, 2000, pp. 121–127. DOI: 10.1115/imece2000-1262.

[17] *ASTM E837-20. Standard Test Method for Determining Residual Stresses by the Hole-Drilling StrainGage Method*. ASTM International. 2021.

[18] R. H. Leggatt et al. “Development and experimental validation of the deep hole method for residual stress measurement”. In: *Journal of Strain Analysis* 31.3 (1996), pp. 177–186.

[19] K. P. Milbradt. “Ring-method determination of residual stresses”. In: *Proceedings of the Society for Experimental Stress Analysis (SESA)* 9.1 (1951), pp. 63–74.

[20] G. S. Schajer. “Application of Finite Element Calculations to Residual Stress Measurements”. In: *Journal of Engineering Materials and Technology* 103.2 (1981), pp. 157–163. ISSN: 1528-8889. DOI: 10.1115/1.3224988.

[21] R. Kelsey. “Measuring non-uniform residual stresses by the hole drilling method”. In: *Proceedings Society for Experimental Stress Analysis* 14 (1956), pp. 181–194.

[22] M. Negaresh, H. Nazockdast and A. A. Katbab. “The impact of various curing methods on the curing process of polymer-fiber composites analyzed using analytical approach”. In: *Results in Engineering* 23 (2024), p. 102861. ISSN: 2590-1230. DOI: 10.1016/j.rineng.2024.102861.

[23] C. Guan, L. Zhan and S. Yao. “Finite Element Simulation and Experimental Research on Uniformity Regulation of Microwave Heating of Composite Materials”. In: *Polymers* 14.17 (2022), p. 3484. ISSN: 2073-4360. DOI: 10.3390/polym14173484.

[24] J. P. Nobre et al. “Stress Evaluation Through the Layers of a Fibre-Metal Hybrid Composite by IHD: An Experimental Study”. In: *Experimental Mechanics* 64.4 (2024), pp. 487–500. ISSN: 1741-2765. DOI: 10.1007/s11340-024-01047-z.

[25] T. C. Smit and R. G. Reid. “Residual Stress Measurement in Composite Laminates Using Incremental Hole-Drilling with Power Series”. In: *Experimental Mechanics* 58.8 (2018), pp. 1221–1235. ISSN: 1741-2765. DOI: 10.1007/s11340-018-0403-6.

[26] T. Bergs et al. “Experimental Investigation concerning the Influence of Electrochemical Machining on Process Chain induced Residual Stress States”. In: *Procedia CIRP* 95 (2020), pp. 726–730. ISSN: 2212-8271. DOI: 10.1016/j.procir.2020.01.170.

[27] V. Savaria, F. Bridier and P. Bocher. “Computational quantification and correction of the errors induced by layer removal for subsurface residual stress measurements”. In: *International Journal of Mechanical Sciences* 64.1 (2012), pp. 184–195. ISSN: 0020-7403. DOI: 10.1016/j.ijmecsci.2012.07.003.

[28] D. Haeffner, J. Almer and U. Lienert. “The use of high energy X-rays from the Advanced Photon Source to study stresses in materials”. In: *Materials Science and Engineering: A* 399.1–2 (2005), pp. 120–127. ISSN: 0921-5093. DOI: 10.1016/j.msea.2005.02.023.

[29] B. Saini and R. Kaur. “X-ray diffraction”. In: *Handbook of Modern Coating Technologies*. Elsevier, 2021, pp. 85–141. ISBN: 9780444632395. DOI: 10.1016/b978-0-444-63239-5.00003-2.

[30] G. S. Schajer. “Advances in Hole-Drilling Residual Stress Measurements”. In: *Experimental Mechanics* 50.2 (2009), pp. 159–168. ISSN: 1741-2765. DOI: 10.1007/s11340-009-9228-7.

[31] G. Schajer. “Residual Stresses: Measurement by Destructive Testing”. In: *Encyclopedia of Materials: Science and Technology*. Elsevier, 2001, pp. 8152–8158. ISBN: 9780080431529. DOI: 10.1016/b0-08-043152-6/01462-5.

[32] G. S. Schajer. “Relaxation Methods for Measuring Residual Stresses: Techniques and Opportunities”. In: *Experimental Mechanics* 50.8 (2010), pp. 1117–1127. ISSN: 1741-2765. DOI: 10.1007/s11340-010-9386-7.

[33] U. M. Abdulkhadar et al. “An Assessment on Residual Stress Measurement in FRP Composites Using Relaxation Techniques”. In: *Iranian Journal of Materials Science & Engineering* 18.3 (2021). DOI: 10.22068/ijmse.2075.

[34] J. Mathar. “Determination of Initial Stresses by Measuring the Deformations Around Drilled Holes”. In: *Journal of Fluids Engineering* 56.3 (1934), pp. 249–254. ISSN: 0097-6822. DOI: 10.1115/1.4019712.

[35] H. W. Carpenter, R. G. Reid and R. Paskaramoorthy. “Sensitivity Analysis of the Crack Compliance and Layer Removal Methods for Residual Stress Measurement in GFRP Pipes”. In: *Journal of Engineering Materials and Technology* 138.3 (2016). ISSN: 1528-8889. DOI: 10.1115/1.4032559.

[36] X. Li et al. “Research progress of residual stress measurement methods”. In: *Heliyon* 10.7 (2024), e28348. ISSN: 2405-8440. DOI: 10.1016/j.heliyon.2024.e28348.

[37] B. P. S. and K. S. K. Karuppasamy. “Introduction and Application of Strain Gauges”. In: *Applications and Techniques for Experimental Stress Analysis*. IGI Global, 2020, pp. 57–77. DOI: 10.4018/978-1-7998-1690-4.ch004.

[38] W. Soete and R. Vancrombrugge. “An industrial method for the determination of residual stresses”. In: *Proceedings Society for Experimental Stress Analysis* 8.1 (1950), pp. 17–28.

[39] N. J. Rendler and I. Vigness. “Hole-drilling strain-gage method of measuring residual stresses: Authors indicate that this method permits the magnitudes and principal directions of residual stresses at the hole location to be determined”. In: *Experimental Mechanics* 6.12 (1966), pp. 577–586. ISSN: 1741-2765. DOI: 10.1007/bf02326825.

[40] G. S. Schajer. “Universal Calibration Constants for Strain Gauge Hole-Drilling Residual Stress Measurements”. In: *Experimental Mechanics* 62.2 (2021), pp. 351–358. ISSN: 1741-2765. DOI: 10.1007/s11340-021-00771-0.

[41] J. Chen, Y. Peng and S. Zhao. “Comparison between grating rosette and strain gage rosette in hole-drilling combined systems”. In: *Optics and Lasers in Engineering* 47.9 (2009), pp. 935–940. ISSN: 0143-8166. DOI: 10.1016/j.optlaseng.2009.03.014.

[42] D. V. Nelson, A. Makino and T. Schmidt. “Residual Stress Determination Using Hole Drilling and 3D Image Correlation”. In: *Experimental Mechanics* 46.1 (2006), pp. 31–38. ISSN: 1741-2765. DOI: 10.1007/s11340-006-5859-0.

[43] G. S. Schajer. “Hole-Drilling Residual Stress Measurements at 75: Origins, Advances, Opportunities”. In: *Experimental Mechanics* 50.2 (2009), pp. 245–253. ISSN: 1741-2765. DOI: 10.1007/s11340-009-9285-y.

[44] T. Smit and R. Reid. “Use of Power Series Expansion for Residual Stress Determination by the Incremental Hole-Drilling Technique”. In: *Experimental Mechanics* 60.9 (2020), pp. 1301–1314. ISSN: 1741-2765. DOI: 10.1007/s11340-020-00642-0.

[45] A. Niku-Lari, J. Lu and J. F. Flavenot. “Measurement of residual-stress distribution by the incremental hole-drilling method”. In: *Experimental Mechanics* 25.2 (1985), pp. 175–185. ISSN: 1741-2765. DOI: 10.1007/bf02328809.

[46] M. T. Flaman and B. H. Manning. “Determination of residual-stress variation with depth by the hole-drilling method”. In: *Experimental Mechanics* 25.3 (1985), pp. 205–207. ISSN: 1741-2765. DOI: 10.1007/bf02325088.

[47] G. S. Schajer. “Measurement of Non-Uniform Residual Stresses Using the Hole-Drilling Method. Part I—Stress Calculation Procedures”. In: *Journal of Engineering Materials and Technology* 110.4 (1988), pp. 338–343. ISSN: 1528-8889. DOI: 10.1115/1.3226059.

[48] G. S. Schajer. “Measurement of Non-Uniform Residual Stresses Using the Hole-Drilling Method. Part II—Practical Application of the Integral Method”. In: *Journal of Engineering Materials and Technology* 110.4 (1988), pp. 344–349. ISSN: 1528-8889. DOI: 10.1115/1.3226060.

[49] J. Nobre et al. “Induced drilling strains in glass fibre reinforced epoxy composites”. In: *CIRP Annals* 62.1 (2013), pp. 87–90. ISSN: 0007-8506. DOI: 10.1016/j.cirp.2013.03.089.

[50] G. S. Schajer and L. Yang. “Residual-stress measurement in orthotropic materials using the hole-drilling method”. In: *Experimental Mechanics* 34.4 (1994), pp. 324–333. ISSN: 1741-2765. DOI: 10.1007/bf02325147.

[51] O. Sicot et al. “Determination of Residual Stress in Composite Laminates Using the Incremental Hole-drilling Method”. In: *Journal of Composite Materials* 37.9 (2003), pp. 831–844. ISSN: 1530-793X. DOI: 10.1177/0021998303031057.

[52] P. Pagliaro and B. Zuccarello. “Residual Stress Analysis of Orthotropic Materials by the Through-hole Drilling Method”. In: *Experimental Mechanics* 47.2 (2007), pp. 217–236. ISSN: 1741-2765. DOI: 10.1007/s11340-006-9019-3.

[53] M. Beghini, T. Grossi and C. Santus. "Validation of a strain gauge rosette setup on a cantilever specimen: Application to a calibration bench for residual stresses". In: *Materials Today: Proceedings* 93 (2023), pp. 719–724. ISSN: 2214-7853. DOI: 10.1016/j.matpr.2023.05.505. URL: http://dx.doi.org/10.1016/j.matpr.2023.05.505.

[54] J. Nadeau and M. Ferrari. "Effective thermal expansion of heterogeneous materials with application to low temperature environments". In: *Mechanics of Materials* 36.3 (2004), pp. 201–214. ISSN: 0167-6636. DOI: 10.1016/s0167-6636(03)00009-7.

[55] V. Luzin. "Use of the Eigenstrain Concept for Residual Stress Analysis". In: *Materials Science Forum* 768–769 (2013), pp. 193–200. ISSN: 1662-9752. DOI: 10.4028/www.scientific.net/msf.768-769.193.

[56] A. N. Tikhonov et al. *Numerical Methods for the Solution of Ill-Posed Problems*. Springer Netherlands, 1995. ISBN: 9789401584807. DOI: 10.1007/978-94-015-8480-7.

[57] *ASTM D3039/D3039M. Standard Test Method for Tensile Properties of Polymer Matrix Composite Materials*. ASTM International. 2014.

[58] *ASTM D3518/D3518M. Standard Test Method for In-Plane Shear Response of Polymer Matrix Composite Materials by Tensile Test of a 45° Laminate*. ASTM International. 2013.

[59] F. Lanza di Scalea. "Measurement of thermal expansion coefficients of composites using strain gages". In: *Experimental Mechanics* 38.4 (1998), pp. 233–241. ISSN: 1741-2765. DOI: 10.1007/bf02410384.

[60] ASM International. *ASM handbook vol. 2*. ASM Handbooks. ASM International, 1990.

[61] G. S. Schajer. "Use of displacement data to calculate strain gauge response in non-uniform strain fields". In: *Strain* 29.1 (1993), pp. 9–13. ISSN: 1475-1305. DOI: 10.1111/j.1475-1305.1993.tb00820.x.

[62] BIPM. "Guide to the expression of uncertainty in measurement. JCGM 100:2008". In: *Evaluation of measurement data* (2008). DOI: 10.59161/jcgm100-2008e.

[63] BIPM and IEC and IFCC and ILAC and IUPAC and IUPAP. "Evaluation of measurement data - Supplement 1 to the "Guide to the Expression of Uncertainty in Measurement"". In: *Propagation of distributions using a Monte Carlo method* (2008).

[64] S. Ratick and G. Schwarz. "Monte Carlo Simulation". In: *International Encyclopedia of Human Geography*. Elsevier, 2009, pp. 175–184. ISBN: 9780080449104. DOI: 10.1016/b978-008044910-4.00476-4.

[65] R. Schapery. "Thermal Expansion Coefficients of Composite Materials Based on Energy Principles". In: *Journal of Composite Materials* 2.3 (1968), pp. 380–404. ISSN: 1530-793X. DOI: 10.1177/002199836800200308.

[66] C. T. Herakovich. *Mechanics of fibrous composites*. en. Nashville, TN: John Wiley & Sons, 1997.